Topological Protection and Emission Control in a Waveguide Quantum Electrodynamical System

Ciarán McDonnell

A thesis presented for the degree of
Doctor of Philosophy

School of Physics and Astronomy
University of Nottingham
United Kingdom

March 2023

Abstract

In this thesis we explore methods for controlling and protecting quantum processes in a QED system. We begin with an explanation of how topology can arise in physics before deriving the quantum optical master equation of identical two-level atoms coupled to a one-dimensional nanofiber waveguide. We analyze the topological and dynamical properties of a system formed by placing the atoms in two chains, whose interactions with the guided modes of the nanofiber induce all-to-all excitation hopping. We find that, in the single excitation limit, the bulk topological properties of the Hamiltonian that describes the coherent dynamics of the system are identical to the ones of a one-dimensional Su-Schrieffer-Heeger (SSH) model. We confirm this in the short-range interacting limit by showing the bulk-boundary correspondence - the emergence of robust edge states in the topologically non-trivial phase of the model. Upon extending the range of interactions however, we find weakening of this bulk-boundary correspondence. This is illustrated by the variation of the localization length and mass gap of the edge states encountered as we vary the lattice constant and offset between the chains. Most interestingly, we analytically identify parameter regimes where edge states arise which are fully localized to the boundaries of the chain, independently of the system size. These edge states are shown to be not only robust against positional disorder of the atoms in the chain, but also subradiant, i.e., dynamically stable even in the presence of inevitable dissipation processes. Furthermore we show how the population of an edge excitation can be transported from one end of the chain to the other and how one can engineer different dynamical properties of the edge excitations, such as superradiant decay.

We next examine the guided emission properties of the atoms coupled to the nanofiber waveguide via weak laser-driving. We first investigate the effects of varying the spacing between atoms in the same and different chains and find that the fiber coupling efficiency, as well as the flux of the guided emission are maximised when neighbouring atoms are separated by a multiple of the wavelength of the light in the nanofiber, satisfying the modified Bragg condition. These two observables increase with the system size before saturating for large enough atom numbers. Moreover, we find that placing the two chains on opposite sides of the nanofiber allows us to enhance both the FCE and the guided photon flux even further. Moreover, these observables are optimized further by choosing an appropriate value of the detuning between the laser and atomic frequency. Next we study the correlation properties of the photon emission into the guided modes. For a system of two atoms driven by a resonant laser on the same side or opposite sides of the fiber, we find that by varying the distance between the atoms the same-time photon correlation functions can exhibit photon bunching or anti-bunching. Furthermore, the time-separated correlation functions of photons emitted by atoms above the nanofiber may exhibit persistent quantum beat behaviour for fixed atomic separation between the atoms. No such beats are found when the atoms are on opposite sides of the fiber. The overall size of the photon bunching and anti-bunching effects exhibited by same-time correlations are found to reduce with increased system size, suggesting that large system sizes may only exhibit coherent photon emission.

Acknowledgements

Firstly I would like to thank my supervisor Dr. Beatriz Olmos for her unending support and mentorship throughout this research and beyond. You have always encouraged me to get the most from my Ph.D. experience which has really helped me to grow in confidence and maturity. I admit I will miss the trips to Germany, but not so much the winter trips.

An immeasurable thank you to my family. To my parents, who have loved and supported me irrespective of my decisions in life. I cannot thank you enough for how you raised us and have thought me to see the joy and love in everything in life. To my siblings, I cannot thank you enough for always being there at important times in my life and pretending to know what it is I do in my Ph.D., it helps to keep me grounded. Finally to my wife Chloe. The best thing that happened to me during this journey was meeting you. Everything just seems that bit brighter and more meaningful thanks to you, even writing papers.

To my oldest friends, wherever you may be. Without you I would not have had the confidence to undertake this journey. You have pushed me to be better in all aspects of life, but never expected it from me. For that I am forever thankful. To my friends I have made along the way. I feel very privileged to have met you and have had you all play a part in this journey of mine. A special mention to the senior members of NUFC in my first year. You are one of the biggest reasons I settled here so quickly and a true inspiration for how any club should be run. YAMN.

To those that have come and gone in the CQNE group and beyond. Throughout my time here you have made this a fantastic place to work. Be it office chats or wine nights, you made the days and weeks easier and more enjoyable. I hope that everyone gets to work in an environment like the one you created here.

List of Publications

The research presented in this thesis covers, among other topics, the subjects of each of the following manuscripts.

Chapter 3:

Ciarán McDonnell and Beatriz Olmos. "Subradiant edge states in an atom chain with waveguide-mediated hopping." Quantum, 6:805, 9 2022.

Chapter 4:

Ciarán McDonnell and Beatriz Olmos. "Enhanced fiber coupling efficiency and photon correlation properties from a driven periodic emitter chain" (in preparation).

Contents

Chapter 1

Introduction

Quantum mechanical processes can be, almost by definition, difficult to control. Even when closed off from the outside world, the non-deterministic nature of quantum mechanics means that we cannot predict with certainty what the outcome of a process will be. What's more, once we open that system to the influence of its environment it is very difficult to retain the 'quantum nature' of these processes long enough to make practical use of them. Interactions with the surrounding environment can cause a quantum system to lose the *coherence* that made it a quantum system in the first place. This is known as *decoherence* [1]. Difficulties in controlling quantum processes and prolonging decoherence make it extremely challenging to design and construct quantum technologies on any sort of commercial scale. At the time of writing, IBM's quantum processor "Osprey" currently boasts the most qubits at 433 yet the processor must be kept at ultra-low temperatures and isolated from the outside environment, not something achievable in an everyday setting. The numerous fields that pose possible solutions or at least improvements to controlling quantum processes are sure to play a part in the advancements of quantum technologies. One such field is quantum electrodynamics.

1.1 Quantum Electrodynamics

The field of quantum electrodynamics (QED) has come a long way since Dirac explained how emission and absorption properties of a single atom interacting with an electromagnetic field may be solved with quantum mechanics [2]. With such fundamental processes explained, the building blocks were provided for close to a century of exploration into systems of ever-growing complexity within the QED field.

In the 1940s Purcell showed that the environment of a two-level emitter could significantly reduce the relaxation time of said two-level system [3]. This became the next major step in the complexity-building of QED systems. Now scientists knew that the introduction of different media (i.e. not just electromagnetic field in free space) could change the fundamental properties of, in this case, a two-level atom. This gave some degree of control over a quantum process and it inspired research into how other forms of media could alter atomic properties like dielectric surfaces, cylindrical nanofibers and nuclear-magnetic media [4–7].

In the 1950s Dicke showed that instead of introducing different media into

the environment of emitters, one could alter the emission properties collectively i.e. by introducing more emitters. It was shown that the radiation properties of molecules in a gas could be enhanced due to their collective interactions [8]. The 'strong' radiation of the gas due to coherence was coined *superradiance* and could not be explained simply by the sum of the individual emitter properties. Although only hinted at by Dicke, there also existed a prescription for collective suppression of emitter radiation now referred to as *subradiance*. Superradiance and subradiance add another degree of control to systems in QED which has been widely expanded on in the last half-century [9–13].

The separate research paths of single emitters with different media and collective emitters inevitably merged. A seminal example of this came in 2005 when Le Kien et al. investigated the coupling of two distant atoms via interactions mediated by a nanofiber waveguide [14]. This waveguide QED approach has resulted in new levels of control over quantum emitter processes from suppression and enhancement of emission of radiation into the waveguide [15–23] to the control of the directionality of the radiation emitted into the waveguide [23–29] and provide promise in the context of designing quantum networks and quantum gates [30–32]. Recently these waveguide QED systems have also been shown to exhibit correlated photon emission. Calculation of the second order coherence function has revealed the facilitation of photon bunching [33, 34] where the emission is expected in short pulses, photon anti-bunching [29, 35] where the emission is expected to be well separated in time, and the emergence of quantum beats [19, 36, 37] which causes the correlation functions to oscillate.

1.2 Topological Protection

In the early 1980's, unbeknownst to Tsui and Gossard [38], and Klitzing, Dorda and Pepper [39] they had just found the first experimental observation of topology in physics. The unmistakable quantised Hall conductance plateaus of the *integer quantum Hall effect* (IQHE), where the system exhibits an insulated bulk but allows for a charge current on the boundary, were first explained by Laughlin [40] and Thouless et al. [41]. The latter showed that the integer quantisation was an invariant, often called the *TKNN invariant*, which could not change unless the energy band gaps of the model close. It was not until the seminal work of Berry [42] that the true topological nature of the TKNN invariant was realised in that it is equivalent to the *geometric phase* of the system. Berry showed that if a state depends on some collection of parameters, and during adiabatic evolution of that state the parameters evolve and return to their original values (creating a closed loop in parameter space), that state may obtain a measurable phase which is quantised to an integer multiple of 2π. This integer was precisely that of the TKNN invariant. The geometry of the parameter space on which the closed loop formed dictated the existence of this phase. Thus it was shown that the intrinsic geometry of a system's parameter space can have observable physical effects on the system itself. As a result of the impact of Berry's research this geometric phase is often referred to as the *Berry phase* and it has been observed in a number of settings [43–45]. In a reversed situation, Kane and Mele predicted the existence of the *quantum spin Hall effect* (QSHE) [46], where the system exhibits an insulating bulk but allows for a spin current on the boundary, after adapting

work previously done by Haldane [47]. Bernevig and Hughes predicted this phenomenon independently [48] before it was later observed in HgTe quantum wells [49]. The calculation of the Berry phase (or equivalent topological invariants) became the tell-tale step in the search for non-trivial *topological states* of matter.

Topological phases of matter have been researched in a wide range of settings from cold atoms [50–52] and photonics [53–57] to resonators and quantum dots [58, 59], with experiments continuously finding and verifying the existence of these topological states [49, 60–63]. One of the main appealing features of these topological states is their robust nature. As Thouless et al. alluded to, these topological invariants which classify the topological state of matter cannot change unless the energy band gaps of the system close. This means that these gapped topological states have an inherent defence against local noise, perturbation and disorder which does not close the energy gap. Information encoded using these intrinsically robust states of matter would have a natural tolerance against environmental disorder and thus have been proposed for use in quantum computing and information processing [64–67].

Much of the topological matter has been classified by Schnyder and Ryu et al. into *topological insulators* and *topological superconductors* [68, 69]. Given a system's dimensionality and the presence or absence of certain symmetries, the possible topological invariants constituting topological phases of matter can be determined. Topological insulators are named for their insulating bulk properties and zero-energy conducting boundary modes often referred to as *edge states* [70–73]. The correspondence between the topological invariant of a system's insulating bulk and the existence of the zero-energy conducting edge states is known as the *bulk-boundary correspondence* [74, 75]. This classification of topological insulators and superconductors, referred to as the *tenfold way classification*, is limited to systems with interactions much shorter than the size of the system. Much work has been done on the theory of the effects that long-range[1] interactions have on the topological states of matter and the bulk-boundary correspondence which has included the emergence of *massive edge states* [76–84], however the topological nature of systems with interactions which do not decay with distance have not been studied either theoretically or experimentally.

One of the simplest examples of a topological insulator is that of the Su-Schrieffer-Heeger (SSH) model, originally used as a model for the transport properties in a polyacetylene chain [85]. The SSH model is a one-dimensional (1D) nearest-neighbour staggered-hopping model that we now know belongs to the BDI symmetry class of the tenfold way classification. 1D systems were thought not to exhibit non-trivial topology until 1989 when Zak showed how 1D solids may exhibit a non-zero (although now quantised to integer multiples of π) Berry phase [86]. Now the SSH model is a benchmark example for those both new and experienced in the field of topological insulators thanks to the zero-energy majorana edge states exhibited in the topological insulator phase [87, 88]. The SSH model has even been theoretically [89] and experimentally [90] realised using the emitter-waveguide QED systems described above and has even been researched in the context of formulating quantum gates [91].

The topological edge states of the SSH model have been observed in experi-

[1] 'Long-range' in the literature can range from next-nearest neighbour interactions in the context of hopping models, to almost all-to-all interacting systems.

ment only for very few systems [92, 93]. This is in part due to the difficulty of neglecting further than nearest-neighbour interactions in real physical systems. There have been a few research efforts to investigate the extension to long-range interactions in a toy SSH model approach [81, 82], but very few experimental efforts [90] or theoretical efforts which take experimental realisation into consideration [94]. Further efforts have focused on the addition of more sites to the typical two-site unit cell of the SSH model, but this does not explore the effects of long-range interactions [95, 96].

1.3 Thesis Structure

In this thesis we aim to further develop methods of controlling the processes occurring in waveguide quantum electrodynamical systems in two main ways; by investigating the topological properties of the system and by investigating the degree of control over photons emitted in the system via system engineering. In Chapter 2 we begin by detailing how topology is found in physics and how one can calculate the topological invariant of a system. Next we introduce the mathematical framework used to derive the quantum optical master equation in general, before showing further derivations specific to a system of atoms coupled to a cylindrical nanofiber waveguide. Lastly we detail some of the methods used in simulating the dynamics of such a system.

In Chapter 3 we show in detail how an atom-waveguide QED system can be used to simulate the one-dimensional SSH model with all-to-all interactions. We then detail the topological characteristics of this SSH model in the short-range interaction limit before extending to long-range interactions and investigating whether any of these characteristics are retained. Next we examine the dynamics of this long-range SSH model to see if our results persist in time or whether dissipative effects dominate the dynamics. We finish the chapter by giving our conclusion from the findings and discussing possible future research avenues from the chapter results.

In Chapter 4 we explore the emission properties of a similar atom-waveguide QED system via laser-driving. We specifically focus on how the spacing between atoms placed in two chains, as well as the offset between these chains affects the flux of photons emitted into the waveguide as well as the fraction of total emission which is into the waveguide. Different arrangements and sizes of the atomic chains are compared before the effects that an off-resonant laser has on these emission properties is examined. We then investigate the correlations of the emitted photons in a search for quantum signatures of light. We end this chapter with our conclusion from this research and a discussion on future research which could improve the results we have found.

We note that throughout this thesis we have set $\hbar = 1$.

Chapter 2

Theoretical Background

This chapter provides the mathematical framework used in this thesis for the analysis of the topological characteristics of matter and the collective emission of many-body QED systems.

Sec. 2.1 details how the topology of a system's phase space can have real implications on the physics we see in said systems. We derive in general the conditions necessary for these topological effects to be present and give an intuitive explanation as to how these effects arise, finding parallels with electromagnetism. We then explain how these topological characteristics, if any, can be classified via the symmetries that are present (or absent) in a system. We go on to explain the correspondence between this classification and the existence of topological boundary modes or edge states, known as the *bulk-boundary correspondence*. Finally we show the exact method we use to detect the topological characteristics in our research.

In Sec. 2.2 we outline the derivation of the Lindblad master equation considered throughout this thesis. We first derive the Redfield equation for a general quantum system before applying and justifying the approximations typically used in quantum optical systems. The derivation then becomes less general as we introduce the specifics of the QED system we are looking to research. We specify the structure of the atoms considered as well as deriving the structure of the different modes of the electromagnetic field specific to the system at hand. These specifications along with the usual approximations of quantum optical systems lead us to refine the Redfield equation into a master equation specific to our research which is in Lindblad form. We illustrate some examples of the collective nature of the emission from this many-body system in order to highlight the key properties we will search for later in the thesis.

In Sec. 2.3 we discuss the difficulties faced when trying to solve for the dynamics of a quantum system obeying the Lindblad master equation, either analytically or numerically. We detail the methods used to overcome these difficulties, allowing us to efficiently simulate the dynamics of the many-body QED system. Finally we briefly discuss the limitations of these methods.

2.1 Topology in Physics

In this section we present a detailed derivation of the geometric phase associated with non-trivial topological phases of matter. We give an intuition as to how

one can think about this geometric phase and explain the important details for the general classification of the topological nature of system Hamiltonians before introducing and explaining the winding number method for this classification that will be used in Chapter 3.

2.1.1 Time-dependent Hamiltonians and Adiabaticity

Here, we will combine analysis of instantaneous eigenstates of time-dependent Hamiltonians with the adiabatic theorem to show the emergence of the geometric phase also known as the Berry phase. Our starting point is a Hamiltonian $H(\boldsymbol{R})$ parameterised by any number of parameters $\boldsymbol{R} = \begin{pmatrix} R_1, & R_2, & \cdots, & R_N \end{pmatrix}$ which span an arbitrary vector space $\mathbb{R}^N$. This Hamiltonian satisfies the eigenvalue equation [97]

$$H(\boldsymbol{R}) \left|\psi_n(\boldsymbol{R})\right\rangle = E_n(\boldsymbol{R}) \left|\psi_n(\boldsymbol{R})\right\rangle \tag{2.1}$$

for any set of parameters $\boldsymbol{R}$. This equation must hold even if the parameters themselves depend on time $\boldsymbol{R} = \boldsymbol{R}(t) = \begin{pmatrix} R_1(t), & R_2(t), & \cdots, & R_N(t) \end{pmatrix}$ since any evolution of the parameters will remain in the parameter space. This leads to the instantaneous eigenvalue equation

$$H[\boldsymbol{R}(t)] \left|\psi_n[\boldsymbol{R}(t)]\right\rangle = E_n[\boldsymbol{R}(t)] \left|\psi_n[\boldsymbol{R}(t)]\right\rangle . \tag{2.2}$$

Here $\left|\psi_n[\boldsymbol{R}(t)]\right\rangle$ are the instantaneous eigenstates of $H[\boldsymbol{R}(t)]$ with eigenvalues $E_n[\boldsymbol{R}(t)]$. We assume that each $\left|\psi_n[\boldsymbol{R}(t)]\right\rangle$ is single-valued such that no two different points in $\mathbb{R}^N$ map to the same eigenstate. We note that the instantaneous eigenstates $\left|\psi_n[\boldsymbol{R}(t)]\right\rangle$ are not solutions to the time-dependent Schrödinger equation (TDSE), since at each instant in time we will have an entirely new set of eigenstates along with an entirely new Hamiltonian.

At this point we build an ansatz with the motivation that some superposition of these instantaneous eigenstates will solve the TDSE. We take our ansatz to be

$$\left|\Psi[\boldsymbol{R}(t); t]\right\rangle = \sum_n f_n[\boldsymbol{R}(t); t] \left|\psi_n[\boldsymbol{R}(t)]\right\rangle \tag{2.3}$$

where $f_n[\boldsymbol{R}(t); t]$ is some system-parameter-dependent function associated with the n^{th} eigenvector. Note that these functions can in principle have explicit time dependence even when the Hamiltonian and thus the eigenstates do not. We now substitute this into the TDSE

$$i\partial_t \left|\Psi[\boldsymbol{R}(t); t]\right\rangle = H[\boldsymbol{R}(t)] \left|\Psi[\boldsymbol{R}(t); t]\right\rangle , \tag{2.4}$$

where $\partial_t = \frac{\partial}{\partial t}$. Attempting to solve for the functions $f_m[\boldsymbol{R}(t); t]$ yields

$$\begin{aligned} i\partial_t f_m[\boldsymbol{R}(t); t] = &\left[E_m[\boldsymbol{R}(t)] - i \left\langle \psi_m[\boldsymbol{R}(t)] \right| \frac{d}{dt} \left|\psi_m[\boldsymbol{R}(t)]\right\rangle \right] f_m[\boldsymbol{R}(t); t] \\ &- i \sum_{n \neq m} f_m[\boldsymbol{R}(t); t] \left\langle \psi_m[\boldsymbol{R}(t)] \right| \frac{d}{dt} \left|\psi_n[\boldsymbol{R}(t)]\right\rangle , \end{aligned} \tag{2.5}$$

for some m in the range of values of n. In this form we see the term in the square brackets contains only information concerning the m^{th} eigenstate, and the last

term contains information on the coupling of the m^{th} eigenstate with all of the other instantaneous eigenstates at time t.

It is at this point we would like to restrict our analysis to systems with approximately adiabatic evolution such that we can neglect the last term of (2.5). The adiabatic theorem, in short, states that Hamiltonians which vary 'slowly' in time will be subject to adiabatic transformation [98–100]. More precisely, if a Hamiltonian $H[\boldsymbol{R}(t)]$ varies for times $0 \leq t \leq T$ then a wavefuntion in the system initially in an instantaneous eigenstate of $H[\boldsymbol{R}(t)]$, $|\Psi[\boldsymbol{R}(0);0]\rangle = |\psi_m[\boldsymbol{R}(0)]\rangle$, will remain in that instantaneous eigenstate with error

$$\big\| |\Psi[\boldsymbol{R}(t);t]\rangle - |\psi_m[\boldsymbol{R}(t)]\rangle \big\| \sim \mathcal{O}(\frac{1}{T}), \tag{2.6}$$

where $\|\boldsymbol{a}\| = \sqrt{\boldsymbol{a}\boldsymbol{a}*}$ is the norm of $\boldsymbol{a}$. Note that Born and Fock proved this theorem assuming a non-degenerate system [98], Tosio proved this theorem with a more general eigenstructure of the system [99].

We can see this more explicitly by differentiating (2.2)

$$\langle \psi_m[\boldsymbol{R}(t)]| \frac{d}{dt} |\psi_n[\boldsymbol{R}(t)]\rangle = \frac{\langle \psi_m[\boldsymbol{R}(t)]| \frac{d}{dt} H[\boldsymbol{R}(t)] |\psi_n[\boldsymbol{R}(t)]\rangle}{E_n[\boldsymbol{R}(t)] - E_m[\boldsymbol{R}(t)]}. \tag{2.7}$$

This implies that the timescale defining how slowly the Hamiltonian is varying is determined by the separation of each of the energy levels $E_n[\boldsymbol{R}(t)] - E_m[\boldsymbol{R}(t)]$. It is not enough to simply say that $\langle \psi_m[\boldsymbol{R}(t)]| \frac{d}{dt} H[\boldsymbol{R}(t)] |\psi_n[\boldsymbol{R}(t)]\rangle$ will be small, but more formally we require

$$\frac{\langle \psi_m[\boldsymbol{R}(t)]| \frac{d}{dt} H[\boldsymbol{R}(t)] |\psi_n[\boldsymbol{R}(t)]\rangle}{E_n[\boldsymbol{R}(t)] - E_m[\boldsymbol{R}(t)]} \ll 1. \tag{2.8}$$

If we use the convention that $E_n[\boldsymbol{R}(t)] > E_m[\boldsymbol{R}(t)]$ (in order not to have to worry about flipping the inequality) we see the requirement for slow evolution of the Hamiltonian is

$$\langle \psi_m[\boldsymbol{R}(t)]| \frac{d}{dt} H[\boldsymbol{R}(t)] |\psi_n[\boldsymbol{R}(t)]\rangle \ll E_n[\boldsymbol{R}(t)] - E_m[\boldsymbol{R}(t)]. \tag{2.9}$$

When this adiabatic approximation condition is met we consider the effect of each $\langle \psi_m[\boldsymbol{R}(t)]| \frac{d}{dt} |\psi_n[\boldsymbol{R}(t)]\rangle$ to be negligible when $n \neq m$.

Solving the now simplified version of (2.5) we find

$$f_m[\boldsymbol{R}(t);t] \approx f_m[\boldsymbol{R}(0);0] e^{-i\theta_m[\boldsymbol{R}(t)]} e^{i\gamma_m[\boldsymbol{R}(t)]}, \tag{2.10}$$

where we define

$$\theta_m[\boldsymbol{R}(t)] = \int_0^t E_m[\boldsymbol{R}(t')]dt' \tag{2.11a}$$

$$\gamma_m[\boldsymbol{R}(t)] = \int_0^t i \langle \psi_m[\boldsymbol{R}(t')]| \frac{d}{dt'} |\psi_m[\boldsymbol{R}(t')]\rangle \, dt' \tag{2.11b}$$

to be the usual *dynamical phase* and the *geometric* or *Berry phase* of the instantaneous eigenstate $|\psi_m[\boldsymbol{R}(t)]\rangle$ respectively. We know that $\theta_m[\boldsymbol{R}(t)]$ is a real number.

We now show that the same is true for $\gamma_m[\boldsymbol{R}(t)]$ as $\langle\psi_m[\boldsymbol{R}(t)]|\,\frac{d}{dt}\,|\psi_m[\boldsymbol{R}(t)]\rangle$ must be a purely imaginary number for all t. Using the chain rule we show

$$\langle\psi_m[\boldsymbol{R}(t)]|\,\frac{d}{dt}\,|\psi_m[\boldsymbol{R}(t)]\rangle = \frac{d}{dt}\,\langle\psi_m[\boldsymbol{R}(t)]|\psi_m[\boldsymbol{R}(t)]\rangle - \big(\,\langle\psi_m[\boldsymbol{R}(t)]|\,\frac{d}{dt}\,|\psi_m[\boldsymbol{R}(t)]\rangle\,\big)^*.$$

Since at any instant in time $\langle\psi_m[\boldsymbol{R}(t)]|\psi_m[\boldsymbol{R}(t)]\rangle = 1$ this implies

$$\langle\psi_m[\boldsymbol{R}(t)]|\,\frac{d}{dt}\,|\psi_m[\boldsymbol{R}(t)]\rangle + \big(\,\langle\psi_m[\boldsymbol{R}(t)]|\,\frac{d}{dt}\,|\psi_m[\boldsymbol{R}(t)]\rangle\,\big)^* = 0.$$

For any complex number z, $z + z^* = 2Re[z]$ and so $\langle\psi_m[\boldsymbol{R}(t)]|\,\frac{d}{dt}\,|\psi_m[\boldsymbol{R}(t)]\rangle$ must be purely imaginary. Finally we write our approximate adiabatic solution to the TDSE as

$$|\Psi[\boldsymbol{R}(t);t]\rangle \approx e^{-i\theta_m[\boldsymbol{R}(t)]}e^{i\gamma_m[\boldsymbol{R}(t)]}\,|\psi_m[\boldsymbol{R}(t)]\rangle\,, \tag{2.12}$$

assuming the system began in the m^{th} instantaneous eigenstate i.e. $|\Psi[\boldsymbol{R}(0);0]\rangle = |\psi_m[\boldsymbol{R}(0)]\rangle$.

2.1.2 Physical Nature of Berry's Phase

We now focus on the main results obtained by Berry in the seminal work [42] regarding the geometric phase $\gamma_m[\boldsymbol{R}(t)]$. It was this work that motivated the naming of the Berry phase. We will refer to this phase as the Berry phase from here on in. The integrand of Eq. (2.11b) can be re-written using the chain rule

$$\langle\psi_m[\boldsymbol{R}(t)]|\,\frac{d}{dt}\,|\psi_m[\boldsymbol{R}(t)]\rangle = \langle\psi_m[\boldsymbol{R}(t)]|\,\nabla_{\boldsymbol{R}}\,|\psi_m[\boldsymbol{R}(t)]\rangle\cdot\frac{d\boldsymbol{R}(t)}{dt}. \tag{2.13}$$

Where $\nabla_{\boldsymbol{R}}\,|\psi_m[\boldsymbol{R}(t)]\rangle$ is the gradient of each component of $|\psi_m[\boldsymbol{R}(t)]\rangle$ with respect to the parameter space. We can now write the Berry phase as

$$\gamma_m[\boldsymbol{R}(t)] = \int_{\boldsymbol{R}(0)}^{\boldsymbol{R}(t)} i\,\langle\psi_m[\boldsymbol{R}(t')]|\,\nabla_{\boldsymbol{R}}\,|\psi_m[\boldsymbol{R}(t')]\rangle\cdot d\boldsymbol{R}(t'), \tag{2.14}$$

which can instead be written purely in terms of a path traced in parameter space χ

$$\gamma_m(\chi) = \int_\chi \mathcal{A}_m(\boldsymbol{R})\cdot d\boldsymbol{R}, \tag{2.15}$$

where

$$\mathcal{A}_m(\boldsymbol{R}) = i\,\langle\psi_m(\boldsymbol{R})|\,\nabla_{\boldsymbol{R}}\,|\psi_m(\boldsymbol{R})\rangle \tag{2.16}$$

is known as the *Berry connection* of the m^{th} band. Thus we find that the Berry phase does not depend on time, but rather on the path traced via adiabatic evolution in parameter space.

We now want to check if the Berry phase is gauge invariant and thus observable. Beginning with the Berry connection we let $|\psi_m(\boldsymbol{R})\rangle \to |\psi'_m(\boldsymbol{R})\rangle = e^{-i\epsilon(\boldsymbol{R})}\,|\psi_m(\boldsymbol{R})\rangle$, where $\epsilon(\boldsymbol{R})$ is some real function of the parameters of the system. We find the Berry connection transforms as

$$\mathcal{A}'_m(\boldsymbol{R}) = \mathcal{A}_m(\boldsymbol{R}) + \nabla_{\boldsymbol{R}}\,\epsilon(\boldsymbol{R}). \tag{2.17}$$

So the Berry connection is not gauge invariant, and it transforms just like a vector potential from Maxwell's equations of electromagnetism.

With this result now we find that the Berry phase transforms in general as

$$\gamma'_m(\chi) = \gamma_m(\chi) + \epsilon(\boldsymbol{R}_f) - \epsilon(\boldsymbol{R}_i), \tag{2.18}$$

where $\boldsymbol{R}_{i(f)}$ is the initial (final) point of the path χ in parameter space. Finally we conclude that the Berry phase is only gauge invariant, and thus observable, if $\boldsymbol{R}_f = \boldsymbol{R}_i$. The path χ must form a closed loop in parameter space for the Berry phase to be a physical quantity.

In general the Berry phase will be zero for one-dimensional systems since to obtain a closed path one must always double back on the path itself. An exception to this case was shown to exist in 1-D solids where their crystalline structures allow eigenstates of the system to be written as Bloch states [86]. In this case the crystalline momentum k becomes a good quantum number and a non-trivial path can be traversed in the first Brilluoin zone (FBZ). Since the FBZ is topologically equivalent to a torus, and in 1-D solids we have a Hamiltonian parameterised by k such that $H(k)\left|\psi_m(k)\right\rangle = E_n(k)\left|\psi_m(k)\right\rangle$, one can obtain a non-zero Berry phase for the m^{th} energy band as

$$\gamma_m = \oint_{FBZ} i\left\langle\psi_m(k)\right| \frac{\partial}{\partial k}\left|\psi_m(k)\right\rangle dk. \tag{2.19}$$

The perturbation needed for the Hamiltonian to evolve in time may be introduced by some external vector potential that depends on time. This will lead to a time dependence in the ks such that the FBZ may be 'swept over'. It was J. Zak that first wrote down the Berry phase in 1-D solids and so it is often also referred to as the *Zak phase* in this case.

Now let us try and visualise the Berry phase. Using a 3D parameter space for illustration sake, we first re-write the Berry phase as a surface integral using Stokes' theorem

$$\gamma_m = \int_S (\nabla_{\boldsymbol{R}} \times \mathcal{A}_m(\boldsymbol{R})) \cdot \boldsymbol{n}\, d\boldsymbol{S}. \tag{2.20}$$

Here $\nabla_{\boldsymbol{R}} \times \mathcal{A}_m$ is the curl of $\mathcal{A}_m$. The integrand in (2.20) is known as the Berry curvature

$$\boldsymbol{B}_m(\boldsymbol{R}) = \nabla_{\boldsymbol{R}} \times \mathcal{A}_m(\boldsymbol{R}). \tag{2.21}$$

The Berry curvature is a 'magnetic field' in parameter space attributed to the m^{th} band. With this thinking, the Berry phase is the flux of this magnetic field normal to the surface enclosed by the adiabatic path χ [see Fig. 2.1] (a)-(c). Treating an infinite flux-tube as a puncture in the parameter space we see that the loop χ in Fig. 2.1 (a) cannot be contracted to a trivial point. A similar (but not necessarily equivalent) example is illustrated further in (d) where the loop in red is seen as a non-trivial loop on a torus geometry. In Fig. 2.1 (b) we take the case where the flux-tube remains in the parameter space, however the loop χ no longer encircles it. In this case the loop is trivial, as is the loop shown in (e), and can be contracted to a point. The precise distinction between the loops of Fig. 2.1 (a) and (b) is that their corresponding mappings from this space to say eigenspace belong to a different homotopy class. A homotopy class constitutes all mappings from one space to another which can be smoothly deformed into

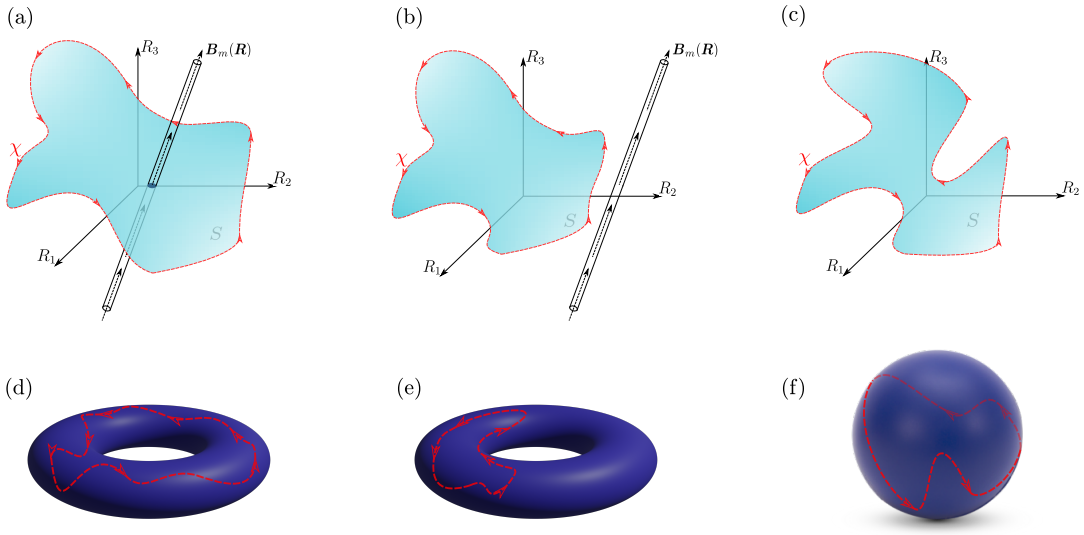

Figure 2.1: **Visualisation of the Berry Phase and Berry Curvature.** (a)-(c): Three sample loops (red dashed and arrows) in a three-dimensional parameter space enclosing a surface S (blue shading). In (a) the loop encloses a flux (the Berry curvature), in (b) the loop does not enclose a flux but a flux exists in the parameter space and in (c) there is no flux present for the loop to enclose. (d)-(f): A (similar but not exact) representation of the loops in (a)-(c) respectively on a torus or sphere geometry. The case of (a) and (d) has a loop which cannot be smoothly contracted to a point (non-trivial loop) whereas the loop in the case of (b) and (e), and (c) and (f) can be continuously deformed into a point (trivial loop).

one another. Different homotopy classes can be distinguished by their winding numbers, something we will explore in more detail in Sec. 2.1.4. Finally if we remove the flux from the system entirely as we have done for Fig. 2.1 (c), we find that there are no non-trivial loops possible in the parameter space [see similar example in Fig. 2.1 (f)]. This is expected as we will later see the correspondence between winding numbers of non-trivial loops and the existence of a non-zero Berry phase.

In the interest of understanding the Berry phase further, we note that the magnetic flux in parameter space is not generated by the adiabatic evolution of an eigenstate. Instead we should think of the Berry phase as simply a way of detecting the existence of the magnetic flux. As an illustrative example, let us take the Aharanov-Bohm effect [101]. In one setup[1] we take a particle in a box and adiabatically move it around a flux-tube perpendicular to the plane of motion until it returns to its original position. The wavefunction of the particle gains a phase

$$\gamma = \frac{q\Phi}{c}, \tag{2.22}$$

where q is the charge of the particle, c is the speed of light and Φ is the flux in the tube. The flux in this case already existed in the tube and the Berry phase was generated as a result of its existence. We have other ways of measuring the

[1]Note this is not the original idea of Aharanov and Bohm. Their idea was to split a beam of particles around a localised flux and measuring the difference in phase of these split beams.

flux due to a real magnetic field, but the Berry phase gives us a way to measure the magnetic flux in a more abstract parameter space.

2.1.3 Symmetry Classes and the Bulk-Boundary Correspondence

Probably the most important part of the Berry phase analysis is the assumption of approximate adiabatic evolution. So long as this assumption is valid, the m^{th} eigenstate of a Hamiltonian will have a Berry phase γ_m associated with it. This means that the only way the Berry phase of a given eigenstate can change is if the adiabatic approximation breaks down. We know that according to Eq. (2.7) this breakdown happens when the energy gap between eigenstates closes. If one Hamiltonian can be smoothly deformed into another Hamiltonian without closing the energy gap between the eigenstates then the same Berry phase must be attributed to the corresponding eigenstates of the new Hamiltonian. This elucidates the fact that the Berry phase is a topological invariant that can be attributed to the eigenstates of classes of Hamiltonians. These Hamiltonians are classified via the presence or absence of a series of symmetries. It is useful to note that the following are not symmetries of the model in the sense that they imply the conservation of some quantity. Despite the use of the word 'symmetry' in the literature, 'reality conditions' is probably a more accurate description as they impose conditions on the entries and structure of the Hamiltonians in a given class.

Time-reversal symmetry (TRS)

A system with TRS behaves identically whether we run the clock forwards or backwards. It is defined by an anti-unitary operator T such that

$$TH(\boldsymbol{R})T^\dagger = H(\boldsymbol{R}'), \tag{2.23}$$

where $T^\dagger$ is the Hermitian conjugate of T [72]. $\boldsymbol{R}'$ comprises the parameters that do not change under time-reversal, for example $\boldsymbol{x} \to \boldsymbol{x}$, and the time reversed version of those that do transform under the time reversal operator, for example $\boldsymbol{k} \to -\boldsymbol{k}$. The anti-unitary nature of this operator means it must take the form $T = U_T K$ where U_T is a unitary operator $U_T U_T^\dagger = \mathbb{1}$ and K is the operator of complex conjugation $KOK^\dagger = O^*$ where O is an arbitrary operator and we also note that $K^\dagger = K$.

Depending on the operator U_T, we can have either $T^2 = \pm\mathbb{1}$. In both cases it can be shown that for $H\left|\psi_n(\boldsymbol{R})\right\rangle = E_n\left|\psi_n(\boldsymbol{R})\right\rangle$,

$$H(\boldsymbol{R}')T\left|\psi_n(\boldsymbol{R})\right\rangle = TH(\boldsymbol{R})\left|\psi_n(\boldsymbol{R})\right\rangle = E_n(\boldsymbol{R})T\left|\psi_n(\boldsymbol{R})\right\rangle. \tag{2.24}$$

This means that for each eigenstate $\left|\psi_n(\boldsymbol{R})\right\rangle$ of $H(\boldsymbol{R})$, there is a state $T\left|\psi_n(\boldsymbol{R})\right\rangle = \left|\psi_n(\boldsymbol{R}')\right\rangle$ with the same energy [see Fig. 2.2(a)]. In order for $T\left|\psi_n(\boldsymbol{R})\right\rangle$ to also be an eigenstate of $H(\boldsymbol{R})$ it must be orthogonal to $\left|\psi_n(\boldsymbol{R})\right\rangle$. The anti-unitarity of T implies that for states $|\alpha\rangle$, $|\beta\rangle$, $\langle\alpha|\,T^\dagger T\left|\beta\right\rangle = \langle\alpha|\beta\rangle^* = \langle\beta|\alpha\rangle$, i.e. anti-unitary operators preserve the complex conjugate of the inner product. With this we find

$$\langle\psi_n(\boldsymbol{R})|\,T\left|\psi_n(\boldsymbol{R})\right\rangle = \langle\psi_n(\boldsymbol{R})|\,(T^\dagger)^2\,T\left|\psi_n(\boldsymbol{R})\right\rangle. \tag{2.25}$$

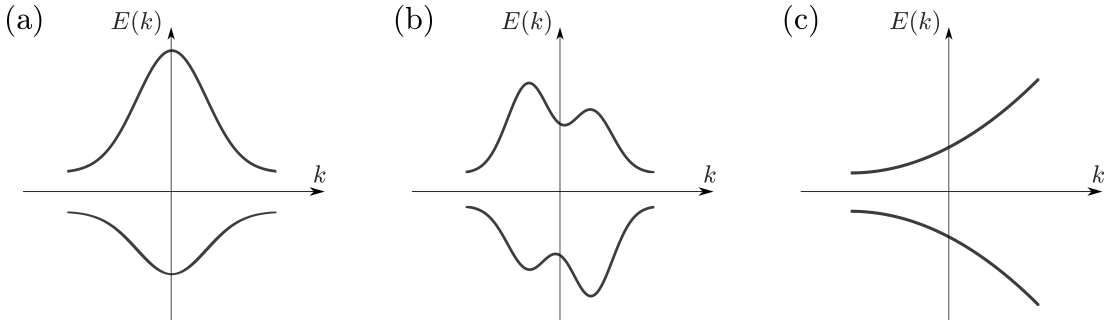

Figure 2.2: **Symmetries of Hamiltonians**. Illustration of effects of (a) TRS, (b) PHS and (c) chiral symmetry on fabricated one-dimensional, two-band, energy spectra that depend on wavevector k. (a) shows Kramer's degeneracy $E(k) = E(-k)$, in (b) we have $E(k) = -E(-k)$ and in (c) $E(k) = -E(k)$. We can work out from the sketches that if we have any two symmetries present, the third must also be present.

If $T^2 = \mathbb{1}$, there is no guarantee that the above states will be orthogonal and more work may be needed in order to ensure this. However if $T^2 = -\mathbb{1}$, the above states are guaranteed to be orthogonal and the energy eigenstates will be at least doubly degenerate, this is known as Kramer's degeneracy [72]. It is worth noting that $T^2 = \mathbb{1}$ for integer-spin particles and $T^2 = -\mathbb{1}$ for half-integer-spin particles.

Particle-Hole Symmetry (PHS)

A system with PHS, also known as charge-conjugation symmetry, behaves identically (up to a minus sign) under the replacement of particles with their corresponding holes - oppositely charged quasi-particles at positions where the particle were. PHS, like TRS, is defined by an anti-unitary operator $C = U_C K$ with U_C unitary. A Hamiltonian with PHS transforms as

$$CH(\boldsymbol{R})C^\dagger = -H(\boldsymbol{R}'). \tag{2.26}$$

Similar to the case of TRS, $\boldsymbol{R}'$ comprises the parameters left unchanged by the particle-hole operation and those that do transform under particle-hole interchange for example $\boldsymbol{k} \to -\boldsymbol{k}$. There are also two options for the square of the PHS operator $C^2 = \pm\mathbb{1}$. Once again noting the eigenvalue equation $H\left|\psi_n(\boldsymbol{R})\right\rangle = E_n\left|\psi_n(\boldsymbol{R})\right\rangle$ we find

$$H(\boldsymbol{R}')C\left|\psi_n(\boldsymbol{R})\right\rangle = -CH(\boldsymbol{R})\left|\psi_n(\boldsymbol{R})\right\rangle = -E_n(\boldsymbol{R})C\left|\psi_n(\boldsymbol{R})\right\rangle. \tag{2.27}$$

So for every eigenstate $\left|\psi_n(\boldsymbol{R})\right\rangle$ of $H(\boldsymbol{R})$, there is an eigenstate $C\left|\psi_n(\boldsymbol{R})\right\rangle = \left|\psi_n(\boldsymbol{R}')\right\rangle$ with the same but negative energy [see Fig. 2.2(b)]. This implies the eigenenergies of a Hamiltonian with PHS will be symmetric with respect to the axes of parameters that remain unchanged, and will be central-symmetric through the origin for the parameters that are reversed (i.e. pick up a minus sign). The difference between $C^2 = \pm\mathbb{1}$ is not as illustrative as that in the TRS case. $C^2 = \mathbb{1}$ corresponds to a triplet pairing Bogoliubov-de Gennes (BdG) Hamiltonian whereas $C^2 = -\mathbb{1}$ corresponds to a singlet pairing BdG Hamiltonian [68].

Symmetry				Dimension							
AZ	T	C	S	1	2	3	4	5	6	7	8
A	0	0	0	0	$\mathbb{Z}$	0	$\mathbb{Z}$	0	$\mathbb{Z}$	0	$\mathbb{Z}$
AIII	0	0	1	$\mathbb{Z}$	0	$\mathbb{Z}$	0	$\mathbb{Z}$	0	$\mathbb{Z}$	0
AI	1	0	0	0	0	0	$\mathbb{Z}$	0	$\mathbb{Z}_2$	$\mathbb{Z}_2$	$\mathbb{Z}$
BDI	1	1	1	$\mathbb{Z}$	0	0	0	$\mathbb{Z}$	0	$\mathbb{Z}_2$	$\mathbb{Z}_2$
D	0	1	0	$\mathbb{Z}_2$	$\mathbb{Z}$	0	0	0	$\mathbb{Z}$	0	$\mathbb{Z}_2$
DIII	-1	1	1	$\mathbb{Z}_2$	$\mathbb{Z}_2$	$\mathbb{Z}$	0	0	0	$\mathbb{Z}$	0
AII	-1	0	0	0	$\mathbb{Z}_2$	$\mathbb{Z}_2$	$\mathbb{Z}$	0	0	0	$\mathbb{Z}$
CII	-1	-1	1	$\mathbb{Z}$	0	$\mathbb{Z}_2$	$\mathbb{Z}_2$	$\mathbb{Z}$	0	0	0
C	0	-1	0	0	$\mathbb{Z}$	0	$\mathbb{Z}_2$	$\mathbb{Z}_2$	$\mathbb{Z}$	0	0
CI	1	-1	1	0	0	$\mathbb{Z}$	0	$\mathbb{Z}_2$	$\mathbb{Z}_2$	$\mathbb{Z}$	0

Figure 2.3: **Tenfold Way Classification**. The labels of the ten 'symmetry classes' are in the first column. The presence (± 1) or absence (0) of each symmetry is what separates the Hamiltonians into these classes, with the ± 1 corresponding to whether the operator of the given symmetry squares to ± 1 respectively. The symmetry class and dimension then dictate whether the boundary modes are protected by a $\mathbb{Z}$-type or a $\mathbb{Z}_2$-type topological insulator/superconductor. A zero in the latter columns indicates no topological protection of the boundary modes. This table was re-created from [69].

Chiral symmetry

Chiral symmetry, also known as sublattice symmetry, is the product of TRS and PHS, $S = TC$. It is possible for a Hamiltonian that does not exhibit TRS or PHS to instead be invariant (up to a minus sign) under the action of reversing time and swapping particles with their corresponding holes. The chiral symmetry operator S is unitary and transforms the Hamiltonian as

$$SH(\boldsymbol{R})S^\dagger = -H(\boldsymbol{R}). \tag{2.28}$$

We can see that for every eigenstate $|\psi_n(\boldsymbol{R})\rangle$ of $H(\boldsymbol{R})$, there is an eigenstate $S|\psi_n(\boldsymbol{R})\rangle$ with the same but negative energy [see Fig. 2.2(c)]. The unitarity of S implies that $S^2 = \mathbb{1}$ only. The name sublattice symmetry is in relation to systems with a sublattice structure. For these systems, changing the sign of the eigenstate components on one of the sublattices does not affect the overall system.

This symmetry classification was first done in the context of random matrix theory [102, 103] and is often referred to as the *tenfold way classification* due to the ten allowed combinations of the TRS, PHS and chiral symmetry, see Fig. 2.3. The classification table was extended to the context of topology, specifically fermionic topological insulators and superconductors, by Schnyder et. al. [68, 69]. Here the problem was posed as one of Anderson localisation [104], the phenomenon of delocalised eigenstates becoming increasingly localised with increasing disorder. With the knowledge that topological insulators/superconductors in d-dimensions have robust[2] $(d-1)$-dimensional delocalised boundary modes, the problem becomes one of finding out if the $(d-1)$-dimensional system can evade Anderson

[2]Robust here means against the addition of any sort of local disorder.

localisation or not. It turns out that in order to evade Anderson localisation, one must be able to add a term to the action of the model which is free from any system parameters. These terms can either be of $\mathbb{Z}_2$ or $\mathbb{Z}$ form, or simply not exist at all for a given symmetry class and dimension. The resulting $\mathbb{Z}_2$ or $\mathbb{Z}$ term from the $(d-1)$-dimensional boundary problem, if it exists, thus characterises the possible non-trivial topology of a d-dimensional topological insulator/superconductor. Further methods for calculating the same classification table were found by Kitaev [105] and Qi et. al. [106].

This work of of Schnyder and Ryu et al. used the assumed existence of robust boundary modes in order to calculate the nature of the topological invariant of the system. In practice this method is usually reversed. If we first calculate a non-zero topological invariant of the d-dimensional bulk of a fermionic material, then we expect the existence of $(d-1)$-dimensional boundary modes, also known as *edge states*, which have energies that are well separated or *gapped* from other energy levels and are robust against any sort of disorder that does not force the Hamiltonian to another symmetry class. This correspondence between non-trivial topology of the bulk of a material and the existence of robust, gapped edge states is known as the *bulk-boundary correspondence*.

2.1.4 Winding Number and the Berry Phase

The tenfold way classification is valid only for irreducible Hamiltonians, i.e. the Hamiltonian cannot be decomposed into a direct sum of lower-dimensional Hamiltonians. Since we do not always start with a Hamiltonian in an irreducible representation, we often need to find this first before classifying the topological nature of the system. For the scope of this thesis we always deal with Hamiltonians that can, in the context of topological classification, be reduced to a 2×2 diagonal block structure. We now show that for Hamiltonians with such a block structure the problem of calculating the Berry phase for each eigenstate can be reduced to solving for a winding number ν [87]. As we had alluded to in Sec. 2.1.2 [Fig. 2.1], the winding number of a closed, oriented curve in phase space is the net number of non-trivial loops traced by the curve in a counterclockwise direction. The general structure of the 2×2 reduced Hamiltonian found in our research looks like

$$H(\boldsymbol{R}) = \begin{pmatrix} n_0(\boldsymbol{R}) & n^*(\boldsymbol{R}) \\ n(\boldsymbol{R}) & n_0(\boldsymbol{R}) \end{pmatrix}, \tag{2.29}$$

where $n_0(\boldsymbol{R})$ is a real number and $n(\boldsymbol{R}) = n_x(\boldsymbol{R}) + i n_y(\boldsymbol{R})$ is in general a complex number. As the Berry phase has been shown to be time-independent, here we suppress the possible time-dependence of the parameters. Solving for the eigenstates of this system we find

$$|\psi_+(\boldsymbol{R})\rangle = \frac{1}{\sqrt{2}} \begin{pmatrix} e^{-i \arg[n(\boldsymbol{R})]} \\ 1 \end{pmatrix} \tag{2.30a}$$

$$|\psi_-(\boldsymbol{R})\rangle = \frac{1}{\sqrt{2}} \begin{pmatrix} -e^{-i \arg[n(\boldsymbol{R})]} \\ 1 \end{pmatrix}, \tag{2.30b}$$

with corresponding eigenvalues $E_\pm(\boldsymbol{R}) = n_0(\boldsymbol{R}) \pm \big|n(\boldsymbol{R})\big|$. Using equations (2.30a) and (2.30b) we can calculate the Berry connection

$$\mathcal{A}_\pm(\boldsymbol{R}) = \frac{1}{2}\nabla_{\boldsymbol{R}} \arg[n(\boldsymbol{R})]. \tag{2.31}$$

Note we used the fact that $\nabla_{\boldsymbol{R}}\{e^{i\arg[n(\boldsymbol{R})]}\} = i\, e^{i\arg[n(\boldsymbol{R})]}\, \nabla_{\boldsymbol{R}}\{\arg[n(\boldsymbol{R})]\}$. Thus we can now write down the Berry phases

$$\gamma_\pm = \frac{1}{2}\oint \nabla_{\boldsymbol{R}} \arg[n(\boldsymbol{R})] \cdot d\boldsymbol{R}, \tag{2.32}$$

where the closed integral is used such that $\gamma_\pm$ may be an observable quantity. This integral is easily evaluated as the variation of the argument of $n(\boldsymbol{R})$ around a closed curve. This variation of $\arg[n(\boldsymbol{R})]$ increases by 2π each time it encircles the origin in a counterclockwise direction. This variation of $\arg[n(\boldsymbol{R})]$ is thus the winding number of the closed path traced by the complex number $n(\boldsymbol{R})$ times 2π

$$\gamma_\pm = \frac{1}{2}(2\pi\nu) = \pi\nu. \tag{2.33}$$

The Berry phase in this case is thus quantized to integer values of π. Furthermore it is a topological invariant as it depends only on the global properties of the path traced by $n(\boldsymbol{R})$, i.e. how may times it winds around the origin, and not the local properties of the path itself. Since there is a one-to-one correspondence between the Berry phase and winding number in this case, we only concern ourselves with calculating the winding number when classifying the underlying topology. This concludes the mathematical framework needed for investigating topological phases of matter in this thesis. Next we must derive the equations describing the QED system that we will apply this framework to.

2.2 Quantum Optical Master Equation

In this section we will derive the master equation for a system of two-level atoms interacting with a cylindrical nanofiber waveguide. We follow the main steps described in [107] in order to derive the Redfield equation before deriving expressions that are unique to the system at hand. Finally the general Lindblad master equation is found and briefly studied by refining the Redfield equation to the form that will be used throughout all chapters of this thesis.

2.2.1 The Density Matrix

We begin this derivation with the most general Hamiltonian of a system interacting with a bath as depicted in Fig. 2.4(a). The possibly infinite-dimensional Hilbert space of such a system can be written as $\mathcal{H} = \mathcal{H}_S \otimes \mathcal{H}_E$ where $\mathcal{H}_S$ is the Hilbert space of the system alone and $\mathcal{H}_E$ is the Hilbert space of the environment alone with $\otimes$ denoting the Kronecker product. With this the total Hamiltonian can be written as

$$H = H_S \otimes \mathbb{1}_E + \mathbb{1}_S \otimes H_E + \alpha H_{SE}, \tag{2.34}$$

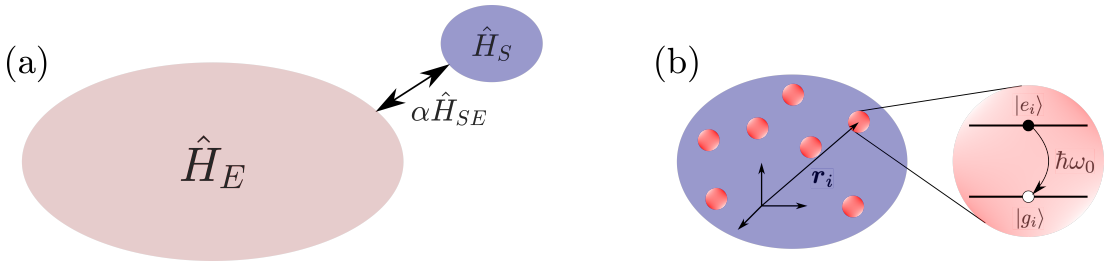

Figure 2.4: **System and Environment**. (a) Depiction of the spaces attributed to the system (governed by H_S), the environment (governed by H_E) and the interaction between them (governed by αH_{SE}). (b) A more detailed view of a system comprised of a collection of 2-level atoms each with transition energy ω_0.

where H_S (H_E) is the Hamiltonian of the system (environment) alone acting on the Hilbert space $\mathcal{H}_S$ ($\mathcal{H}_E$) and $\mathbb{1}_S$ ($\mathbb{1}_E$) is the identity operator acting on $\mathcal{H}_S$ ($\mathcal{H}_E$). Finally H_{SE} acts on the full Hilbert space $\mathcal{H} = \mathcal{H}_S \otimes \mathcal{H}_E$ and encodes the interaction between the system and environment with α being a dimensionless quantity describing the strength of the interactions.

The Schrödinger equation for the evolution of an arbitrary state $|\psi(t)\rangle$ of the full system yields the solution

$$|\psi(t)\rangle = U(t - t_0)\,|\psi(t_0)\rangle\,, \tag{2.35}$$

where $U(t - t_0) = e^{-i\int_{t_0}^{t} dt' H(t')}$ is the unitary evolution operator for a time-dependent Hamiltonian. Without loss of generality we will set $t_0 = 0$ and drop the t_0 symbol. Typically one is interested in the dynamics of the subsystem S which can be difficult to single out in the Hamiltonian formulation. Instead it is common to use the density operator formulation which allows us to view the dynamics of S alone, under the influence of the environment. The density operator, usually denoted by ρ, is defined as

$$\rho(t) = \sum_i p_i\,|\psi_i(t)\rangle\,\langle\psi_i(t)| \tag{2.36}$$

where $\{|\psi_i(t)\rangle\}$ is the set of possible quantum states that can be produced at time t and $\{p_i\}$ is the set of classical probabilities associated with the production of the quantum state $|\psi_i(t)\rangle$. We can derive the conditions that the density operator must obey in order to represent a physical system. Taking the trace of Eq. (2.36) and using the cyclic properties of the trace we find

$$tr\{\rho(t)\} = \sum_i p_i\, tr\{|\psi_i(t)\rangle\,\langle\psi_i(t)|\} = \sum_i p_i\ \langle\psi_i(t)|\psi_i(t)\rangle = \sum_i p_i = 1, \tag{2.37}$$

where $\langle\psi_i(t)|\psi_i(t)\rangle = 1$ if $|\psi_i(t)\rangle$ is normalised. So $tr\{\rho(t)\} = 1$ is the equivalent of state normalisation in the density matrix language. Next, for an arbitrary state $|\phi(t)\rangle$ we find $\langle\phi(t)|\,\rho(t)\,|\phi_i(t)\rangle = \sum_i p_i \big|\langle\phi(t)|\psi(t)\rangle\big|^2$. Interpreting this as the probability of the system being in the state $|\phi(t)\rangle$ given that the density matrix is $\rho(t)$, we require this to be non-negative i.e.

$$\langle\phi(t)|\,\rho(t)\,|\phi(t)\rangle \geq 0. \tag{2.38}$$

This is the condition of $\rho(t)$ being *positive semi-definite* and is often denoted by $\rho(t) \geq 0$. It is an equivalent statement to require all eigenvalues of $\rho(t)$ to be non-negative.

2.2.2 The Redfield Equation

The dynamics of the density operator is found via the Liouville-von Neumann equation [108]

$$\dot{\rho} = -i[H,\, \rho] \tag{2.39}$$

where the dot denotes the time derivative $\dot{O} = \frac{d}{dt}O$ and $[A, B] = AB - BA$ is the commutator of A and B. We may now write this out as

$$\dot{\rho}(t) = -i[H_S \otimes \mathbb{1}_E + \mathbb{1}_S \otimes H_E + \alpha H_{SE},\, \rho(t)]. \tag{2.40}$$

It is at this point that we rotate from the Schrödinger picture in which operators are stationary, to the interaction picture in which the density matrix as well as the interaction Hamiltonian will depend on time. This is done via the unitary operator $U_I(t) = e^{i(H_S \otimes \mathbb{1}_E + \mathbb{1}_S \otimes H_E)t}$ such that

$$\rho_I(t) = U_I(t)\rho(t)U_I^\dagger(t). \tag{2.41}$$

The equivalent of (2.40) for the interaction picture reads

$$\dot{\rho}_I(t) = -i\alpha[H_{SE}^I(t),\, \rho_I(t)], \tag{2.42}$$

where $H_{SE}^I(t) = U_I^\dagger(t)H_{SE}(t)U_I(t)$. Formally integrating (2.42) we find

$$\rho_I(t) = \rho_I(0) - i\alpha \int_0^t [H_{SE}^I(t'),\, \rho_I(t')]dt'. \tag{2.43}$$

Inserting (2.43) into (2.42) we get

$$\dot{\rho}_I(t) = -i\alpha[H_{SE}^I(t),\, \rho_I(0)] - \alpha^2[H_{SE}^I(t), \int_0^t [H_{SE}^I(t'),\, \rho_I(t')]\, dt']. \tag{2.44}$$

This equation is in general hard to solve as it requires the integration of the density operator over all previous times up to t. To overcome this, first we repeat this process of integration and substitution such that we find

$$\dot{\rho}_I(t) = -i\alpha[H_{SE}^I(t),\, \rho_I(0)] - \alpha^2[H_{SE}^I(t), \int_0^t [H_{SE}^I(t'),\, \rho_I(t)]\, dt'] + \mathcal{O}(\alpha^3). \tag{2.45}$$

It is at this point we make our first approximation. We assume that the system and environment coupling is weak such that terms in (2.45) of order $\mathcal{O}(\alpha^3)$ and above are negligible. This is known as the Born approximation and leaves us with

$$\dot{\rho}_I(t) = -i\alpha[H_{SE}^I(t),\, \rho_I(0)] - \alpha^2[H_{SE}^I(t), \int_0^t [H_{SE}^I(t'),\, \rho_I(t)]\, dt']. \tag{2.46}$$

We now want to focus on the dynamics of S. The partial trace operation allows us to 'trace out' the environment degrees of freedom and leave us only with the degrees of freedom of S. For an operator O acting on a composite space $\mathcal{H}_S \otimes \mathcal{H}_E$, the partial trace of O is defined as

$$tr_E\{O\} = \sum_e (\mathbb{1}_S \otimes \langle e|)O(\mathbb{1}_S \otimes |e\rangle) \tag{2.47a}$$

$$tr_S\{O\} = \sum_s (\langle s| \otimes \mathbb{1}_E) O (|s\rangle \otimes \mathbb{1}_E) \tag{2.47b}$$

over the subspaces $\mathcal{H}_E$ and $\mathcal{H}_S$ respectively. Here $\{|e\rangle\}$ span $\mathcal{H}_E$ and $\{|s\rangle\}$ span $\mathcal{H}_S$. If O can be written as a product of operators acting only on the individual subspaces $O = S \otimes E$ then $tr_E\{O\} = S\, tr\{E\}$ and $tr_S\{O\} = tr[S]\, E$.

Taking the partial trace over the environment and defining $tr_E\{\rho_I(t)\} = \rho_I^S(t)$ we get

$$\dot{\rho}_I^S(t) = -i\alpha\, tr_E\{[H_{SE}^I(t),\, \rho_I(0)]\} - \alpha^2\, tr_E\{[H_{SE}^I(t), \int_0^t [H_{SE}^I(t'),\, \rho_I(t)]\, dt']\}. \tag{2.48}$$

Let us now work with the first term. We assume that at $t = 0$ the full system is in a separable state $\rho_I(0) = \rho_I^S(0) \otimes \rho_I^E(0)$, that is, we assume at $t = 0$ that the system and environment have not begun to interact. Next we assume that the environment is initially in a thermal state $\rho_I^E(0) = e^{-H_E k_B T}/tr\{e^{-H_E k_B T}\}$ with T being the temperature and k_B is the Boltzmann constant. Without loss of generality we can write [109]

$$H_{SE}^I(t) = \sum_\beta S_\beta(t) \otimes E_\beta(t), \tag{2.49}$$

where S_β are operators acting on the Hilbert space of S and E_β are operators acting on the Hilbert space of the environment. This allows us to write the first term of (2.48) as

$$\begin{aligned} tr_E\{[H_{SE}^I(t),\, \rho_I(0)]\} = \sum_\beta \big(& S_\beta(t)\rho_I^S(0)\, tr_E\big\{E_\beta(t)\, \rho_I^E(0)\big\} \\ & -\rho_I^S(0) S_\beta(t)\, tr_E\big\{\rho_I^E(0)\, E_\beta(t)\big\}\big). \end{aligned} \tag{2.50}$$

If $tr_E\big\{E_\beta(t)\, \rho_I^E(0)\big\} = tr_E\big\{\rho_I^E(0)\, E_\beta(t)\big\} = \langle E_\beta(t)\rangle$ is not zero already, one can always add and subtract the term $\alpha \sum_i \langle E_\beta(t)\rangle\, S_\beta$ from H resulting in an energy shift of H_S which does not change the system dynamics, and we find

$$\begin{aligned} tr_E\{[H_{SE}^I(t) - \alpha \sum_\beta \langle E_\beta(t)\rangle\, S_\beta,\, \rho_I(0)]\} = \sum_\beta \big[& S_\beta(t)\rho_I^S(0)\, \big(\langle E_\beta(t)\rangle - \langle E_\beta(t)\rangle \big) \\ & -\rho_I^S(0) S_\beta(t)\, \big(\langle E_\beta(t)\rangle - \langle E_\beta(t)\rangle \big)\big]. \end{aligned} \tag{2.51}$$

As a result we can always neglect the first term of Eq. (2.48).

We now take the weak-coupling approximation one step further. With the assumption that α is small, we can assume that the correlation time scales and relaxation times of the environment are much shorter than that of the typical observable timescale. We thus assume we may always represent the environment as a thermal state decoupled from S such that $\rho_I(t) = \rho_I^S(t) \otimes \rho_I^E(0)$. Under this strong assumption we now have an equation of the form

$$\dot{\rho}_I^S(t) = -\alpha^2 \int_0^t dt' tr_E\{[H_{SE}^I(t), [H_{SE}^I(t'),\, \rho_I^S(t) \otimes \rho_I^E(0)]\,]\}, \tag{2.52}$$

where the integral has been taken outside the trace. Next we note that the kernel of integration decays very quickly with time. That is to say the correlations

between system and environment are so short in time the environment is often said to be 'memory-less', so that the dynamics of the system only depend on the current time and not on previous times. This allows us to extend integrals over time to infinity without significantly impacting the calculations. This is known as the Markov approximation. Changing the integration variable to $\tau = t - t'$ and extending the upper limit of τ to infinity we arrive at the well-known *Redfield equation* [109]

$$\dot{\rho}_I^S(t) = -\alpha^2 \int_0^\infty d\tau \, tr_E\{[H_{SE}^I(t), [H_{SE}^I(t-\tau), \, \rho_I^S(t) \otimes \rho_I^E(0)]\,]\}. \tag{2.53}$$

The dynamics one obtains from the Redfield equation does not ensure the positivity of the density matrix [Eq. (2.38)] for all times. As a result there is need for further approximation of the Redfield equation which will be detailed in Sec. 2.2.5.

2.2.3 Atom-Electric Field Interactions in the Dipole Approximation

We will now derive the interaction Hamiltonian in Eq. (2.53) of interest to us using the prescription set out in [110]. We are interested in studying the interactions between an ensemble of identical 2-level atoms, see Fig. 2.4(b), and an external electric field. We begin by examining a single atom with a nucleus at position $\boldsymbol{r}$ and an orbiting electron of mass m_e and charge e at position $\boldsymbol{r}_e$ relative to the nucleus. Assuming the electron is bound by a potential $V(\boldsymbol{r}_e)$, we initially let its Hamiltonian take the form

$$H_0 = \frac{\boldsymbol{p}^2}{2m_e} + V(\boldsymbol{r}_e), \tag{2.54}$$

where $\boldsymbol{p} = -i\nabla_{\boldsymbol{r}}$ is the momentum operator. The wavefunction of the electron $\psi(\boldsymbol{R}, t)$, where $\boldsymbol{R} = \boldsymbol{r} + \boldsymbol{r}_e$ is the position of the electron with respect to the origin, evolves according to the Schrödinger equation

$$H_0\psi(\boldsymbol{R}, t) = i\frac{\partial}{\partial t}\psi(\boldsymbol{R}, t). \tag{2.55}$$

This equation is invariant with respect to global gauge transformations i.e

$$\psi(\boldsymbol{R}, t) \to \psi(\boldsymbol{R}, t)e^{i\xi}, \tag{2.56}$$

where ξ is a constant phase, however it is not invariant with respect to gauge transformations

$$\psi(\boldsymbol{R}, t) \to \psi(\boldsymbol{R}, t)e^{i\xi(\boldsymbol{R},t)}, \tag{2.57}$$

where the phase $\xi(\boldsymbol{R}, t)$ is local in space and time. The requirement of local gauge invariance of the Schrödinger equation gives rise to the following necessary modifications of the Hamiltonian (2.54)

$$\boldsymbol{p} \to \boldsymbol{p} + e\boldsymbol{A}(\boldsymbol{R}, t), \tag{2.58a}$$

$$H_0 \to H_0 - e\phi(\boldsymbol{R}, t), \tag{2.58b}$$

where $\boldsymbol{A}(\boldsymbol{R},t)$ and $\phi(\boldsymbol{R},t)$ are the vector and scalar potentials respectively. Under local gauge transformations we find that these potentials must transform as $\boldsymbol{A}(\boldsymbol{R},t) \to \boldsymbol{A}(\boldsymbol{R},t)+\nabla_{\boldsymbol{r}}\xi(\boldsymbol{r},t)$ and $\phi(\boldsymbol{r},t) \to \phi(\boldsymbol{r},t)-\partial_t\xi(\boldsymbol{r},t)$ where $\nabla_{\boldsymbol{r}}\xi(\boldsymbol{r},t)$ is the gradient of $\xi(\boldsymbol{r},t)$. The potentials themselves are not gauge invariant quantities but are directly related to the gauge invariant electric and magnetic fields via

$$\boldsymbol{E}(\boldsymbol{R},t) = -\nabla_{\boldsymbol{r}}\phi(\boldsymbol{R},t) - \partial_t\boldsymbol{A}(\boldsymbol{R},t), \tag{2.59a}$$
$$\boldsymbol{B}(\boldsymbol{R},t) = \nabla_{\boldsymbol{r}} \times \boldsymbol{A}(\boldsymbol{R},t), \tag{2.59b}$$

respectively. The Hamiltonian of the electron which ensures local gauge invariance is

$$H = \frac{(\boldsymbol{p}+e\boldsymbol{A}(\boldsymbol{r},t))^2}{2m_e} - e\phi(\boldsymbol{r},t) + V(\boldsymbol{r}). \tag{2.60}$$

Choosing $\boldsymbol{A}(\boldsymbol{R},t)$, $\phi(\boldsymbol{R},t)$ and $\xi(\boldsymbol{R},t)$ is known as fixing the gauge of the problem. One convenient choice is the Coulomb gauge in which we let $\phi(\boldsymbol{R},t) = 0$ and $\nabla_{\boldsymbol{r}} \cdot \boldsymbol{A}(\boldsymbol{R},t) = 0$. Maxwell's equations yield the wave equation

$$\nabla^2_{\boldsymbol{r}}\boldsymbol{A}(\boldsymbol{R},t) - \frac{1}{c^2}\frac{\partial^2}{\partial t^2}\boldsymbol{A}(\boldsymbol{R},t) = 0, \tag{2.61}$$

where $c = 1/\sqrt{\epsilon_0\mu_0}$ is the speed of light in a vacuum with ϵ_0, μ_0 the vacuum permittivity and permeability respectively. The solution to this equation for a multi-mode field in a vacuum is the superposition of plane waves

$$\boldsymbol{A}(\boldsymbol{R},t) = \sum_{\boldsymbol{k}}\left[A^-_{\boldsymbol{k}}\boldsymbol{\epsilon}_{\boldsymbol{k}}e^{-i\omega_{\boldsymbol{k}}t} + A^+_{\boldsymbol{k}}\boldsymbol{\epsilon}_{\boldsymbol{k}}e^{i\omega_{\boldsymbol{k}}t}\right]e^{i\boldsymbol{k}\cdot\boldsymbol{R}}. \tag{2.62}$$

Here $A^{\pm}_{\boldsymbol{k}}$ are the amplitudes of the waves with wavevector $\boldsymbol{k}$, frequency $\pm\omega_{\boldsymbol{k}}$ where $|\boldsymbol{k}| = \frac{\omega_{\boldsymbol{k}}}{c}$, and $\boldsymbol{\epsilon}$ is the unit vector specifying the direction of polarisation of the wave.

Typically $\boldsymbol{r}_e$ has a magnitude of the order of a few Ångström and $\lambda = \frac{2\pi}{|\boldsymbol{k}|}$ is of the order of a few hundred nanometers such that $\boldsymbol{k}\cdot\boldsymbol{r}_e \ll 1$. Taylor expanding (2.62) around $\boldsymbol{k}\cdot\boldsymbol{r}_e = 0$ and neglecting terms above zeroth order in $\boldsymbol{k}\cdot\boldsymbol{r}_e$ we arrive at the solution

$$\boldsymbol{A}(\boldsymbol{r},t) = \sum_{\boldsymbol{k}}\left[A^-_{\boldsymbol{k}}\boldsymbol{\epsilon}_{\boldsymbol{k}}e^{-i\omega_{\boldsymbol{k}}t} + A^+_{\boldsymbol{k}}\boldsymbol{\epsilon}_{\boldsymbol{k}}e^{i\omega_{\boldsymbol{k}}t}\right]e^{i\boldsymbol{k}\cdot\boldsymbol{r}}. \tag{2.63}$$

This approximation is known as the dipole approximation. It assumes that the nucleus and electron are so close that they experience the same external field. The next step is to choose our gauge function to be

$$\xi(\boldsymbol{r},t) = -e\boldsymbol{A}(\boldsymbol{r},t)\cdot\boldsymbol{r}_e. \tag{2.64}$$

Filling all of this information back in to the locally gauge invariant Schrodinger equation we arrive at

$$[H_0 - \boldsymbol{d}\cdot\boldsymbol{E}(\boldsymbol{r},t)]\psi(\boldsymbol{R},t) = i\frac{\partial}{\partial t}\psi(\boldsymbol{R},t), \tag{2.65}$$

where $\boldsymbol{d} = e\boldsymbol{r}_e$ is known as the dipole operator of the atom.

Examining Eq. (2.65) we find that the interaction between an atom and external electromagnetic field is contained entirely within the $\boldsymbol{d} \cdot \boldsymbol{E}(\boldsymbol{r}, t)$ term. Taking the atom as the system S and the external field as the environment, this means that the interaction Hamiltonian of the previous section (in the Schrödinger picture) is

$$\alpha H_{SE} = -\boldsymbol{d} \cdot \boldsymbol{E}(\boldsymbol{r}, t). \tag{2.66}$$

The derivation above can be easily extended to include an ensemble of M atoms

$$H = \sum_{i=1}^{M} H_0^i - \sum_{i=1}^{M} \boldsymbol{d}_i \cdot \boldsymbol{E}(\boldsymbol{r}_i, t), \tag{2.67}$$

where H_0^i is the bare atom Hamiltonian for atom i and we have introduced the operator representations of the dipole transitions and electric field. Using Dirac notation we can write the dipole operator as $\boldsymbol{d}_i = \sum_{j_i k_i} |j_i\rangle \langle j_i| \boldsymbol{d}_i |k_i\rangle \langle k_i|$ where $\boldsymbol{d}_i = e\boldsymbol{r}_i$ and $\{|j_i\rangle\}$ and $\{|k_i\rangle\}$ are the eigenstates of H_0^i. In our 2-level atom system we have that $|j_i\rangle$, $|k_i\rangle \in \{|g_i\rangle, |e_i\rangle\}$, where $|g_i\rangle$ and $|e_i\rangle$ are the ground and excited state of atom i respectively, so we may write

$$\boldsymbol{d}_i = \boldsymbol{d}_i^{eg} |e_i\rangle \langle g_i| + \boldsymbol{d}_i^{ge} |g_i\rangle \langle e_i|, \tag{2.68}$$

where $\boldsymbol{d}_i^{eg} = \langle e_i| \boldsymbol{d}_i |g_i\rangle$ is the transition dipole matrix element associated with the transition from the ground state to the excited state of the i^{th} atom. The components $\boldsymbol{d}_i^{ee} = \boldsymbol{d}_i^{gg} = 0$ due to selection rules [111].

We define now $\sigma_i^+ = |e_i\rangle \langle g_i|$, the raising operator associated with the transition from the ground state to the excited state of the i^{th} atom, and $\sigma_i^- = |g_i\rangle \langle e_i|$ as the lowering operator associated with the transition from the excited state to the ground state of the i^{th} atom. Since the atoms only have one excited and ground state we add that $\sigma_i^+ |e_i\rangle = 0$ and $\sigma_i^- |g_i\rangle = 0$. Finally we write the dipole operator as

$$\boldsymbol{d}_i = \boldsymbol{d}_i^{eg} \sigma_i^+ + \boldsymbol{d}_i^{ge} \sigma_i^-. \tag{2.69}$$

We will use this form of the dipole moment operator along with the quantised electric field operator which is defined later in Sec. 2.2.5.

2.2.4 EM Field Around a Cylindrical Nanofiber

We will now derive the electromagnetic (EM) field induced by the presence of a cylindrical nanofiber waveguide of refractive index n_1 in free space ($n_2 = 1$). As depicted in Fig. 2.5 the waveguide is chosen to lie along the z-axis with radius r_{f}.

In order to derive the electromagnetic field we follow the prescription set out in [112], using the cylindrical polar coordinate basis. We can write the electric and magnetic field of frequency ω in a medium of refractive index n as

$$\boldsymbol{E}_\omega(\boldsymbol{r}, t) = \tilde{\boldsymbol{E}}(r, \phi) e^{i(\omega t - \beta z)}, \tag{2.70a}$$

$$\boldsymbol{B}_\omega(\boldsymbol{r}, t) = \tilde{\boldsymbol{B}}(r, \phi) e^{i(\omega t - \beta z)}, \tag{2.70b}$$

respectively where $\beta = nk\cos\theta$ is the propagation constant of the mode with $k = |\boldsymbol{k}|$. Here θ is the angle between the projection of $\boldsymbol{k}$ onto the z-axis and $\boldsymbol{k}$

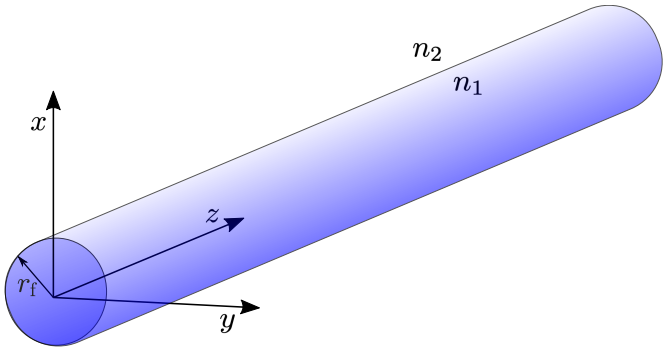

Figure 2.5: **Cylindrical Waveguide.** The cylindrical waveguide of radius r_f and uniform refractive index n_1 is surrounded by media of uniform refractive index n_2 and oriented along the z-axis.

itself and runs from $\theta \in [0, \pi]$. Maxwell's equations for a homogeneous dielectric medium read

$$\nabla_{\boldsymbol{r}} \times \boldsymbol{E}_\omega(\boldsymbol{r}, t) = -\mu \frac{\partial}{\partial t} \boldsymbol{B}_\omega(\boldsymbol{r}, t), \tag{2.71a}$$

$$\nabla_{\boldsymbol{r}} \times \boldsymbol{B}_\omega(\boldsymbol{r}, t) = \epsilon \frac{\partial}{\partial t} \boldsymbol{E}_\omega(\boldsymbol{r}, t), \tag{2.71b}$$

where μ and ϵ are the permeability and permittivity of the medium respectively and are related to the free space values by $\mu = \mu_0$ and $\epsilon = \epsilon_0 n^2$ with n the refractive index of the medium. $\nabla_{\boldsymbol{r}}$ specifies the curls are taken over the cylindrical polar coordinates[3]. We know that the electric and magnetic fields must also satisfy the wave equations[4]

$$(\nabla^2_{\boldsymbol{r}} + n^2 k^2) \boldsymbol{E}_\omega(\boldsymbol{r}, t) = 0, \tag{2.72a}$$

$$(\nabla^2_{\boldsymbol{r}} + n^2 k^2) \boldsymbol{B}_\omega(\boldsymbol{r}, t) = 0. \tag{2.72b}$$

Inputting our electric and magnetic fields into Maxwell's equations (and dropping the subscript ω) we find

$$\frac{1}{r}\frac{\partial E_z}{\partial \phi} + i\beta E_\phi = -i\omega\mu_0 B_r \tag{2.73a}$$

$$-i\beta E_r - \frac{\partial E_z}{\partial r} = -i\omega\mu_0 B_\phi \tag{2.73b}$$

$$\frac{1}{r}\frac{\partial}{\partial r}(rE_\phi) - \frac{1}{r}\frac{\partial E_r}{\partial \phi} = -i\omega\mu_0 B_z \tag{2.73c}$$

$$\frac{1}{r}\frac{\partial B_z}{\partial \phi} + i\beta B_\phi = i\omega\epsilon_0 n^2 E_r \tag{2.73d}$$

$$-i\beta B_r - \frac{\partial B_z}{\partial r} = -i\omega\epsilon_0 n^2 E_\phi \tag{2.73e}$$

$$\frac{1}{r}\frac{\partial}{\partial r}(rB_\phi) - \frac{1}{r}\frac{\partial B_r}{\partial \phi} = i\omega\epsilon_0 n^2 E_z. \tag{2.73f}$$

[3]In cylindrical polar coordinates $\nabla_{\boldsymbol{r}} \times \boldsymbol{A}(r, \phi, z) = \left(\frac{1}{r}\frac{\partial A_z}{\partial \phi} - \frac{\partial A_\phi}{\partial z}\right)\boldsymbol{r} + \left(\frac{\partial A_r}{\partial z} - \frac{\partial A_z}{\partial r}\right)\boldsymbol{\phi} + \frac{1}{r}\left(\frac{\partial}{\partial r}(rA_\phi) - \frac{\partial A_r}{\partial \phi}\right)\boldsymbol{z}$.

[4]In cylindrical polar coordinates $\nabla^2_{\boldsymbol{r}} = \frac{\partial^2}{\partial r^2} + \frac{1}{r}\frac{\partial}{\partial r} + \frac{1}{r^2}\frac{\partial^2}{\partial \phi^2} + \frac{\partial^2}{\partial z^2}$.

Combining these equations we show that E_r, E_ϕ, B_r and B_ϕ can be expressed in terms of E_z and B_z alone. As we assume homogeneity along the fiber, the refractive index must be uniform along the fiber, and may only vary with respect to the radial component i.e. $n = n(r)$ where we use the bipartite function

$$n(r) = \begin{cases} n_1 & r \leq r_\mathrm{f} \\ n_2 & r > r_\mathrm{f} \end{cases} . \tag{2.74}$$

Using the above equations we find

$$E_r = \frac{i}{\beta^2 - k^2 n^2(r)} \left[\beta \frac{\partial E_z}{\partial r} + \frac{\omega \mu_0}{r} \frac{\partial B_z}{\partial \phi} \right] \tag{2.75a}$$

$$E_\phi = \frac{i}{\beta^2 - k^2 n^2(r)} \left[\frac{\beta}{r} \frac{\partial E_z}{\partial \phi} - \omega \mu_0 \frac{\partial B_z}{\partial r} \right] \tag{2.75b}$$

$$B_r = \frac{i}{\beta^2 - k^2 n^2(r)} \left[\beta \frac{\partial B_z}{\partial r} - \frac{\omega \epsilon_0 n^2(r)}{r} \frac{\partial E_z}{\partial \phi} \right] \tag{2.75c}$$

$$B_\phi = \frac{i}{\beta^2 - k^2 n^2(r)} \left[\frac{\beta}{r} \frac{\partial B_z}{\partial \phi} + \omega \epsilon_0 n^2(r) \frac{\partial E_z}{\partial r} \right]. \tag{2.75d}$$

Since these equations only depend on E_z and B_z, solving the wave equations reduces to the following equations

$$\left[\frac{\partial^2}{\partial r^2} + \frac{1}{r^2} \frac{\partial^2}{\partial \phi^2} + \frac{1}{r} \frac{\partial}{\partial r} + \left(k^2 n^2(r) - \beta^2 \right) \right] E_z = 0 \tag{2.76a}$$

$$\left[\frac{\partial^2}{\partial r^2} + \frac{1}{r^2} \frac{\partial^2}{\partial \phi^2} + \frac{1}{r} \frac{\partial}{\partial r} + \left(k^2 n^2(r) - \beta^2 \right) \right] B_z = 0. \tag{2.76b}$$

These equations can be solved if we assume the functions E_z and B_z are separable i.e. $E_z = e(r)g(\phi)e^{i(\omega t - \beta z)}$ and $B_z = b(r)f(\phi)e^{i(\omega t - \beta z)}$. Focusing only on E_z and forcing $g(\phi)$ to be a single-valued function yields the solution $g(\phi) = e^{im\phi}$ where $m \in \mathbb{Z}$. Naturally the function $f(\phi)$ is of exactly the same form.

The solutions to the radial functions depend on the sign of $q^2 = k^2 n^2(r) - \beta^2$. If $q^2 > 0$, the solutions (one for each m) are that of a general Bessel equation [113]

$$e_m(r) = C_1 J_m(qr) + C_2 Y_m(qr), \tag{2.77}$$

where $J_m(qr)$ is the m^{th} order Bessel function of the first kind, $Y_m(qr)$ is the m^{th} order Bessel function of the second kind and C_1 and C_2 are constants. In the case that $q^2 < 0$ the solutions are now those of the equivalent modified Bessel equation

$$e_m(r) = C_3 I_m(pr) + C_4 K_m(pr), \tag{2.78}$$

where $p^2 = \beta^2 - k^2 n^2(r)$, $I_m(qr)$ is the m^{th} order modified Bessel function of the first kind, $K_m(qr)$ is the m^{th} order modified Bessel function of the second kind and C_3 and C_4 are again some constants. One can relate the Bessel functions and modified Bessel functions by

$$J_m(x) = i^m I_m(-ix), \tag{2.79a}$$

$$-\pi Y_m(x) = i^m K_m(ix) + (-i)^m K_m(-ix). \tag{2.79b}$$

We will now split the solutions above into two classes of electromagnetic modes, namely those that are confined to the nanofiber, the *guided modes*, and those which are not confined to the nanofiber, the *unguided modes*.

The Guided Modes

The cylindrical nanofiber waveguide is known to host a range of guided (g) optical modes. Inside the fiber ($r \leq r_\mathrm{f}$) the electric and magnetic field must remain finite in the limit of $r \to 0$. Given the divergence of $Y_m(qr)$ and $K_m(pr)$ in this limit we must set C_2 and C_4 to zero

$$e_m^g(r) = C_1 J_m(qr), \qquad q^2 > 0 \tag{2.80a}$$
$$e_m^g(r) = C_3 I_m(pr), \qquad p^2 > 0. \tag{2.80b}$$

Next, we expect the guided modes to be localised withing the vicinity of the waveguide and so we impose the condition that $e_m^g(r)$ and $b_m^g(r)$ must vanish in the limit of $r \to \infty$. This condition means that for $r > r_\mathrm{f}$ we must have $C_3 = 0$. So outside the fiber

$$e_m^g(r) = C_1' J_m(qr) + C_2 Y_m(qr), \qquad q^2 > 0 \tag{2.81a}$$
$$e_m^g(r) = C_4 K_m(pr), \qquad p^2 > 0. \tag{2.81b}$$

Due to the expected evanescent decay profile of the electric and magnetic fields outside the fiber we find that only $K_m(pr)$ can be a valid solution for $r > r_\mathrm{f}$. Finally we find that the $I_m(pr)$ solution inside the fiber becomes problematic when the continuity conditions are applied at the boundary of the fiber. To remedy this we set $C_3 = 0$.

Our solutions are now

$$e_m^g(r) = C_1 J_m(qr), \qquad r \leq r_\mathrm{f}, \quad q^2 > 0 \tag{2.82a}$$
$$e_m^g(r) = C_4 K_m(pr), \qquad r > r_\mathrm{f}, \quad p^2 > 0. \tag{2.82b}$$

In exactly the same way we get the solutions for the magnetic field for inside and outside the fiber

$$b_m^g(r) = D_1 J_m(qr), \qquad r \leq r_\mathrm{f}, \quad q^2 > 0 \tag{2.83a}$$
$$b_m^g(r) = D_4 K_m(pr), \qquad r > r_\mathrm{f}, \quad p^2 > 0, \tag{2.83b}$$

where D_1 and D_4 are constants analogous to C_1 and C_4. Let us note that these solutions also mean we can only have $q^2 > 0$ inside the fiber, and we can only have $p^2 > 0$ outside of the fiber. We now index the q and p terms such that $q_i^2 = k^2 n_i^2 - \beta^2$ and $p_i^2 = \beta^2 - k^2 n_i^2$ for $i = 1, 2$. We know that the guided modes are restricted to travel along the nanofiber, which means that $\theta = 0, \pi$ only. In turn $\beta = f\beta_g$ where $f = \pm 1$ denoted the z-direction of propagation and $\beta_g = kn$.

For now we will work only with the guided modes travelling in the positive z-direction. Our solutions are only in terms of q_1 and p_2 which in turn restricts the possible values for the waveguide propagation parameter within the fiber to $\beta_g^2 < k^2 n_1^2$ and outside the fiber to $\beta_g^2 > k^2 n_2^2$. Note that we have introduced β_g as the propagation constant of the guided modes only. We can now say that the propagation constant of a guided mode must lie within the range $kn_2 < \beta_g < kn_1$.

We now substitute our results for $E_{z,m}^g = e_m^g(r) e^{im\phi} e^{i(\omega t - \beta_g z)}$ and $H_{z,m}^g =$

$b_m^g(r)e^{im\phi}e^{i(\omega t-\beta_g z)}$ into (2.75). Inside the fiber ($r \leq r_\mathrm{f}$) we find

$$E_{r,m}^g = \frac{-i}{q_1^2}\left[C_1\beta_g q_1 \frac{\partial J_m(q_1 r)}{\partial(q_1 r)} + D_1 \frac{i\omega\mu_0 m}{r} J_m(q_1 r)\right] e^{im\phi}e^{i(\omega t-\beta_g z)} \tag{2.84a}$$

$$E_{\phi,m}^g = \frac{-i}{q_1^2}\left[C_1 \frac{im\beta_g}{r} J_m(q_1 r) - D_1\omega\mu_0 q_1 \frac{\partial J_m(q_1 r)}{\partial(q_1 r)}\right] e^{im\phi}e^{i(\omega t-\beta_g z)} \tag{2.84b}$$

$$E_{z,m}^g = C_1 J_m(q_1 r)\, e^{im\phi}e^{i(\omega t-\beta_g z)} \tag{2.84c}$$

$$B_{r,m}^g = \frac{-i}{q_1^2}\left[D_1\beta_g q_1 \frac{\partial J_m(q_1 r)}{\partial(q_1 r)} - C_1 \frac{i\omega\epsilon_0 n_1^2 m}{r} J_m(q_1 r)\right] e^{im\phi}e^{i(\omega t-\beta_g z)} \tag{2.84d}$$

$$B_{\phi,m}^g = \frac{-i}{q_1^2}\left[D_1 \frac{im\beta_g}{r} J_m(q_1 r) + C_1\omega\epsilon_0 n_1^2 q_1 \frac{\partial J_m(q_1 r)}{\partial(q_1 r)}\right] e^{im\phi}e^{i(\omega t-\beta_g z)} \tag{2.84e}$$

$$B_{z,m}^g = D_1 J_m(q_1 r)\, e^{im\phi}e^{i(\omega t-\beta_g z)}. \tag{2.84f}$$

Similarly outside the fiber ($r > r_\mathrm{f}$) we find

$$E_{r,m}^g = \frac{i}{p_2^2}\left[C_4\beta_g p_2 \frac{\partial K_m(p_2 r)}{\partial(p_2 r)} + D_4 \frac{i\omega\mu_0 m}{r} K_m(q_2 r)\right] e^{im\phi}e^{i(\omega t-\beta_g z)} \tag{2.85a}$$

$$E_{\phi,m}^g = \frac{i}{p_2^2}\left[C_4 \frac{im\beta_g}{r} K_m(p_2 r) - D_4\omega\mu_0 p_2 \frac{\partial K_m(p_2 r)}{\partial(p_2 r)}\right] e^{im\phi}e^{i(\omega t-\beta_g z)} \tag{2.85b}$$

$$E_{z,m}^g = C_4 K_m(p_2 r)\, e^{im\phi}e^{i(\omega t-\beta_g z)} \tag{2.85c}$$

$$B_{r,m}^g = \frac{i}{p_2^2}\left[D_4\beta_g p_2 \frac{\partial K_m(p_2 r)}{\partial(p_2 r)} - C_4 \frac{i\omega\epsilon_0 n_2^2 m}{r} K_m(p_2 r)\right] e^{im\phi}e^{i(\omega t-\beta_g z)} \tag{2.85d}$$

$$B_{\phi,m}^g = \frac{i}{p_2^2}\left[D_4 \frac{im\beta_g}{r} K_m(p_2 r) + C_4\omega\epsilon_0 n_2^2 p_2 \frac{\partial K_m(p_2 r)}{\partial(p_2 r)}\right] e^{im\phi}e^{i(\omega t-\beta_g z)} \tag{2.85e}$$

$$B_{z,m}^g = D_4 K_m(p_2 r)\, e^{im\phi}e^{i(\omega t-\beta_g z)}. \tag{2.85f}$$

The final step in this derivation is to impose continuity at the boundary $r = r_\mathrm{f}$ in the tangential field components $E_{z,m}^g$, $E_{\phi,m}^g$, $B_{z,m}^g$ and $B_{\phi,m}^g$. At $r = r_\mathrm{f}$, these conditions allow us to solve for each of the constants C_1, C_4, D_1 and D_4. This leaves us with an equation for the propagation constant entirely in terms of the system parameters

$$m^2\frac{\beta_g^2}{k^2}\left[\left(\frac{1}{q_1 r_\mathrm{f}}\right)^2 + \left(\frac{1}{p_2 r_\mathrm{f}}\right)^2\right]^2 = \left[\frac{J_m'(q_1 r_\mathrm{f})}{q_1 r_\mathrm{f} J_m(q_1 r_\mathrm{f})} + \frac{K_m'(p_2 r_\mathrm{f})}{p_2 r_\mathrm{f} K_m(p_2 r_\mathrm{f})}\right]\left[\frac{n_1^2 J_m'(q_1 r_\mathrm{f})}{q_1 r_\mathrm{f} J_m(q_1 r_\mathrm{f})} + \frac{n_2^2 K_m'(p_2 r_\mathrm{f})}{p_2 r_\mathrm{f} K_m(p_2 r_\mathrm{f})}\right]. \tag{2.86}$$

There are a discrete number of solutions to the above equation that lie in the range $kn_2 < \beta_g < kn_1$, each of which correspond to a different set of possible guided modes. Finally we recall that the solutions we have derived for the electric and magnetic field of the guided modes are not all of the solutions. In the above work we fixed the direction of guided mode propagation to be in the positive z-direction however there also exist the set of solution for a guided mode travelling in the negative z-direction, i.e. when $\beta_g \to -\beta_g$.

The Fundamental Guided Modes

We can simplify the task of solving for the electromagnetic field by restricting the number of modes in the fiber. We have already seen how the possible values

of β_g are limited by $kn_2 < \beta_g < kn_1$. Now along with (2.86) we find that β_g can only take on a finite number of values within this range. It turns out that we can limit the waveguide to only host a single set of fundamental modes, also known as the HE_{11} modes. This condition is met when

$$\frac{2\pi r_\mathrm{f}}{\lambda_\mathrm{f}}\sqrt{n_1^2 - n_2^2} < 2.4, \tag{2.87}$$

where λ_f is the wavelength of the light inside the fiber. Meeting this condition restricts the mode orders to $m = \pm 1$. In order to be consistent with the notation found in the literature we label the restricted values of m by $l = \pm 1$, which correspond to clockwise and anticlockwise polarisation of the HE_{11} modes respectively.

Dropping the mode order subscript we find that the electric field polarised in the clockwise direction and travelling in the positive z-direction has components

$$E_r^g = -iC_4\frac{\beta_g}{2q_1}\frac{K_1(p_2 r_\mathrm{f})}{J_1(qr_\mathrm{f})}\Big[(1-s)J_0(q_1 r) - (1+s)J_2(q_1 r)\Big]e^{il\phi}e^{i(\omega t - \beta_g z)} \tag{2.88a}$$

$$E_\phi^g = C_4\frac{\beta_g}{2q_1}\frac{K_1(p_2 r_\mathrm{f})}{J_1(q_1 r_\mathrm{f})}\Big[(1-s)J_0(q_1 r) + (1+s)J_2(q_1 r)\Big]e^{il\phi}e^{i(\omega t - \beta_g z)} \tag{2.88b}$$

$$E_z^g = C_4\frac{K_1(p_2 r_\mathrm{f})}{J_1(q_1 r_\mathrm{f})}J_1(q_1 r)\, e^{il\phi}e^{i(\omega t - \beta_g z)} \tag{2.88c}$$

inside the fiber.[5] Whereas outside the fiber the components simplify to

$$E_r^g = -iC_4\frac{\beta_g}{2p_2}\Big[(1-s)K_0(p_2 r) + (1+s)K_2(p_2 r)\Big]e^{il\phi}e^{i(\omega t - \beta_g z)} \tag{2.89a}$$

$$E_\phi^g = C_4\frac{\beta_g}{2p_2}\Big[(1-s)K_0(p_2 r) - (1+s)K_2(p_2 r)\Big]e^{il\phi}e^{i(\omega t - \beta_g z)} \tag{2.89b}$$

$$E_z^g = C_4 K_1(p_2 r)\, e^{il\phi}e^{i(\omega t - \beta_g z)}, \tag{2.89c}$$

where we have defined the constant

$$s = \frac{\left(\frac{1}{q_1 r_\mathrm{f}}\right)^2 + \left(\frac{1}{p_2 r_\mathrm{f}}\right)^2}{\frac{n_2^2}{p_2 r_\mathrm{f}}\frac{K_1'(p_2 r_\mathrm{f})}{K_1(p_2 r_\mathrm{f})} + \frac{n_1^2}{q_1 r_\mathrm{f}}\frac{J_1'(q_1 r_\mathrm{f})}{J_1(q_1 r_\mathrm{f})}} \tag{2.90}$$

Now we can write down the guided electric field that will be of interest to us in this thesis

$$\boldsymbol{E}^g(\boldsymbol{r}, t) = \boldsymbol{e}^{(\mu)}(r)e^{il\phi}e^{i(\omega t - f\beta_g z)}, \tag{2.91}$$

where $l = \pm 1$ once again denotes the clockwise and anticlockwise polarisation of the mode and $f = \pm 1$ denote the z-direction propagation of the fundamental guided mode. We use the notation $\mu = \omega f l$ to denote the guided mode, i.e. $\boldsymbol{e}^{(\mu)} = \Big(e_r^g,\ le_\phi^g,\ fe_z^g\Big)$ is the electric field profile function of a guided fundamental mode where each e_j^g, $j = r,\ \phi,\ z$, is just the corresponding E_j^g without the factor of $e^{il\phi}e^{i(\omega t - \beta_g z)}$. The constant C_4 is found through normalisation of the field.

[5] We have used the following identities $\frac{\partial J_m(x)}{\partial x} = \frac{1}{2}\big(J_{m-1}(x) - J_{m+1}(x)\big)$, $\frac{\partial K_m(x)}{\partial x} = -\frac{1}{2}\big(K_{m-1}(x) + K_{m+1}(x)\big)$ and $2mJ_m(x) = x\big(J_{m-1}(x) + J_{m+1}(x)\big)$, $2mK_m(x) = -x\big(K_{m-1}(x) - K_{m+1}(x)\big)$.

The Unguided Modes

The unguided modes, or radiation modes, are defined as the modes that are not restricted to the waveguide. As a result there is no restriction on the direction of propagation of the modes and so $\beta = n_2 k \cos\theta$ runs continuously in the range $[-n_2 k, n_2 k]$. Inside the fiber, the same physical conditions apply as for the guided modes. We will use the label u for parameters explicitly to do with the unguided modes. Inside the fiber we find

$$E^u_{r,m} = \frac{-i}{q_1^2}\left[A_1 \beta q \frac{\partial J_m(q_1 r)}{\partial(q_1 r)} + B_1 \frac{i\omega\mu_0 m}{r} J_m(q_1 r)\right] e^{im\phi} e^{i(\omega t - \beta z)}, \tag{2.92a}$$

$$E^u_{\phi,m} = \frac{-i}{q_1^2}\left[A_1 \frac{im\beta}{r} J_m(q_1 r) - B_1 \omega\mu_0 q \frac{\partial J_m(q_1 r)}{\partial(q_1 r)}\right] e^{im\phi} e^{i(\omega t - \beta z)}, \tag{2.92b}$$

$$E^u_{z,m} = A_1 J_m(q_1 r)\, e^{im\phi} e^{i(\omega t - \beta z)}, \tag{2.92c}$$

where A_1 and B_1 are constants. When we move outside the waveguide now we do not need the fields to decay exponentially from the boundary. We may still neglect the modified Bessel function of the first kind solution as it diverges in the limit of $r \to \infty$. Now we can write compact solutions of the electric field for of the unguided modes outside the fiber and in the allowed range of propagation constants as

$$E^u_{r,m} = \frac{-i}{q_2^2} \sum_{j=1,2} \left[C_j \beta q_2 \frac{\partial H_m^{(j)}(q_2 r)}{\partial(q_2 r)} + D_j \frac{i\omega\mu_0 m}{r} H_m^{(j)}(q_2 r)\right] e^{im\phi} e^{i(\omega t - \beta z)} \tag{2.93a}$$

$$E^u_{\phi,m} = \frac{-i}{q_2^2} \sum_{j=1,2} \left[C_j \frac{im\beta}{r} H_m^{(j)}(q_2 r) - D_j \omega\mu_0 q_2 \frac{\partial H_m^{(j)}(q_2 r)}{\partial(q_2 r)}\right] e^{im\phi} e^{i(\omega t - \beta z)} \tag{2.93b}$$

$$E^u_{z,m} = \sum_{j=1,2} C_j H_m^{(j)}(q_2 r)\, e^{im\phi} e^{i(\omega t - \beta z)}, \tag{2.93c}$$

where $H_m^{(j)}(x) = J_m(x) - (-1)^j\, Y_m(x)$ is the Hankel function of the j^{th} kind for $j = 1, 2$. Once again imposing the continuity equations at the boundary of the waveguide we find

$$C_j = (-1)^j \frac{i\pi q_2^2 r_\text{f}}{4n_2^2}\left[i\mu_0 c B V_j + A L_j\right] \tag{2.94a}$$

$$D_j = (-1)^{j-1} \frac{i\pi q_2^2 r_\text{f}}{4}\left[i\epsilon_0 c A V_j - B M_j\right] \tag{2.94b}$$

where we have defined

$$V_j = \frac{m\beta k}{r_\text{f} q_1^2 q_2^2}\left(n_2^2 - n_1^2\right) J_m(q_1 r_\text{f}) H_m^{(j)*}(q_2 r_\text{f}) \tag{2.95a}$$

$$L_j = \frac{n_1^2}{q_1} J'_m(q_1 r_\text{f}) H_m^{(j)*}(q_2 r_\text{f}) - \frac{n_2^2}{q_2} J_m(q_1 r_\text{f}) H_m^{'(j)*}(q_2 r_\text{f}) \tag{2.95b}$$

$$M_j = \frac{1}{q_1} J'_m(q_1 r_\text{f}) H_m^{(j)*}(q_2 r_\text{f}) - \frac{1}{q_2} J_m(q_1 r_\text{f}) H_m^{'(j)*}(q_2 r_\text{f}). \tag{2.95c}$$

Note that we used the result $H_m^{(1)}(q_2 r_\text{f}) H_m^{'(2)}(q_2 r_\text{f}) - H_m^{(2)}(q_2 r_\text{f}) H_m^{'(1)}(q_2 r_\text{f}) = \frac{4i}{\pi q_2 r_\text{f}}$ from [114]. We have also suppressed the m index which should be included in the

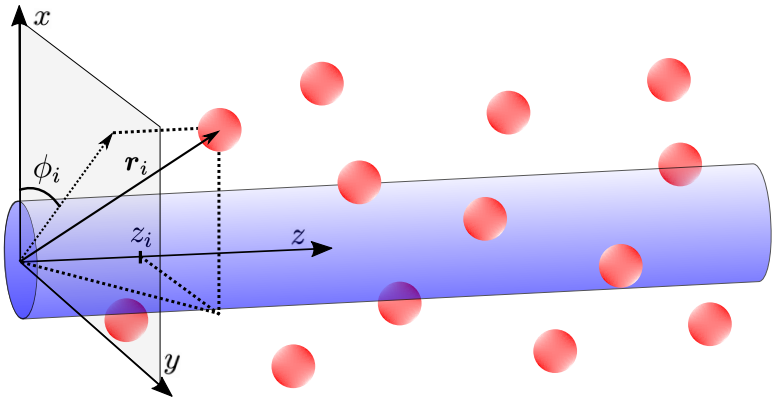

Figure 2.6: **Atom-Waveguide QED.** Ensemble of identical two-level atoms in the vicinity of the nanofiber waveguide. Also drawn is z_i, the z-component of the position of atom i and ϕ_i the azimuthal angle of atom i defined by the angle of the projection of $\boldsymbol{r}_i$ in the $x-y$ plane. In general the atoms will interact with one another through both the waveguide and through free space.

expressions defined in equations (2.94)-(2.95) for neatness. The final step here is to let $B_1 = il\eta A_1$ where the $l = \pm 1$ corresponds to clockwise/anticlockwise polarisation of the mode respectively where

$$\eta = \epsilon_0 c \sqrt{\frac{n_2^2 \left|V_j\right|^2 + \left|L_j\right|^2}{\left|V_j\right|^2 + n_2^2 \left|M_j\right|^2}}. \tag{2.96}$$

The normalisation of the electric field operators allows us to find the final constant as it imposes the condition

$$\frac{8\pi\omega}{q_2^2}\left(n_2^2 \left|C_j\right|^2 + \frac{\mu_0}{\epsilon_0}\left|D_j\right|^2\right) = 1. \tag{2.97}$$

We introduce a labelling here for the radiation modes $\nu = \omega\beta ml$ such that we can write the electric field of the unguided mode with frequency ω as

$$\boldsymbol{E}_m^u(\boldsymbol{r}, t) = \boldsymbol{e}^{(\nu)}(r) e^{im\phi} e^{i(\omega t - \beta z)}, \tag{2.98}$$

where $\boldsymbol{e}^{(\nu)}(r) = \left(e_r^u, \quad e_\phi^u, \quad e_z^u\right)$ is the electric field profile function of the unguided modes and each e_j^u, $j = r,\ \phi,\ z$, is just the corresponding E_j^u without the factor of $e^{im\phi} e^{i(\omega t - \beta_g z)}$.

2.2.5 Master Equation for Atoms Coupled to a Cylindrical Waveguide

We are now in a position to derive the master equation specific to our research, namely that of an ensemble of identical two-level atoms surrounding the optical nanofiber [see Fig. 2.6]. The electric field operator can be split into the components corresponding to the guided modes of the fiber and those corresponding to the radiation modes

$$\boldsymbol{E}(\boldsymbol{r}_i, t) = \boldsymbol{E}^g(\boldsymbol{r}_i, t) + \boldsymbol{E}^u(\boldsymbol{r}_i, t). \tag{2.99}$$

As is done in [14, 115] the electric field operator is found by quantising the bosonic field in both the guided and unguided modes in the cylindrical coordinate basis. The guided and unguided components of the electric field can also be split into their positive and negative frequency parts where $\boldsymbol{E}^{g(u)}(\boldsymbol{r}_i,t) = \boldsymbol{E}^{g(u)}_{+}(\boldsymbol{r}_i,t) + \boldsymbol{E}^{g(u)}_{-}(\boldsymbol{r}_i,t)$ and $\boldsymbol{E}^{g(u)}_{+}(\boldsymbol{r}_i,t) = \big[\boldsymbol{E}^{g(u)}_{-}(\boldsymbol{r}_i,t)\big]^\dagger$. The solutions for the positive frequency parts of the electric field, with $n_2 = 1$, in the interaction picture are

$$\boldsymbol{E}^{g}_{+}(\boldsymbol{r}_i,t) = i\int_0^\infty d\omega \sum_{fl}\sqrt{\frac{\omega\beta'_g}{4\pi\epsilon_0}}\, a_\mu \boldsymbol{e}^{(\mu)}(r)e^{-i(\omega t-\beta_g f z_i - l\phi_i)}, \tag{2.100a}$$

$$\boldsymbol{E}^{u}_{+}(\boldsymbol{r}_i,t) = i\int_0^\infty d\omega \int_{-k}^{k} d\beta \sum_{ml}\sqrt{\frac{\omega}{4\pi\epsilon_0}}\, a_\nu \boldsymbol{e}^{(\nu)}(r)e^{-i(\omega t-\beta z_i - m\phi_i)}. \tag{2.100b}$$

Here $a_{\omega fl}$ is the bosonic annihilation field operator of a guided photon which obeys the continuous-mode bosonic commutation relations $[a_\mu, a^\dagger_{\mu'}] = \delta(\omega-\omega')\delta_{ff'}\delta_{ll'}$. $\boldsymbol{e}^{(\mu)}(r)$ is the electric field profile function of the guided modes derived in Sec. 2.2.4, $\beta'_g = \frac{d\beta_g}{d\omega}$, z_i is the z-position of atom i and ϕ_i is the azimuthal angle of atom i. In the case of the radiation modes the mode order $m = 0, \pm1, \pm2, ..., \pm\infty$. a_ν is the bosonic annihilation field operator of an unguided photon of order m which also obeys the continuous-mode bosonic commutation relations $[a_\nu, a^\dagger_{\nu'}] = \delta(\omega-\omega')\delta(\beta-\beta')\delta_{mm'}\delta_{ll'}$. $\boldsymbol{e}^{(\nu)}(r)$ is the electric field profile function of the unguided modes derived in Sec. 2.2.4.

Returning to the atom-field interaction Hamiltonian, we will assume that each of the atomic dipoles are aligned such that in the interaction picture we find[6]

$$\alpha H^I_{SE}(t) = -\sum_{i=1}^{N}(\boldsymbol{d}^*\sigma_i^- e^{-i\omega_0 t} + \boldsymbol{d}\sigma_i^+ e^{i\omega_0 t})\cdot\boldsymbol{E}(\boldsymbol{r}_i,t), \tag{2.101}$$

where we have used the fact that $\boldsymbol{d}^{eg} = (\boldsymbol{d}^{ge})^* = \boldsymbol{d}$. It is convenient to write our expressions using a generalised sum $\sum_\eta = \sum_\mu + \sum_\nu$ where $\sum_\mu = \int_0^\infty d\omega \sum_{fl}$ and $\sum_\nu = \int_0^\infty d\omega \int_{-k}^{k} d\beta \sum_{ml}$ such that we can re-write (2.101) as

$$\begin{aligned}\alpha H^I_{SE}(t) = -i\sum_{i=1}^{N}\sum_{\eta}\Big[&\tilde{G}_{\eta i}\sigma_i^- a_\eta e^{-i(\omega_0+\omega)t} + \tilde{G}^*_{\eta i}\sigma_i^+ a^\dagger_\eta e^{i(\omega_0+\omega)t} \\ &+ G_{\eta i}\sigma_i^+ a_\eta e^{i(\omega_0-\omega)t} + G^*_{\eta i}\sigma_i^- a^\dagger_\eta e^{-i(\omega_0-\omega)t}\Big]\end{aligned} \tag{2.102}$$

where we have let

$$G_{\mu i} = \sqrt{\frac{\omega\beta'}{4\pi\epsilon_0}}\big[\boldsymbol{d}_i\cdot\boldsymbol{e}^{(\mu)}\big]e^{i(f\beta_g z_i + l\phi_i)}, \tag{2.103a}$$

$$G_{\nu i} = \sqrt{\frac{\omega}{4\pi\epsilon_0}}\big[\boldsymbol{d}_i\cdot\boldsymbol{e}^{(\nu)}\big]e^{i(\beta z_i + m\phi_i)}. \tag{2.103b}$$

[6]Note that the transformation of $\sigma_i^\pm$ is found using the Baker–Campbell–Hausdorff formula $e^{aA}Be^{-aA} = B + a[A,B] + \frac{a^2}{2!}[A,[A,B]]] + ...$

In order to get $\tilde{G}_{\mu i}$ or $\tilde{G}_{\nu i}$ one simply replaces the dipole moment with its complex conjugate in the above expressions. Since the atomic and field operators commute, when (2.102) is substituted into the Redfield equation (2.53) we can collect the atomic degrees of freedom and the environment degrees of freedom separately. Furthermore we can now take the partial trace operation over just the environment as we need. We end up with terms of the form $tr_E\{a_\eta a_{\eta'}\rho_I^E(0)\} = \langle a_\eta a_{\eta'}\rangle$, $tr_E\{a_\eta^\dagger a_{\eta'}^\dagger\rho_I^E(0)\} = \langle a_\eta^\dagger a_{\eta'}^\dagger\rangle$, $tr_E\{a_\eta^\dagger a_{\eta'}\rho_I^E(0)\} = \langle a_\eta^\dagger a_{\eta'}\rangle$ and $tr_E\{a_\eta a_{\eta'}^\dagger\rho_I^E(0)\} = \langle a_\eta a_{\eta'}^\dagger\rangle$ where $\langle O\rangle$ is the expectation value of the operator O in the environment. Since we assumed the environment is in a thermal equilibrium state in Sec. 2.2.2 this means that

$$\langle a_\eta a_{\eta'}\rangle = \langle a_\eta^\dagger a_{\eta'}^\dagger\rangle = 0, \tag{2.104a}$$

$$\langle a_\eta^\dagger a_{\eta'}\rangle = \bar{n}_\eta\delta_{\eta\eta'}, \tag{2.104b}$$

$$\langle a_\eta a_{\eta'}^\dagger\rangle = \big(\bar{n}_\eta + 1\big)\delta_{\eta\eta'}, \tag{2.104c}$$

where $\bar{n}_\eta$ is the average photon number. Close to zero temperature $\bar{n}_\eta$ tends to zero and so the only expectation value that survives is $\langle a_\eta a_{\eta'}^\dagger\rangle = \delta_{\eta\eta'}$. Note that the functions $\delta_{\eta\eta'}$ include both continuous and discrete Dirac delta functions as seen in the commutation relations above. Substituting this result and (2.102) into the Redfield equation (2.53), and applying the secular approximation, in which we assume that the 'fast-oscillating' terms, those with factors of $e^{\pm i2\omega_0 t}$, will average to zero in the timescales we are interested in. We find

$$\begin{aligned}\dot{\rho}_I^S(t) = \sum_{ij\eta}\int_0^\infty d\tau\Big[&\tilde{G}_{\eta i}\tilde{G}_{\eta j}^*\sigma_i^-\sigma_j^+\rho_I^S(t)e^{i(\omega+\omega_0)\tau} - \tilde{G}_{\eta i}^*\tilde{G}_{\eta j}\sigma_i^+\rho_I^S(t)\sigma_j^-e^{-i(\omega+\omega_0)\tau}\\ &- \tilde{G}_{\eta i}^*\tilde{G}_{\eta j}\sigma_i^+\rho_I^S(t)\sigma_j^-e^{i(\omega+\omega_0)\tau} + \tilde{G}_{\eta i}\tilde{G}_{\eta j}^*\rho_I^S(t)\sigma_i^-\sigma_j^+e^{-i(\omega+\omega_0)\tau}\\ &+ G_{\eta i}G_{\eta j}^*\sigma_i^-\sigma_j^+\rho_I^S(t)e^{-i(\omega-\omega_0)\tau} - G_{\eta i}^*G_{\eta j}\sigma_i^-\rho_I^S(t)\sigma_j^+e^{i(\omega-\omega_0)\tau}\\ &- G_{\eta i}^*G_{\eta j}\sigma_i^-\rho_I^S(t)\sigma_j^+e^{-i(\omega-\omega_0)\tau} + G_{\eta i}G_{\eta j}^*\rho_I^S(t)\sigma_i^-\sigma_j^+e^{i(\omega-\omega_0)\tau}\Big].\end{aligned} \tag{2.105}$$

The dynamics generated by the above master equation does ensure the positivity of the density matrix which was lacking from the Redfield equation. This is known as the *Lindblad master equation*.

Our next step is to perform the integral over τ noting that $\int_0^\infty d\tau e^{ix\tau} = \zeta(x) = \pi\delta(x) + i\mathcal{P}\frac{1}{x}$ where $\zeta(x)$ is the Heitler zeta function [116] and $\mathcal{P}$ is the Cauchy principal value. Collecting the terms with or without tildes and swapping indices i and j where needed we find

$$\begin{aligned}\dot{\rho}_I^S(t) =& i\mathcal{P}\sum_{ij\eta}\left[\frac{G_{\eta i}G_{\eta j}^*}{\omega-\omega_0}[\sigma_i^+\sigma_j^-,\rho_I^S(t)] + \frac{\tilde{G}_{\eta j}\tilde{G}_{\eta i}^*}{\omega+\omega_0}[\sigma_j^-\sigma_i^+,\rho_I^S(t)]\right]\\ &- \sum_{ij\eta}G_{\eta i}G_{\eta j}^*\pi\delta(\omega-\omega_0)\Big[\big\{\sigma_i^+\sigma_j^-,\rho_I^S(t)\big\} - 2\sigma_j^-\rho_I^S(t)\sigma_i^+\Big].\end{aligned} \tag{2.106}$$

Next we examine the commutation relations of the spin operators $[\sigma_i^+,\sigma_j^-] = \delta_{ij}\sigma_i^z$. In this thesis we will only concern ourselves with ensembles of atoms which are all at the same radial height from the surface of the nanofiber. As a result we

can absorb the potential coming from each of the σ_i^z terms into the bare atomic frequency. This allows us to write the Lindblad master equation in the form

$$\dot{\rho}_I^S(t) = -i\sum_{i\neq j} V_{ij}[\sigma_i^+\sigma_j^-, \rho_I^S(t)] + \sum_{ij}\Gamma_{ij}\big(\sigma_j^-\rho_I^S(t)\,\sigma_i^+ - \frac{1}{2}\big\{\sigma_i^+\sigma_j^-, \rho_I^S(t)\big\}\big), \quad (2.107)$$

where we have defined

$$V_{ij} = -\mathcal{P}\sum_\eta\left[\frac{G_{\eta j}^* G_{\eta i}}{\omega-\omega_0} + \frac{\tilde{G}_{\eta j}\tilde{G}_{\eta i}^*}{\omega+\omega_0}\right], \quad (2.108a)$$

$$\Gamma_{ij} = 2\pi\sum_\eta G_{\eta i}G_{\eta j}^*\delta(\omega-\omega_0). \quad (2.108b)$$

We note that $V_{ij}^* = V_{ji}$ and $\Gamma_{ij}^* = \Gamma_{ij}$. The first term of the Lindblad master equation describes the induced coherent dipole-dipole interactions mediated by exchange of virtual photons, which occur at a rate V_{ij} between the i-th and j-th atom. The second term describes the dissipative dynamics of the system, in our case this describes how photons are emitted into the environment. We note that the Lindblad master equation is often written in terms of the superoperator $\mathcal{L}$ as $\dot{\rho}_I^S(t) = \mathcal{L}\rho_I^S(t)$.

We now look in more detail at the V_{ij} and Γ_{ij} coefficients. When the fiber is not present and the atoms are in free space only, these coupling coefficients take the form

$$V_{ij}^0 = \frac{3\Gamma^0}{4}\left[y_0(k_0r_{ij}) - \frac{y_1(k_0r_{ij})}{(k_0r_{ij})} + y_2(k_0r_{ij})(\boldsymbol{d}\cdot\boldsymbol{r}_{ij})^2\right], \quad (2.109a)$$

$$\Gamma_{ij}^0 = \frac{3\Gamma^0}{2}\left[j_0(k_0r_{ij}) - \frac{j_1(k_0r_{ij})}{(k_0r_{ij})} + j_2(k_0r_{ij})(\boldsymbol{d}\cdot\boldsymbol{r}_{ij})^2\right], \quad (2.109b)$$

where $\Gamma^0 = \frac{d^2k_0^2}{3\pi\epsilon_0}$ is the single-atom spontaneous decay rate in a vacuum with $d = |\boldsymbol{d}|$, $k_0 = \frac{\omega_0}{c}$, $r_{ij} = |\boldsymbol{r}_{ij}| = |\boldsymbol{r}_i - \boldsymbol{r}_j|$ and $j_m(x)$, $y_m(x)$ are the spherical Bessel functions of the first and second kind of order m respectively. In the limit of zero separation between atoms ($r_{ij}\to 0$) the coherent interactions diverge since we can not physically place one atom on top of another. In this limit we also retain the single-atom spontaneous decay rate from the dissipative interactions. In the limit of infinite separation between atoms ($r_{ij}\to\infty$) both coherent and dissipative interactions decay to zero and, as one might expect, the atoms behave as though they were alone.

When the atoms are placed in the vicinity of the nanofiber, the quantised electric field solutions, Eqs. (2.100), allow us to split the coefficients into their guided and unguided components [see Fig. 2.7] i.e.

$$V_{ij} = V_{ij}^g + V_{ij}^u, \quad (2.110a)$$

$$\Gamma_{ij} = \Gamma_{ij}^g + \Gamma_{ij}^u. \quad (2.110b)$$

First we will look at the Γ_{ij} coefficients. The guided contribution when the general sum is expanded looks like

$$\Gamma_{ij}^g = 2\pi\sum_{fl}\int_0^\infty d\omega\, G_{\mu i}G_{\mu j}^*\delta(\omega-\omega_0). \quad (2.111)$$

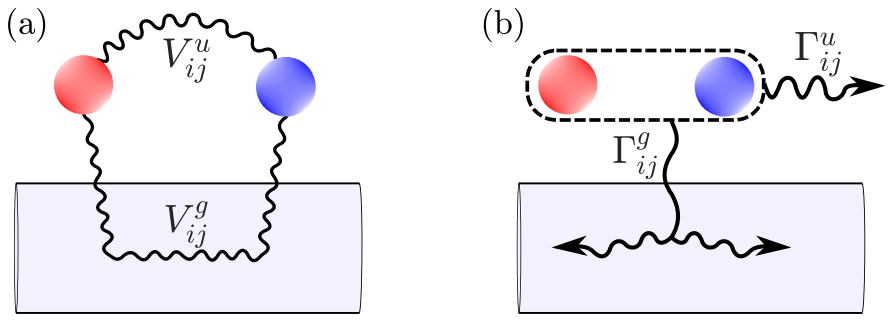

Figure 2.7: **Interaction Schematics. (a)**: A depiction of the coherent dipole-dipole interactions between atom i and j through both the guided modes (V_{ij}^g) and the unguided modes (V_{ij}^u). **(b)**: A depiction of how atom i and j collectively emit photons into the guided modes of the nanofiber at a rate Γ_{ij}^g and into the unguided modes of the environment at a rate Γ_{ij}^u.

As we work only in the domain of $\omega \geq 0$ this integral yields the solution

$$\Gamma_{ij}^g = 2\pi \sum_{fl} G_{\mu_0 i} G_{\mu_0 j}^*, \tag{2.112}$$

where $G_{\mu_0 i} = G_{\mu i}\big|_{\omega=\omega_0}$. The Γ_{ij}^u components cannot be fully solved analytically. Evaluating the integral over ω we find

$$\Gamma_{ij}^u = 2\pi \sum_{ml} \int_{-k_0}^{k_0} d\beta \, G_{\nu_0 i} G_{\nu_0 j}^*, \tag{2.113}$$

where $G_{\nu_0 i} = G_{\nu i}\big|_{\omega=\omega_0}$. Note that the sum over the mode order m theoretically extends from $-\infty$ to ∞, however in practice we apply a suitable truncation such that higher order modes do not contain any significant contributions to Γ_{ij}^u. Finally the integral over β is performed numerically in order to calculate Γ_{ij}^u.

Now we look at the coherent dipole interaction coefficients V_{ij}. Taking only the guided contributions we find

$$V_{ij}^g = -\mathcal{P} \sum_{fl} \int_0^\infty d\omega \left[\frac{G_{\mu j}^* G_{\mu i}}{\omega - \omega_0} + \frac{\tilde{G}_{\mu j} \tilde{G}_{\mu i}^*}{\omega + \omega_0} \right]. \tag{2.114}$$

We make use of the relation $-\tilde{G}_{\omega f l j}\, \tilde{G}_{\omega f l i}^* = G_{-\omega,f,-l,i}\, G_{-\omega,f,-l,j}^*$ which follows from the fact that $\beta(-\omega) = -\beta(\omega)$ and $\boldsymbol{e}^{(-\omega,f,-l)} = \boldsymbol{e}^{(\omega f l)*}$. This allows us to re-write the integral as

$$V_{ij}^g = -\mathcal{P} \sum_{fl} \int_{-\infty}^\infty d\omega \, \frac{G_{\mu j}^* G_{\mu i}}{\omega - \omega_0}. \tag{2.115}$$

As is done in [115], we assume that the main ω dependence of the $G_{\mu j}^* G_{\mu i}$ term is within the $e^{if\beta z_{ij}}$ factor, where $z_{ij} = z_i - z_j$. We can then apply contour integral methods to solve for

$$V_{ij}^g = -i\pi \sum_{fl} \mathrm{sgn}(f z_{ij}) G_{\mu_0 j}^* G_{\mu_0 i}, \tag{2.116}$$

where $\mathrm{sgn}(fz_{ij})$ accounts for the contour being in the upper-half or lower-half plane. The last term left to calculate is V_{ij}^{u}. Despite the fact an exact numerical calculation for this has been used, for example, in [117, 118], here we make use of the approximation

$$V_{ij}^{u} \approx \frac{\Gamma_{ii}^{u}}{\Gamma^{0}} V_{ij}^{0}, \tag{2.117}$$

where Γ_{ii}^{u} is the single atom decay rate into the radiation modes from Eq. (2.113). This approximation works well when the atoms are sufficiently far from the nanofiber surface.

It is convenient to write the second term of the Lindblad master equation in the diagonal form $\sum_n \Gamma_n \big(J_n^- \rho(t)\, J_n^+ - \frac{1}{2} \big\{ J_n^+ J_n^-, \rho(t) \big\} \big)$ where the $J_n^{\pm}$ are the operators of the natural decay modes of the system with a decay rate Γ_n. These operators are defined as a superposition of the single-atom operators $J_n^- = \sum_j D_{nj} \sigma_j^-$ and $J_n^+ = \sum_j D_{jn}^* \sigma_j^+$ where the matrix of D_{ij} values diagonalises the matrix containing the values Γ_{xy}. Each of the decay processes involve all of the atoms in the system and so we refer to $J_n^{\pm}$ and Γ_n as the *collective jump operators* and *collective decay rates* respectively. If the matrix containing the Γ_{ij} decay rates is already a diagonal matrix then the collective decay rates are simply equal to the single-atom decay rate $\Gamma_{ii} = \gamma$. This implies that the collective nature of the emission is encoded in the off-diagonal elements Γ_{ij} (where $i \neq j$) - the larger the off-diagonal values of the matrix, the more pronounced the collective character of the emission. A collective decay mode can in principle have a decay rate which is larger than the single-atom decay rate $\Gamma_n > \gamma$. This is referred to as a *superradiant* mode. In the reverse situation a collective decay mode can have a decay rate smaller than the single-atom decay rate $\Gamma_n < \gamma$. This is referred to as a *subradiant* mode. In the most extreme case collective modes may have zero decay rates $\Gamma_n = 0$. In much the same way, the coherent interactions between atoms are also naturally collective.

We will now use a simple system of two atoms in the vicinity of the nanofiber to illustrate how the introduction of the nanofiber alters the free space coherent and dissipative interactions between the atoms, as well as how the separation between atoms affects their interactions. We will do this (separately) for atomic dipole moments that are linearly polarised, as seen in Fig. 2.8 (a), and circularly polarised, as seen in Fig. 2.8 (b). In Fig. 2.8 (c) we find that the coherent interactions are reduced when the atoms are near the fiber for both dipole polarisations. As the atoms move far away from the surface of the nanofiber we see the fiber has less of an effect on the coherent interactions as they converge towards their corresponding free space values. Interestingly the imaginary part of of the coherent interactions for circularly polarised dipoles is only present when the atoms are near the fiber, suggesting the nanofiber induces more complex interactions between the atoms. In Fig. 2.8 (d) we find that the dissipative interactions between pairs of atoms with either dipole orientation increase dramatically when the atoms are near to the nanofiber surface. As the atoms move further from the surface of the nanofiber the dissipative interactions tend towards their corresponding free space values. Since the collective decay rates in this simple system take the form $\gamma_{\pm} = \gamma \pm |\Gamma_{12}|$ we can see, for example, that when the atoms are placed close to the surface of the nanofiber the decay from the atoms becomes more collective inherently.

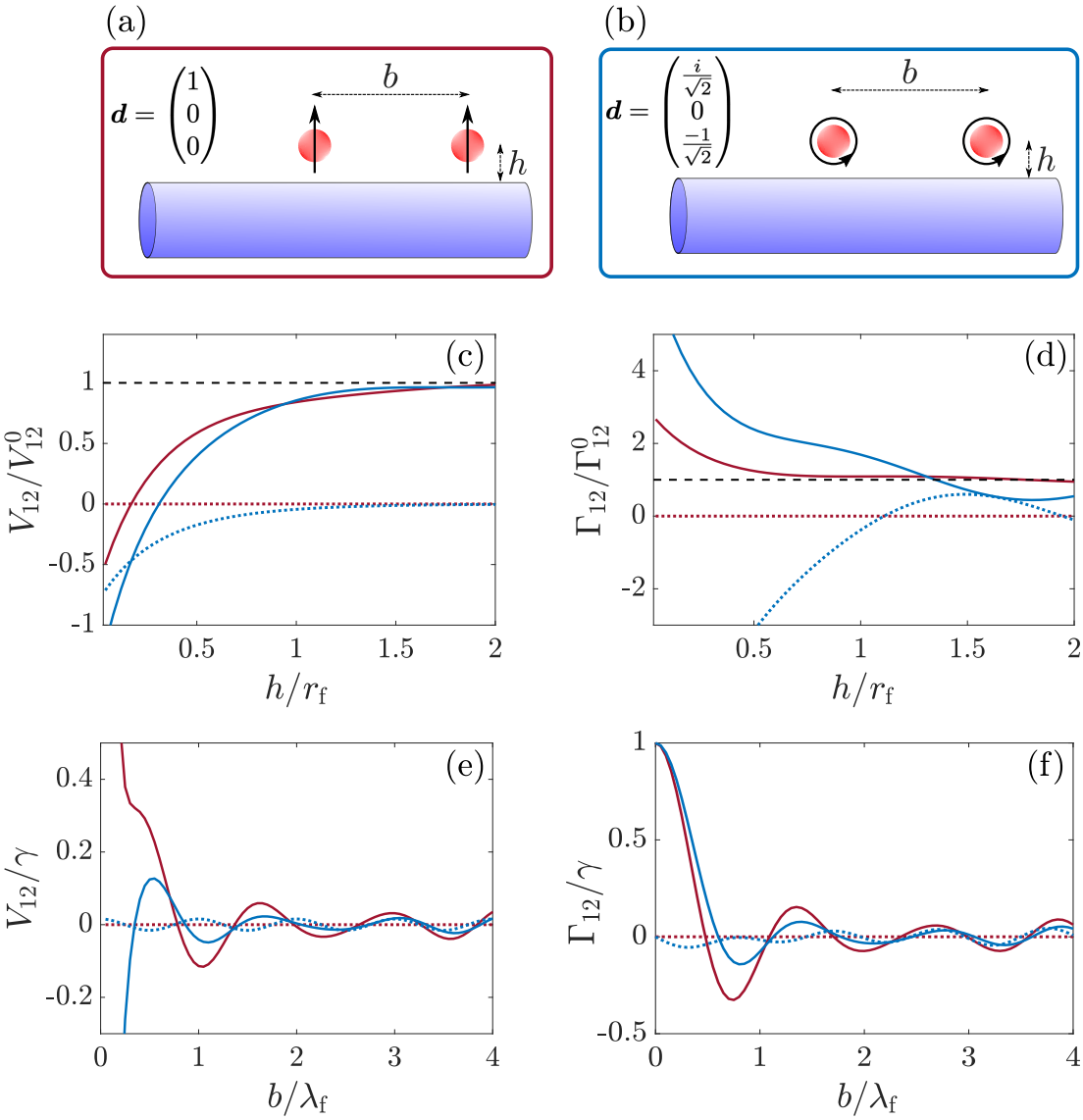

Figure 2.8: **Two Interacting Atoms**. **(a)** and **(b)**: Two-atom setups with linear and circularly polarised dipole moments respectively. The atoms are placed at a height h above the surface of the nanofiber and are separated by a distance b. **(c)** and **(d)**: Coherent and dissipative interactions respectively between the atoms as a function of their height above the fiber in units of the fiber radius. The atoms are separated by $b/\lambda_\mathrm{f} = 1.2$. The different colours match the differing dipole moments in (a) and (b) and the solid (dotted) lines are the real (imaginary) part of the interactions which are both scaled by the corresponding vacuum interactions. **(e)** and **(f)**: Coherent and dissipative interactions respectively between the atoms as a function of their separation distance in units of the wavelength of guided light when placed at a height of 90nm above the surface of the nanofiber. The colouring and line styles match that of (c) and (d). The interactions are scaled by the single-atom spontaneous decay rate in the same position above the fiber. In all plots we have used a fiber of radius 250nm and atoms with transition wavelengths $\lambda_a = 852.347$nm.

Now let us focus on how the separation (in the z-direction) between two atoms, which we call b, in the vicinity of the nanofiber affects the interactions between them. In Fig. 2.8(e) we find that as the separation between the atoms goes to zero, the coherent interactions diverge irrespective of their dipole orientations. This is no surprise as we approximated the unguided contribution to the interactions in terms of the free space coherent interactions which we have already stated diverge in this limit. When the atoms are well separated we find a large reduction in the strength of the coherent interactions, interestingly however they do not decay to zero. This is evidence of the long-range interacting capabilities of the atom-waveguide QED system. Next, in 2.8(f) we see that the dissipative interactions tend to the single-atom decay rate γ in the limit $b \to 0$ for both dipole orientations. As such, when the atoms are close together we expect the collective nature of the decay processes to be enhanced compared to when the atoms are well separated. In the case when the atoms become very well separated we see a large reduction of the strength of Γ_{12} however it too does not decay to zero. The fiber also induces long-range dissipative interactions between atoms.

2.3 Simulating Dynamics

As many in this field will have discovered, the Lindblad master equation (2.107) can rarely be easily (or at all) solved analytically. As a result one must turn to simulating the dynamics of quantum systems by numerical methods. This is a notoriously difficult thing to do on a classical computer however due to the exponential increase of the quantum system's Hilbert space with the number of emitters. The corresponding exponential increase in storage needed to simulate the system makes it impractical to consider systems with more than 6 atoms in our case. In this section we will briefly discuss the methods we used to truncate the Hilbert space, allowing us to investigate large system sizes and also how we turned Eq. (2.107) into a solveable matrix equation. We note that we drop the interaction subscript I, system superscript S and time argument from the derived density operator for ease of notation.

2.3.1 Choi-Jamiołkowski Isomorphism

Solving the dynamics described by the Lindblad master equation (2.107) analytically often becomes too difficult when there is more than one atom present in the system. Even if one can derive the system of differential equations constituted by the Lindblad master equation, they will often be equations for different coupled to one another in such a way as to make even numerical differential equation solving techniques impractical. It is often then useful to use the *Choi-Jamiołkowski isomorphism* [119, 120] (also known as *vectorisation*) which is defined by a map $V : \mathbb{C}^{n\times n} \to \mathbb{C}^{n^2}$, where $V\big(|e_i\rangle\langle e_j|\big) = |e_i\rangle \otimes |e_j\rangle$. Some useful properties of this mapping include

$$V(A+B) = V(A) + V(B), \tag{2.118a}$$
$$V(ABC) = (C^T \otimes A)V(B), \tag{2.118b}$$
$$tr\{A^\dagger B\} = V(A)^\dagger V(B), \tag{2.118c}$$

for arbitrary operators A, B and C. These properties allow us to write the Lindblad master equation (2.107) under this isomorphism as

$$V(\dot{\rho}(t)) = \mathbb{L}V(\rho(t)), \tag{2.119}$$

where the dynamics generated by the super-operator $\mathcal{L}$ are now represented by a matrix

$$\mathbb{L} = -i(\mathbb{1} \otimes H - H^T \otimes \mathbb{1}) + \sum_n \Gamma_n \left[(J_n^-)^* \otimes J_n^- - \frac{1}{2}\mathbb{1} \otimes J_n^+ J_n^- - \frac{1}{2}\left(J_n^+ J_n^-\right)^T \otimes \mathbb{1} \right]. \tag{2.120}$$

As a result we know the solution to the dynamics given by Eq. (2.119)

$$V(\rho(t)) = e^{\mathbb{L}t}\, V(\rho(0)). \tag{2.121}$$

Importantly, since V is an isomorphism it must have a unique inverse V^{-1} such that $V\left(V^{-1}\right) = V^{-1}\left(V\right) = \mathbb{1}$. This means that we can solve the dynamics of the system in the 'vectorised space' and then map back to the original space with the solution still intact. Furthermore we can find the evolution of operators in the vectorised space using Eq. (2.118c)

$$tr[A^\dagger \rho(t)] = V(A)^\dagger e^{\mathbb{L}t} V(\rho(0)). \tag{2.122}$$

If we then define $V(A(t))^\dagger = V(A)^\dagger e^{\mathbb{L}t}$ then this means $V(A(t)) = e^{\mathbb{L}^\dagger t} V(A)$. Thus we can in principle solve for the dynamics of all observables using this method.

A caveat with this method however is the size of the vectors and matrices in the vectorised space. For a density matrix $\rho(t)$ of dimensions $M \times M$, $V(\rho(t))$ will have dimensions $M^2 \times 1$ and $\mathbb{L}$ will have dimensions $M^2 \times M^2$. We could only use this method for a small number of atoms as a result.

Spectral Properties of $\mathbb{L}$

The Choi-Jamiołkowski isomorphism offers us more than just the ability to turn the Lindblad master equation into a matrix equation. We now examine the spectral properties of $\mathbb{L}$ and what they might tell us. Assuming $\mathbb{L}$ is diagonalisable it will have different right and left eigenvectors since in principle it is not Hermitian

$$\mathbb{L}\left|x_m\right\rangle = \lambda_m \left|x_m\right\rangle, \tag{2.123a}$$
$$\left\langle y_m\right| \mathbb{L} = \left\langle y_m\right| \lambda_m. \tag{2.123b}$$

Here λ_m is the m^{th} eigenvalue corresponding to the m^{th} right eigenvector $|x_m\rangle$ and the m^{th} left eigenvector $|y_m\rangle$. The spectral decomposition allows us to the write $\mathbb{L}$ as a diagonal matrix

$$\mathbb{L} = \sum_m \lambda_m \left|x_m\right\rangle \left\langle y_m\right|, \tag{2.124}$$

simplifying things greatly when writing down the required matrix exponential $e^{\mathbb{L}t} = \sum_m e^{\lambda_m t} \left|x_m\right\rangle \left\langle y_m\right|$. We can combine this result with the knowledge that

all density operators are trace preserving to find some necessary conditions on the right and left eigenvectors. First we note that using Eq. (2.118c), the trace preserving property of a density matrix $tr\{\rho(t)\} = 1$ is equivalently written in the vectorised notation as $V(\mathbb{1})^\dagger V(\rho(t)) = 1$. Using Eq. (2.119) this means that

$$\frac{d}{dt}V(\mathbb{1})^\dagger V(\rho(t)) = V(\mathbb{1})^\dagger \mathbb{L} V(\rho(t)) = 0. \tag{2.125}$$

Since this is true for all density operators $\rho(t)$, it is required that

$$V(\mathbb{1})^\dagger \mathbb{L} = 0, \tag{2.126}$$

which means the vectorised identity $V(\mathbb{1})$ must be a left eigenvector of $\mathbb{L}$ with eigenvalue 0, we will call them $|y_1\rangle$ and λ_1 respectively.

The right eigenvector corresponding to the zero eigenvalue, when written down as

$$\mathbb{L}\,|x_1\rangle = 0, \tag{2.127}$$

is clearly seen to be the stationary state of $V(\rho(t))$. Thus for all trace-preserving density operators, the corresponding vectorised evolution matrix $\mathbb{L}$ must have at least one zero eigenvalue with a left eigenvector corresponding to the vectorised identity matrix, and right eigenvector corresponding to the vectorised stationary state of the density operator $|x_1\rangle = V(\rho_{ss})$. We note that in principle the stationary state may not be unique, i.e. there exists more than one zero eigenvalue of $\mathbb{L}$, however in practice we do find a unique stationary state of the density operator.

2.3.2 Single-Excitation Regime

Systems with a master equation of the form Eq. (2.107) can be well approximated to be in the single-excitation regime when driven by a weak laser field [121]. In this regime the Hilbert space of M two-level atoms is spanned by the ground state $|G\rangle = |g_1\rangle \otimes |g_2\rangle \otimes \cdots \otimes |g_M\rangle$ and the excited states $|e\rangle_n = |g_1\rangle \otimes |g_2\rangle \otimes \cdots \otimes |e_n\rangle \otimes \cdots \otimes |g_M\rangle$.

In this truncated Hilbert space we find the following equations of motion for the components of the density operator

$$\langle G|\,\dot{\rho}\,|G\rangle = \sum_{ij} \Gamma_{ij}\rho_{e_i e_j}, \tag{2.128a}$$

$$\langle e_i|\,\dot{\rho}\,|e_j\rangle = -i\sum_{\beta}\left[\left(V_{i\beta} - \frac{i}{2}\Gamma_{i\beta}\right)\rho_{e_\beta e_j} - \left(V_{\beta j} + \frac{i}{2}\Gamma_{\beta j}\right)\rho_{e_j e_\beta}\right], \tag{2.128b}$$

where $\rho_{e_i e_j} = \langle e_i|\,\rho\,|e_j\rangle$. This allows us to write the equation of motion for the single-excitation subspace

$$\dot{\rho}_{ee} = -i[H_{\text{eff}}, \rho_{ee}], \tag{2.129}$$

where in this case $[H_{\text{eff}}, \rho_{ee}] = H_{\text{eff}}\rho_{ee} - \rho_{ee}H_{\text{eff}}^\dagger$. The trace of ρ_{ee} does not need to be one here, if it was then an excitation would never decay to the ground state. In this way the trace of ρ_{ee} tells us about the 'leakage' from the excited subspace to the ground state. We note here that H_{eff} is an $M \times M$ matrix with components $H_{\text{eff}}^{ij} = V_{ij} - \frac{i}{2}\Gamma_{ij}$ acting only on the single-excitation subspace. Any

state of the system in the single-excitation regime can be written as $|\phi(t)\rangle = c_G(t)\,|G\rangle + \sum_i c_e^i(t)\,|e\rangle_i$ with the coefficients $c_G(t)$, $c_e^i(t)$ encoding the information of where the population of a state lies at a given time. Naturally the normalisation of these states requires $\left|c_G(t)\right|^2 + \sum_i \left|c_e^i(t)\right|^2 = 1$ where i ranges from 1 to M.

We already know the solution for the dynamics of an equation of the form Eq. (2.129), i.e. $|\phi(t)\rangle = e^{-iH_{\text{eff}}t}\,|\phi(0)\rangle$. Under the weak laser-driving approximation we can solve for the stationary state of this truncated system, more precisely the stationary state values of the coefficients $c_e^i(t)$. This is done by solving [122]

$$\big(\Delta\mathbb{1} + H_{\text{eff}}\big)\boldsymbol{c}_{ss} = \boldsymbol{E}, \tag{2.130}$$

where Δ is the laser detuning, i.e. the difference between the atomic transition frequency and the laser frequency ($\Delta = \omega_0 - \omega_L$) and $\boldsymbol{c}_{ss}$ is the vector of $c_e^i(t)$ values in the stationary state. $\boldsymbol{E}$ is a vector of the electric field of the laser at each atom site with $\Omega e^{i\boldsymbol{k}_L\cdot\boldsymbol{r}_i}$ being the i^{th} component. Here $\boldsymbol{k}_L$ is the wavevector of the single-mode laser field, $\boldsymbol{r}_i$ is the position of the i^{th} atom and Ω is the Rabi frequency of the laser defined as $\Omega = \boldsymbol{d}\cdot\boldsymbol{E}_0$ where $\boldsymbol{E}_0$ is the amplitude of the electric field of the laser.

Chapter 3

Topology in Waveguide QED

3.1 Introduction

In this results chapter we will use a waveguide QED system in order to investigate the topological characteristics of the SSH model in both short and long-range interaction regimes. Without any research or experiment done in the area of long-range topology we hope that this research can open the door to a fuller understanding of topology in physics.

In Sec. 3.2 we provide a detailed illustration of the extended SSH model that will be used throughout the chapter. The precise coherent and dissipative coupling coefficients are then stated and the mathematical representation of the system particles is explained. We examine the role that TRS, PHS and chiral symmetry play in the topological characterisation of the extended SSH model and thoroughly examine the winding number for the system, outlining how we simplify its calculation and how we can analytically predict in which regimes it will change.

In Sec. 3.3 we demonstrate the precise SSH nature of the system when interactions are restricted to only nearest-neighbour atoms. We probe the topological phases of the system by varying controllable parameters of the model. We next examine in great detail the topological edge states which appear in the topological insulator phase of the model. We then test the topological protection of these edge states against atomic positional disorder.

Sec. 3.4 we begins the exploration of extending the number of interactions. We investigate how the introduction of next-nearest-neighbour interactions, that break the PHS and chiral symmetry of the system, affect the edge states found in the nearest-neighbour limit. We then test the robustness of these states again against local disorder.

In Sec. 3.5 we allow all interactions that do not break the chiral symmetry of the model to be present, allowing us to investigate how the bulk-boundary correspondence is altered for the long-range interacting SSH model. We search for signatures of topologically non-trivial eigenstates, testing any findings against varying levels of local disorder.

Next in Sec. 3.6 we re-introduce the interaction terms which break chiral symmetry such that we truly have a fully connected model. We follow the same prescription as in the previous sections to search for possible topologically non-trivial states of matter in this long-range interacting system.

In Sec. 3.7 we then turn our attention to the dynamical properties of the QED system. Opening the system to dissipation we investigate whether the candidates for long-range topological edge states can also be resistant to these dissipative effects. Furthermore we investigate the full range of decay profiles achievable by edge states in this long-range SSH model. We finish this chapter with a conclusion based on our results and a discussion on the possible future research paths one could take from these findings in Sec. 3.8.

3.2 Extended SSH Model in Waveguide QED

We now detail the atom-waveguide setup as seen in Fig. 3.1. All atoms are placed at the same radial distance from the centre of the nanofiber, at a height h above the fiber. They are arranged in a bipartite lattice structure with the atoms of one sublattice placed at the azimuthal angle ϕ_A, labelled sublattice A, and the atoms of the other sublattice placed at the azimuthal angle ϕ_B, labelled sublattice B. Without loss of generality we will always let $\phi_A = 0$. The unit cell of the lattice consists an atom from either sublattice [see Fig. 3.1(b)]. We will always use an even number of atoms M distributed into $M/2$ unit cells. The unit cells are separated by the lattice constant a and only atoms in the same unit cell are offset by a distance b along the z-axis (In Fig. 2.8 and Fig. 4.2 it was the distance between each consecutive atom). Finally, the nanofiber is chosen to be made of silica and all atoms are chosen to have dipole moments pointing in the radial direction. In polar coordinates

$$\boldsymbol{d} = \begin{pmatrix} d & 0 & 0 \end{pmatrix}, \tag{3.1}$$

where d is the magnitude of the dipole moment. We will see that this choice of the dipole moment guarantees real guided interactions such that $V_{ij}^g = V_{ji}^g$ which is a necessary condition of the SSH model.

This information allows us to further derive the guided components of the coherent and dissipative coefficients derived in general in Eq. (2.112) and Eq. (2.116) respectively

$$V_{ij}^g = \frac{\gamma}{2}\mathrm{sgn}(z_{ij})\sin(\beta_g z_{ij})\cos(\phi_{ij}), \tag{3.2a}$$

$$\Gamma_{ij}^g = \gamma\cos(\beta_g z_{ij})\cos(\phi_{ij}). \tag{3.2b}$$

Here we have defined

$$\gamma = \frac{2d^2\omega_0\beta_g'}{\epsilon_0}|e_r^g|^2 \tag{3.3}$$

as the single atom decay rate in the presence of the nanofiber, recall that e_r^g is the radial component of the electric field profile function of the guided modes of the nanofiber. We will only consider the effects of the guided modes in this chapter. This is a good approximation when the distances a and b are comparable to or larger than that of the transition wavelength associated to the $|g\rangle \to |e\rangle$ transition since both radiation coefficients decay as $(\frac{\lambda_a}{z})^3$ where $\lambda_a = \frac{2\pi c}{\omega_0}$ and z is the separation between the two atoms. We will look more into relaxing this approximation in the next chapter.

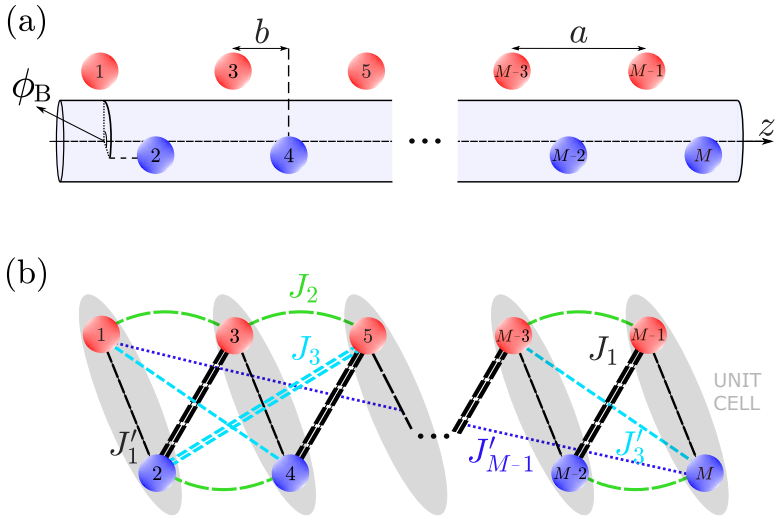

Figure 3.1: **Sublattice Atom-Waveguide QED**. (a) shows the atoms in sublattice A (red) and B (blue) with lattice constant a offset in the z-direction by a distance b, and offset by azimuthal angle ϕ_B. All atoms are at the same height $h = 190$nm above the fiber in the radial direction. (b) is a representation of the system once the fiber degrees of freedom have been traced out and a hopping model becomes evident.

Without the radiation modes, the Hamiltonian governing the coherent interactions between atoms takes the form

$$H = \sum_{ij} V_{ij}^{g} \sigma_i^{+} \sigma_j^{-}, \tag{3.4}$$

and the Γ_{ij}^{g} interactions alone describe the dissipative processes from the atoms. The coherent Hamiltonian in Eq. (3.4) contains all of the information on the geometry of the system parameters and thus it is all we need to look at when investigating the topological characteristics of the system. We will re-introduce the dissipative interactions later in this chapter when we consider the dynamical properties of the system. In order to classify the coherent Hamiltonian using the tenfold way classification, which is explicitly for fermionic particles, we must first make the following Jordan-Wigner transformation from the current spin representation [123]

$$\sigma_i^{+} = e^{-i\pi n_i} c_i^{\dagger}, \tag{3.5a}$$

$$\sigma_i^{-} = e^{i\pi n_i} c_i, \tag{3.5b}$$

where $c_i^{\dagger}, c_i$ are creation and annihilation operators satisfying the fermionic anti-commutation relations $\{c_i^{\dagger}, c_j\} = \delta_{ij}$, $\{c_i^{\dagger}, c_j^{\dagger}\} = \{c_i, c_j\} = 0$ and we have defined

$$n_i = \sum_{k}^{i-1} c_k^{\dagger} c_k. \tag{3.6}$$

Restricting our analysis to the single-excitation regime only, this transformation yields a quadratic Hamiltonian of spinless fermions

$$H = \sum_{ij} J_{|i-j|} c_i^{\dagger} c_j, \tag{3.7}$$

where we have let $J_{|i-j|} = V_{ij}^g$ as the sign of $z_i - z_j$ plays no part in V_{ij}^g. We can interpret $J_{|i-j|}$ as the hopping amplitude for one of these fermions to hop from site j to i.

It is useful to label the fermionic operators by the sublattice they create or annihilate a particle in. We let $c_{2p-1} = a_p$ and $c_{2p} = b_p$ to reflect the operators of sublattice A and B respectively. Here $p \in 1, 2, ..., M/2$ is the cell index. We also use the following labelling for the hopping amplitudes

$$J_{|i-j|} = \begin{cases} J_{2p} & |i-j| \text{ even} \\ J_{2p-1} & |i-j| \text{ odd; } i \text{ even} \\ J'_{2p-1} & |i-j| \text{ odd; } i \text{ odd} \end{cases}, \tag{3.8}$$

such that the same-sublattice hopping amplitudes are separated from the different inter-sublattice hopping amplitudes [see Fig. 3.1 (b)]. This labelling convention allows us to write the Hamiltonian as

$$\begin{aligned} H = \sum_{q=1}^{M/2} \sum_{p=1}^{M/2-q} \Big[& J_{2p-1} b_q^\dagger a_{q+p} + J'_{2p-1} a_q^\dagger b_{q+p-1} \\ & + J_{2p} \big(a_q^\dagger a_{p+q} + b_q^\dagger b_{p+q} \big) \Big] + J'_{M-1} a_1^\dagger b_{M/2} + \text{h.c.}, \end{aligned} \tag{3.9}$$

where we can also re-write the hopping coefficients in terms of the sublattice distance parameters and the guided mode parameters

$$J_{2p} = \frac{\gamma}{2} \sin(\beta_g a p), \tag{3.10a}$$

$$J'_{2p-1} = \frac{\gamma}{2} \sin\big[\beta_g((p-1)a + b)\big], \tag{3.10b}$$

$$J_{2p-1} = \frac{\gamma}{2} \sin\big[\beta_g(ap - b)\big]. \tag{3.10c}$$

We see that in this system the hopping rates are real and are restricted to the interval $[-\frac{\gamma}{2}, \frac{\gamma}{2}]$. The form of the hopping parameters (3.10a)-(3.10c) mean that the hopping interactions do not decay with the distance between sites. Instead they can facilitate all-to-all interactions in the system. When we only consider the J_1 and J'_1 hopping parameters the Hamiltonian (3.9) is exactly that of the well-known SSH model. In this way we have an 'extended' SSH Hamiltonian which is not limited to just nearest neighbour interactions, but instead includes all-to-all interactions.

The topological phases of the bulk of this model are examined in the thermodynamic limit. We can achieve this by setting periodic boundary conditions (PBC) on the lattice, which can be engineered in the atom-waveguide QED system as we will show later. Enforcing PBC on (3.9) makes it a real symmetric 2×2 block-circulant matrix which allows us to diagonalise it in the basis of Bloch states of the external degrees of freedom, i.e. cell index, such that

$$H_{\text{bulk}} = \sum_k \Psi_k^\dagger h(k) \Psi_k, \tag{3.11}$$

with $k \in \left[0, \frac{2\pi}{a}\right]$. Here, we have introduced the eigenvectors

$$\Psi_k = \begin{pmatrix} \tilde{a}_k \\ \tilde{b}_k \end{pmatrix} = \frac{1}{\sqrt{M/4}} \sum_{q=1}^{M/4} \mathrm{e}^{\mathrm{i}kqa} \begin{pmatrix} a_q \\ b_q \end{pmatrix}. \tag{3.12}$$

The 2×2 irreducible blocks $h(k)$ is known as the *reduced Hamiltonian*. It is convenient to write the reduced Hamiltonian as

$$h(k) = h_e(k) + h_o(k) \tag{3.13}$$

where we separate the intra-sublattice hoppings

$$h_e(k) = \begin{pmatrix} n_0(k) & 0 \\ 0 & n_0(k) \end{pmatrix} \tag{3.14}$$

with

$$n_0(k) = 2 \sum_{p=1}^{M/2} J_{2p} \cos kpa, \tag{3.15}$$

and the inter-sublattice hoppings,

$$h_o(k) = \begin{pmatrix} 0 & n(k) \\ n^*(k) & 0 \end{pmatrix} \tag{3.16}$$

with

$$n(k) = \sum_{p=1}^{M/2} \left[J_{2p-1} \mathrm{e}^{\mathrm{i}kpa} + J'_{2p-1} \mathrm{e}^{-\mathrm{i}k(p-1)a} \right]. \tag{3.17}$$

The two energy bands of the reduced Hamiltonian are then determined by $E^{\pm}(k) = n_0(k) \pm \left| n(k) \right|$.

As discussed in detail in Sec. 2.1.3, the topological nature of the bulk of the system is classified via the symmetries of the irreducible system Hamiltonian. TRS, PHS and chiral symmetry are determined in our case by the operators $T = \mathcal{K}$, $C = \sigma_z \mathcal{K}$ and $S = T \cdot C = \sigma_z$, respectively, where $\mathcal{K}$ is the conjugation operator and σ_z is the usual spin-1/2 Pauli-z matrix. In general, for real hopping coefficients, $h_o(k)$ exhibits time-reversal symmetry $T h_o(k) T^{-1} = h_o(-k)$, particle-hole symmetry $C h_o(k) C^{-1} = -h_o(-k)$ and chiral symmetry $S h_o(k) S^{-1} = -h_o(k)$. $h_e(k)$ possesses time-reversal symmetry but, most importantly, its presence makes the full Hamiltonian break PHS and chiral symmetry. This system is therefore to be attributed to the AI symmetry class, for which there is no topological invariant in one dimension. On the other hand, when $n_0(k) = 0$ (e.g., when the all even hoppings $J_{2p} = 0 \ \forall p$) the system is attributed to the BDI symmetry class, which has a $\mathbb{Z}$-type topological invariant in one dimension. In real space, the consequence of chiral symmetry is that if a pair of degenerate eigenstates have zero energy, each eigenstate can be rewritten such that they have support only on sublattice A and B, respectively. Conversely, if an eigenstate has support only on one sublattice, its energy must be zero [80]. The existence or absence of chiral symmetry will play a key part in our analysis in this chapter.

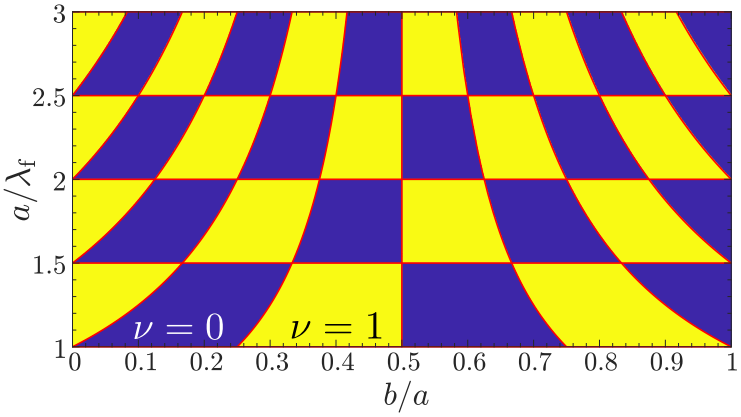

Figure 3.2: **Winding number.** The winding number ν, depicted here as a function of a/λ_f and b/a, takes only the values 0 and 1. The red solid lines represent the analytical predictions (3.22) and (3.21) for the phase boundaries.

As we showed in Sec 2.1.4, Hamiltonians of the form of the reduced Hamiltonian have a geometric phase which can be calculated via the winding number of $n(k)$. Using (2.32) we can write down the winding number of the bands

$$\nu = \frac{1}{2\pi}\Delta\theta(k), \tag{3.18}$$

where $\Delta\theta(k)$ is the variation of the argument of $n(k) = n_x(k) + in_y(k)$ through the FBZ where

$$n_x(k) = \sum_{p=1}^{M/2} \Big(J_{2p-1}\cos(kpa) + J'_{2p-1}\cos[k(p-1)a] \Big)$$
$$n_y(k) = \sum_{p=1}^{M/2} \Big(J_{2p-1}\sin(kpa) - J'_{2p-1}\sin[k(p-1)a] \Big).$$

The evaluation of the winding number can be performed numerically for very large system sizes, where we find that it only takes the values $\nu = 0$ and 1 [see Fig. 3.2]. By fixing the guided propagation constant β_g, we probe the topological phases of the system by varying the offset distance b between the sublattices at a range of values for the lattice constant a.

The values of b and a at which the system changes from a topologically trivial to non-trivial phase and vice versa can be obtained analytically by analyzing the symmetries of $n(k)$: as a consequence of time-reversal symmetry, $n_x(k)$ and $n_y(k)$ are symmetric and anti-symmetric, respectively, with respect to $k = \pi/a$. Hence, the closed path of $n(k)$ in complex space within the FBZ is symmetric about the real axis. In order to determine the winding number, we need to verify whether the closed path of $n(k)$ encloses the origin ($\nu = 1$) or not ($\nu = 0$). Since at the time reversal invariant momenta $k = 0$ and π/a, $n(k)$ crosses the real axis, i.e., $n_y(k) = 0$, it is enough to determine whether there is a change of sign in n_x at the two momenta. In particular, if $\mathrm{sgn}(\frac{n_x(\pi/a)}{n_x(0)}) = 1$, then $\nu = 0$, and if

$\mathrm{sgn}(\frac{n_x(\pi/a)}{n_x(0)}) = -1$, then $\nu = 1$. This can be summarised by

$$\nu = \frac{1}{2}\left[1 - \mathrm{sgn}\left(\frac{n_x(\pi/a)}{n_x(0)}\right)\right]. \tag{3.19}$$

We can determine the phase boundaries analytically using that

$$\mathrm{sgn}\left[\frac{n_x(\pi/a)}{n_x(0)}\right] = \mathrm{sgn}\left[\tan\left[\beta\left(b - \frac{a}{2}\right)\right]\tan\left[\frac{\beta a}{2}\right]\right]. \tag{3.20}$$

Here, one easily obtains that the winding number changes at the values

$$\frac{a}{\lambda_\mathrm{f}} = \frac{m}{2} \qquad \text{where } m \in \mathbb{Z}, \tag{3.21}$$

where $\lambda_\mathrm{f} = \frac{2\pi}{\beta_g}$ is the wavelength of the light propagating in the waveguide. Note, that due to the presence of all-to-all interactions, the gap between the two energy bands also closes whenever $a/\lambda_\mathrm{f} = n/M$ for any $n \in \mathbb{Z}$. However, only when condition (3.21) is satisfied is this gap closing accompanied by a change in the topological invariant of the system. Finally, fixing a, we also find a change from $\nu = 0$ to $\nu = 1$ and vice versa when

$$\frac{b}{\lambda_\mathrm{f}} = \frac{1}{2}\frac{a}{\lambda_\mathrm{f}} + \frac{n}{4}, \qquad \text{with } n \in \mathbb{Z}. \tag{3.22}$$

These phase boundaries correspond exactly with our numerical calculation of the winding number [see red lines in Fig. 3.2]. Note, that when only J_1 and J_1' are different from zero, we obtain exactly the winding number classification of the SSH model as expected, for which $\nu = 1$ when $|J_1| > |J_1'|$ while $\nu = 0$ when $|J_1| < |J_1'|$ [124]. Interestingly, we find that the winding number for our extended SSH model (Fig. 3.2) coincides with the one of the original SSH model, i.e., the topological invariant of the system bulk does not change as the connectivity of the problem is increased.

3.3 Nearest-Neighbour Interaction Limit

We now make clear the exact SSH nature of our model in the nearest-neighbour interaction limit. Setting $\phi_B = 0$, unless otherwise stated, we recover the expected bulk-boundary correspondence of the SSH chain with open boundary conditions (OBC) and give a detailed account of the resulting gapped, robust edge states.

In this limit we use a system of 100 atoms such that the translationally invariant bulk of the chain is very large in comparison to the edge of the chain and set $a/\lambda_\mathrm{f} = 1.0511$. We vary the sublattice offset distance b a total of one lattice constant a, i.e $b \in [0, a]$. Recall J_1 and J_1' vary according to (3.10c) and (3.10b) respectively.

The variation of the sublattice offset distance allows us to find two low-energy eigenstates in the regimes where $\nu = 1$, corresponding to the case when $|J_1| > |J_1'|$, and no low-energy eigenstates when $\nu = 0$, corresponding to the case when $|J_1| < |J_1'|$. This is the bulk-boundary correspondence of the SSH model and it is

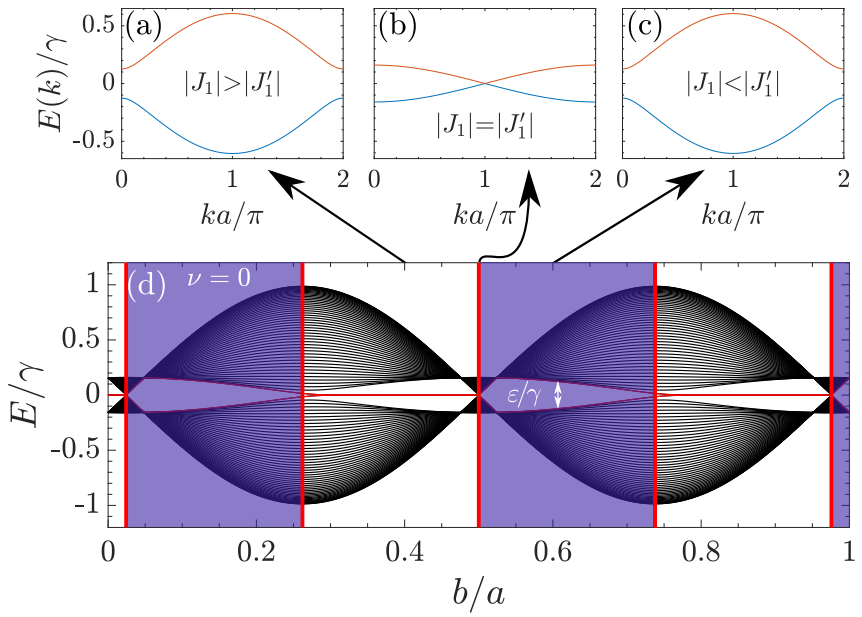

Figure 3.3: **SSH Topological Insulator. (a)-(c)**: Dispersion relation of the chain with periodic boundary conditions for $b/a = 0.4$, 0.5 and 0.6 respectively. **(d)**: Energy levels of the chain with open boundary conditions with the bulk topologically trivial ($\nu = 0$) and non-trivial ($\nu = 1$) regimes superimposed. Zero-energy eigenstates exist in the open boundary system when the bulk of the chain is in a topological insulator phase ($\nu = 1$).

more illustratively seen in Fig. 3.3(d). This figure also shows how the low-energy characteristics of the topological eigenstates in a chiral symmetric system can instead be characterised by their *mass gap* ε.

We show in Fig. 3.3(a)-(c) that the bulk is always in an insulating phase, which is guaranteed by the symmetric dispersion relation about zero, except for when $|J_1| = |J_1'|$ which is where the topological phase transitions. And so we distinguish that when $\nu = 1$ the bulk of the system is in a topological insulator phase whereas when $\nu = 0$ the bulk is in a regular insulating phase.

As mentioned in the introduction, topological insulators are known for their insulating bulk properties and conducting edge states. We have seen the insulating bulk properties so now we examine the edge states in more detail. These edge states are very often referred to as *zero-energy edge states* despite their energy often only being approximately zero. We will try to always refer to eigenstates with exactly zero energy as *exact zero-energy edge states* to distinguish.

The chiral symmetry present in the model allows eigenstates with zero energy to have support in only one sublattice. Conversely, eigenstates which can be written with support in only one sublattice must have zero energy. This can be seen clearly if we use exact diagonalisation of a general nearest-neighbour SSH Hamiltonian. Assuming the existence of a zero mass gap we find that the population of the pair of edge states must obey

$$|A_i|^2 = |A_1|^2 \, e^{\left(\frac{1-i}{\xi}\right)}, \tag{3.23}$$

$$|B_i|^2 = |B_1|^2 \, e^{\left(\frac{i-1}{\xi}\right)}, \tag{3.24}$$

where ξ is the *localisation length* of each sublattice

$$\xi = \frac{1}{2}\big(ln\big|J_1'\big| - ln|J_1|\,\big), \tag{3.25}$$

in units of the lattice constant a. Here we also see the exponential localisation of the exact zero-energy edge state population which is synonymous with these topologically non-trivial states of matter. So we could have the entire population of one zero energy edge state exponentially localised to the edge of sublattice A, and the entire population of the other zero energy edge state exponentially localised to the edge of sublattice B, or we could have a hybridised solution with edge states with population in both sublattices. When the mass gap is not exactly zero the edge states must hybridize as we will see.

In practice, we find that the energy eigenvalues of a system of M sites will be the roots of an equation of the form

$$\lambda^2 f(J_1', J_1, \lambda) + \frac{(J_1')^M}{(J_1)^{M-2}} = 0, \tag{3.26}$$

where $f(J_1', J_1, \lambda)$ is a real polynomial in powers of J_1', J_1 and λ. We thus find that a zero mass gap can only exist with an infinitely long chain and $|J_1'| < |J_1|$ (which is obviously impractical) or in the dimerized limit when $J_1' = 0$ and $J_1' \neq 0$. This becomes evident in Fig. 3.4 where we look in more detail at the edge states found in our model. Comparing the numerically fitted localisation length of the population profile of the system edge states with the localisation length of the population profile of the exact zero-energy edge states in Fig. 3.4(a), we see that 'deeper' into the topological phase, i.e. as $|J_1'|/|J_1|$ becomes smaller, the numerical and exact zero-energy edge state localisation lengths become smaller and get much closer together, indicating that the mass gap reduces 'deeper' into the topological phase which is exactly what we see in Fig. 3.3(d).

In Fig. 3.4(b) we see an example of an edge state population profile that is in the topological insulator phase but is still close to the topological transition point. In this case the hybridized edge state population does not match very well to the corresponding population of an exact zero-energy edge state, and the population is spread along the chain due to the relatively large localisation length. In Fig. 3.4(c) however we see that 'deeper' into the topological phase the edge state populations become much more localised to the edge of the chain due to their comparatively smaller localisation lengths, stemming from their eigenvalues being much closer to zero.

Eventually the localisation lengths do coincide at zero localisation length in Fig. 3.4(a) when $b \approx 0.476a$ at which point $J_1' = 0$, which is the topological dimerized limit with all atoms dimerized except for the first and last atom. Eigenstates localised entirely on these sites of the chain must have zero energy as there is no onsite potential in the system.

Next we test the robust nature of the topological edge states against disorder in the system. We introduce disorder as an uncertainty in the position of the atoms in the chain. We do this by letting the positions of the atoms z_i in the chain have a Gaussian distribution around their non-disordered positions $z_i^{(0)}$, i.e.

$$z_i \to z_i^{(0)} + \sigma R, \tag{3.27}$$

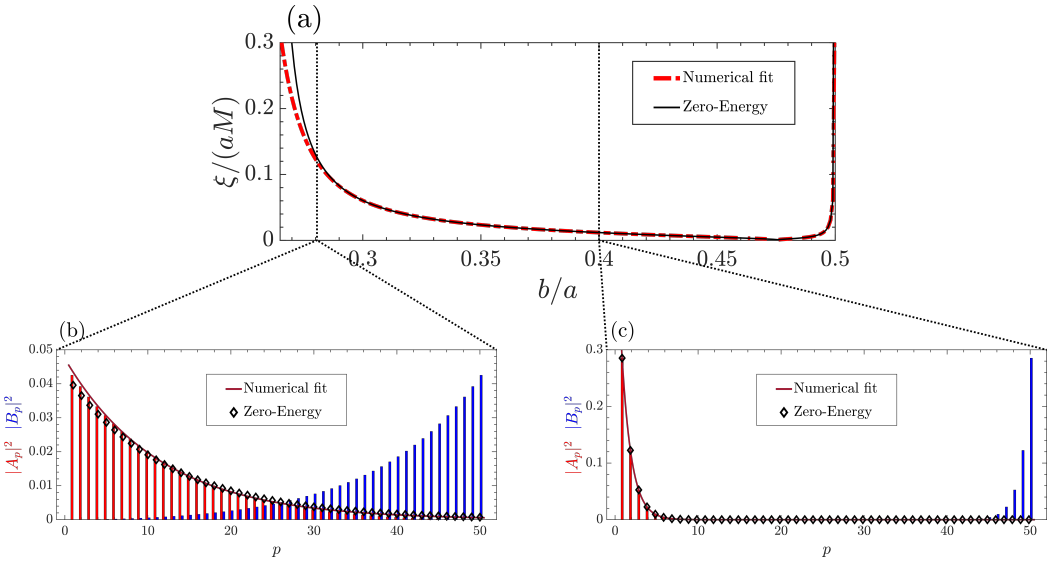

Figure 3.4: **Edge State Localisation. (a)**: Numerically calculated localisation length of the edge states assuming exponential profile (red dashed lines) and the localisation length of the exact zero-energy edge states (black line) as a function of the offset distance b/a. **(b)** and **(c)**: Edge state population profiles for regime where b/a is near a topological phase transition ($b/a = 0.281$) and a regime where b/a is deep into the topological phase ($b/a = 0.4$) respectively. In both cases the numerically fitted exponential profile of the edge population is shown (dark red line) along with the corresponding population profile of an exact zero-energy eigenstate (black diamonds).

where R is a number randomly generated form a normal distribution centred around zero and σ is the standard deviation of the normal distribution that is used to control the level of disorder applied. In order to examine the effects of this disorder we plot the mass gap of the system ε introduced previously, and the fidelity between disordered and non-disordered edge states, defined as

$$F_\sigma = \left|\langle \Psi_\sigma | \Psi_+ \rangle\right|^2, \tag{3.28}$$

as a function of the average hopping parameter fluctuation δJ resulting from the addition of disorder i.e. $J \to J + \delta J$. These simulations are averaged over 5000 samples of disorder. We compare results for the case when we are deep into the topological phase ($\varepsilon \approx 0$) and also for the case when ε is noticeably greater than zero. Fig. 3.5(a) shows that in the regime where $\varepsilon \approx 0$, corresponding to the edge states seen in Fig. 3.4(c), even for increases of up to 10% in the average fluctuations (note that the maximum value δJ could take is $\gamma/2$) the mass gap remains approximately zero. The inset shows that the bulk state energies have also remained well separated from the edge state energies even for large δJ so we expect there to be little change in the population profile of the edge state. This is indeed what we see in Fig. 3.5(b) where the fidelity remains very high despite the high levels of disorder. The inset shows a rather unchanged population profile for the edge state at a significant level of disorder.

As we expected, the edge states as seen in Fig. 3.4(b) do not exhibit the same level of robustness as the previous case. Fig. 3.5(c) shows an increase the mass

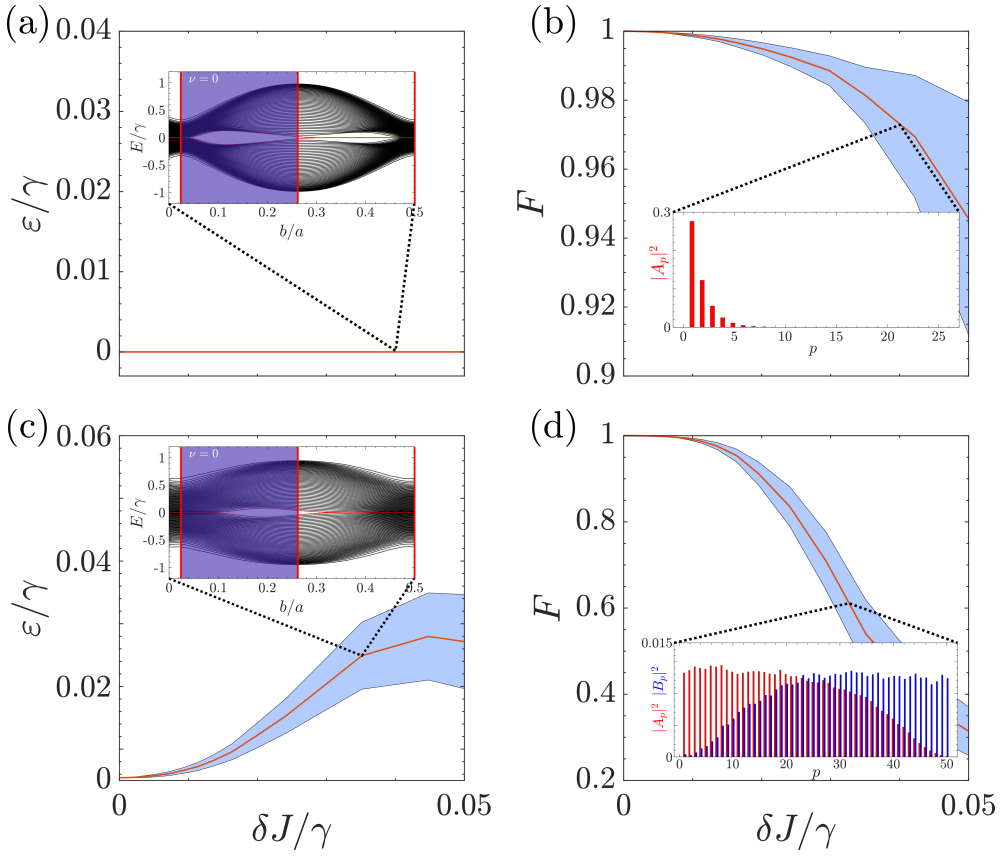

Figure 3.5: **Nearest Neighbour Robustness Against Disorder.** **(a)** and **(c)**: The mass gap ε of the chiral-symmetric system of $M = 100$ atoms as the average fluctuations of the hopping parameters are increased for $a/\lambda_f = 1.0511$ and $b/a = 0.4, 0.281$ respectively. **(b)** and **(d)**: Fidelity F of Eq. (3.28) of the in-gap eigenstates in the presence of disorder with respect to the corresponding state in the absence of disorder in the same parameter regimes as **(a)** and **(c)** respectively. In all figures, the red line represents the average value and the blue shaded area the standard deviation after 5000 realizations of disorder.

gap of the edge states as the level of disorder is increased. The inset shows the destructive effect the disorder has on the gapped nature of the edge state energies from the bulk energies in the topological phase. With this closing of the gap we would not expect the edge states to maintain their population profiles. This is precisely what we find in Fig. 3.5(d). The fidelity is significantly reduced such that very little of the unperturbed population profile is expected to remain. The inset confirms this as any semblance of the exponential localisation of the edge state population is lost, even at a lower level of average fluctuations than for the case in 3.5(c).

3.4 Next-Nearest-Neighbour Interactions

We now investigate what happens when we start to extend the range of atomic interactions to include next-nearest-neighbour (NNN) hoppings. As we have seen, NNN hopping means our bulk Hamiltonian now belongs to the AI symmetry class in which there is no topological invariant associated with 1D systems. We will

explore the destructive effect the NNN hoppings have on the topological insulator phases we found in Sec. 3.3.

To begin we note that the winding number calculation will not change as it does not depend on the same-sublattice hoppings, however we may not expect the same bulk-boundary correspondence due to the NNN interactions. This suggests that the destructive effects of the NNN hoppings are not in the underlying geometry of the bulk Hamiltonian but rather in the insulating properties of the bulk bands. Of course there is now no guarantee that the bulk bands will be symmetric around zero energy and so we define the following possible band gaps: A direct gap (DG) occurs when the minimum of the conduction band is larger than the maximum of the valence band, and they occur at the same value of k. An indirect gap (IG) also means the minimum of the conduction band is larger than the maximum of the valence band, but they occur at different values of k. No gap (NG) occurs when the minimum of the conduction band is smaller than the maximum of the valence band, in other words this is a metal [see Fig. 3.6(a)-(c) for examples of each band gap respectively]. These band gap phases are characterised by the system's hopping coefficients as follows

$$\begin{aligned} &\textbf{DG:} && J_2 < \tfrac{\left|J_1^-\right|-\left|J_1^+\right|}{4}, \\ &\textbf{IG:} && \tfrac{\left|J_1^-\right|-\left|J_1^+\right|}{4} < J_2 < \tfrac{\left|J_1^-\right|+\left|J_1^+\right|}{4}, \\ &\textbf{NG:} && \tfrac{\left|J_1^-\right|+\left|J_1^+\right|}{4} < J_2, \end{aligned} \tag{3.29}$$

where we have defined $J_1^{\pm} = J_1' \pm J_1$.

In Fig. 3.6(d) we plot these band gap phases as a function of the sublattice offset distance and superimpose the energy eigenvalues for the NNN interaction system. We use the same parameters as the NN limit, however this time due to the periodicity in the interactions we only plot the results in the range $b \in [0, \frac{a}{2}]$. From here on out we will only plot quantities that are a function of b in this range.

We find that the NNN interactions significantly reduce the gapped nature of the edge states found in the NN limit. As PHS and chiral symmetry are now broken, these states no longer need to have zero energy and become massive. We see that when J_2 is large enough to force the bulk into a metallic phase, all semblance of gapped energy eigenstates is lost even if the winding number is non-zero. This is not surprising since a topological insulator phase requires the bulk to exhibit both a topologically non-trivial phase and an insulating phase. These results agree with those obtained by Pérez-González et al. [82].

Now let us take a closer look at how the exponential profiles of the NN edge states have changed due to the NNN interactions when the bulk remains in an insulating phase. With chiral symmetry broken, we can not assume that the population of an edge state in each sublattice will be exponentially localised to different ends of the chain. We thus attribute a localisation length to both sublattices. We plot the numerically fitted localisation length of the population in sublattice A (red diamonds) and sublattice B (blue squares) along the first half

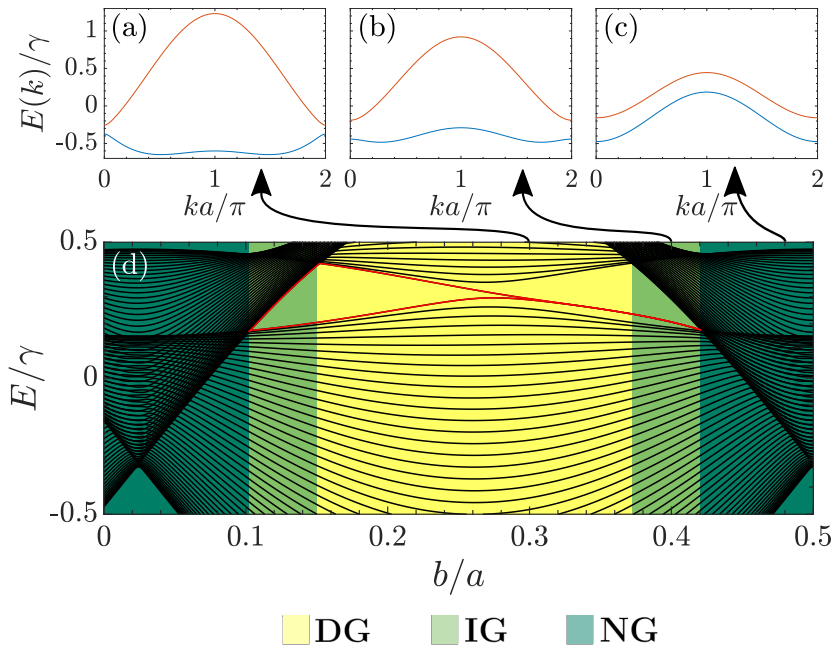

Figure 3.6: **NNN SSH Model Band Structures. (a)-(c)**: The PBC bulk bands corresponding to those in Fig. 3.3 (a)-(c) respectively now impacted by the addition of NNN interactions. **(d)**: The OBC energy level diagram corresponding to Fig. 3.3 **(d)** now only shown for half of the chain and with NNN interactions included, superimposed on top of the bulk band gap phase diagram. A smaller range of energy levels are shown in order to see the effects of NNN on the previously gapped zero-energy eigenstates.

of the chain (as we still expect there to be a symmetry about the midpoint of the lattice) in Fig. 3.7(a). We also plot the localisation lengths associated with the NN zero-energy analytical solutions and, as we did for the energy eigenvalue plot, these results are superimposed onto the band gap phase diagram. In Fig. 3.7(b) we plot the r^2 value associated to each of the exponential fits as a rudimentary method of checking whether the fits are of good quality. The r^2 value is defined as

$$r^2 = 1 - \frac{RSS}{TSS} \tag{3.30}$$

where RSS is the sum over all of the squared residuals of the fit, and TSS is the sum over all of the squared residuals if the fit was simply a line equal to the mean of all of the data. If $r^2 = 1$ this implies the fit perfectly accounts for all of the variance in the data, and if $r^2 = 0$ this implies the fit accounts for none of the variance in the data.

Interestingly we find a very similar behaviour in the localisation lengths despite the introduction of NNN hoppings in Fig.3.7(a). Far into the topological insulator phase the localisation lengths of the NNN eigenstate is almost exactly equal to that of the NN limit. The striking difference now is the divergence of the localisation lengths as the bulk approaches the metallic phase. Fig. 3.7(b) shows us that when the localisation lengths converge towards the NN zero-energy localisation lengths, the fits are in fact good quality fits. As one would expect, as the localisation lengths diverge approaching the metallic transition, the fits are found to be of very bad quality.

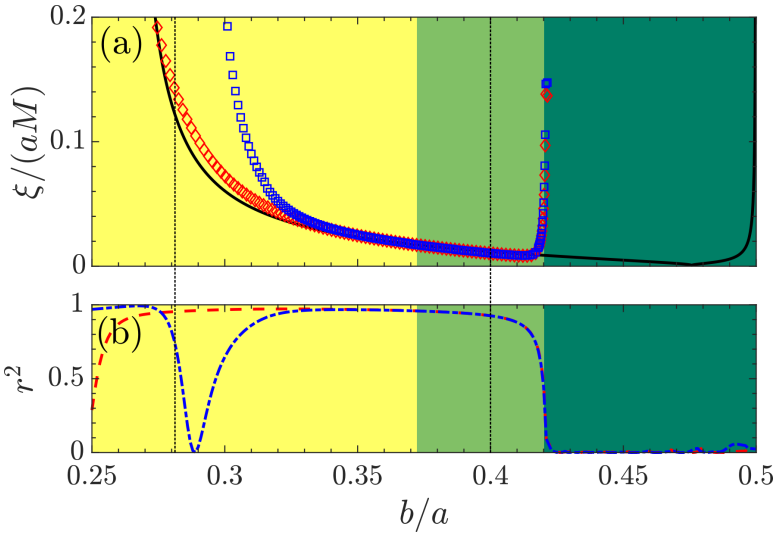

Figure 3.7: **Localisation Length Fits. (a)**: The localisation length of the assumed exponential profile of the eigenstate (those highlighted in red in Fig. 3.6(d)) sublattice population corresponding to the zero-energy eigenstates of the NN model. The analytical zero-energy state localisation length (black line) is compared to the localisation lengths of sublattice A (red diamonds) and sublattice B (blue squares) for the sublattice offset $b/a \in [0.25, 0.5]$. **(b)**: The r^2 value of the numerical exponential fits of sublattice A (red dash) and B (blue dash-dot).

Next we investigate these exponential fits of the edge states in more detail. We plot the NNN population of the states at each of the dashed lines found in Fig. 3.7(a) [see Fig. 3.8(a) and Fig. 3.8(b)]. These correspond to the states in 3.4(a) and Fig. 3.4(b) respectively. This time however we only plot the population of the first half of the chain due to the symmetry in the populations about the mid point of the lattice. If we were to rotate the chain by π and swap sublattice A with B we would have an identical chain, hence the symmetry in the eigenstate population. This symmetry is preserved irrespective of the TRS, PHS or chiral symmetry classification of the Hamiltonian.

The first thing we note from Fig. 3.8(a) and Fig. 3.8(b) is that the exponential fit is not as accurate as in the NN limit, even far into the topological insulator phase. Despite this we consider it to be accurate enough to inform us on the edge localisation of the eigenstate population. We find that adding NNN interactions for the case when $b/a = 0.281$ (Fig. 3.8(a)) increases the population in sublattice B on the left edge of the chain. There is also a reduction in the population in sublattice A on the left edge of the chain and a further mismatch with the analytically calculated zero-energy eigenstate. When $b/a = 0.4$ (Fig. 3.8(b)) we find that the edge state population remains highly localised to the edge of the chain not just for one sublattice, but for both. The localisation of both populations on the same side of the chain is a phenomena that is not seen in the NN limit an is solely due to the introduction of NNN interactions.

We have demonstrated that we can retain some semblance of the NN edge states by only weakly breaking the PHS and chiral symmetry of the original SSH model. So long as $J_2 < \frac{|J_1^-|+|J_1^+|}{4}$ [see Eq. (3.29)] we can still have insulating properties necessary for a topological insulating phase of matter.

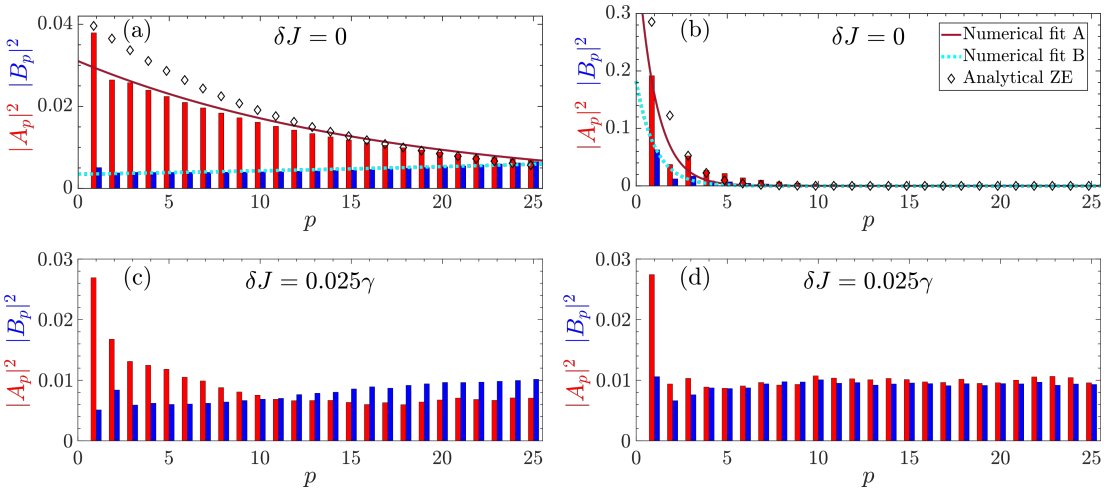

Figure 3.8: **NNN Edge States and Disorder.** **(a)** and **(b)**: The non-disordered population equivalent of the NN eigenstates of Fig. 3.4**(b)** and **(c)** with $b/a = 0.281$ and $b/a = 0.4$ respectively. Exponential numerical fits of sublattice A (dark red line) and B (dashed light-blue line) are included alongside the zero-energy analytical fit of the NN model (black diamonds). **(c)** and **d**: The same eigenstate populations seen in **(a)** and **(b)** respectively but with a significant level of disorder included such that $\delta J = 0.025\gamma$.

Despite this we do not expect the approximately exponentially localised edge states of the NNN hopping model to be as robust against disorder as the NN counterparts. This is because these states have energies that are not as well-separated (or gapped) from the energies of the bulk states. We confirm this by adding disorder in exactly the same way as we did in the NN case (see Eq. (3.27)). Fig. 3.8(c) and (d) show that even a moderate level of average fluctuations in the hopping parameters such as $\delta J = 0.025\gamma$ can almost completely destroy any approximately exponential edge localisation of the eigenstates regardless of how 'deep' into the topological phase we might get.

Already we can see the destructive effects of the PHS and chiral symmetry breaking interactions on the topological protection of the edge state population. In the discussion at the end of this chapter we outline a mechanism for 'switching off' these PHS and chiral symmetry breaking terms as a possibility for future research.

3.5 Long-Range Interactions Retaining Symmetries

As we have seen, the introduction of NNN interactions breaks the PHS and chiral symmetry of the SSH model and can destroy the topological insulating phases it exhibits. This is true for the inclusion of any of the J_{2p} hopping coefficients. Analogous to Sec. 3.3 we will begin our exploration of long-range interactions by first retaining the PHS and chiral symmetry of the Hamiltonian by manually

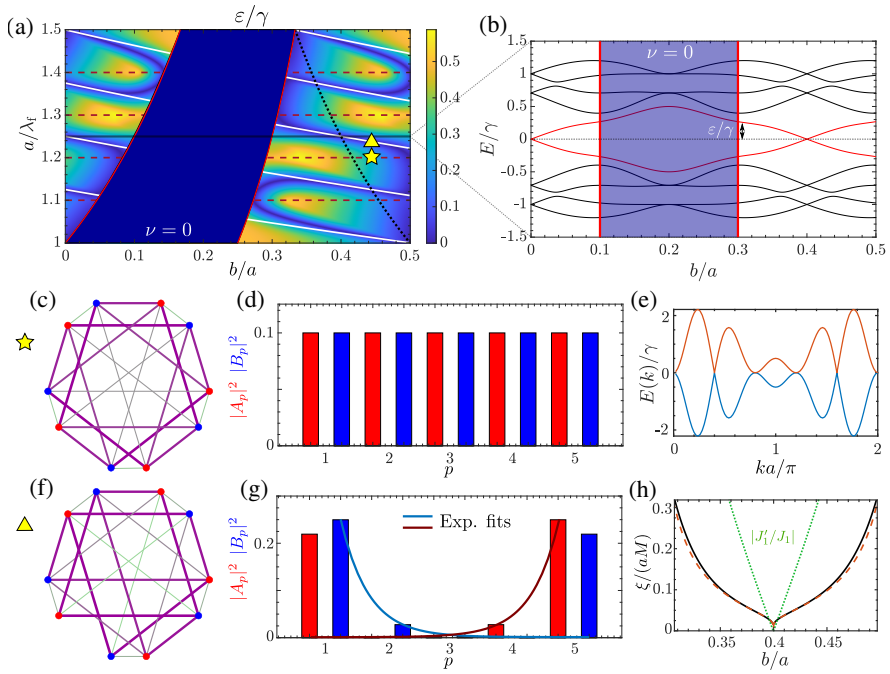

Figure 3.9: **Weakened Bulk-Boundary correspondence. (a)**: Mass gap ε for a system of $M = 10$ sites as a function of a/λ_f and b/a. The dark blue shaded area represents the region where $\nu = 0$. The horizontal dashed, solid white, and black dotted lines indicate where $|J'_{M-1}| = |J_1|$, $J'_{M-1} = 0$, and $J'_1 = 0$, respectively. **(b):** Spectrum at $a/\lambda_f = 1.25$ varying b/a. The mass gap is exactly zero at $b/a = 0.4$. **(c):** Sketch of the (chiral) system's couplings at $a/\lambda_f = 1.2$ and $b/a = 0.4444$ ($|J'_{M-1}| = |J_1|$). **(d):** The system is translationally symmetric, as reflected in the population of one of the eigenstates, and **(e):** the gap in k-space is closed. **(f):** Sketch of the (chiral) system's couplings at $a/\lambda_f = 1.2375$ and $b/a = 0.4444$ ($J'_{M-1} = 0$). **(g):** Near zero-energy states are exponentially localized to the edges of the system. **(h):** Localization length along one of the $J'_{M-1} = 0$ lines. The black solid line represents the length obtained from a fitting while the red dashed line is the analytical approximation given by (3.33). The green dotted line is the ratio $|J'_1/J_1|$.

setting all $J_{2p} = 0$. The Hamiltonian (3.9) in this case reduces to

$$H = \sum_{q=1}^{M/2} \sum_{p=1}^{M/2-q} \left[J_{2p-1} b_q^\dagger a_{q+p} + J'_{2p-1} a_q^\dagger b_{q+p-1} \right] + J'_{M-1} a_1^\dagger b_{M/2} + \text{h.c.} \tag{3.31}$$

The closer we get to the inclusion of all-to-all interactions, the more we lose the distinction between the bulk and boundary of the chain and thus the less we expect the bulk-boundary correspondence to hold. We find that for all-to-all interactions with all $J_{2p} = 0$ the bulk-boundary correspondence is not completely lost but is only weakened. We identify two parameter regimes that give rise to eigenstates that are of interest to us, namely *flat states* and *localised states*.

3.5.1 Flat States

In this case, we find a parameter regime where the first particle can hop to its nearest neighbor and to the last site of the chain with the same hopping rate i.e.

$|J'_{M-1}| = |J_1|$. Moreover, the specific form of the rates (3.10b-3.10c), imposing that $|J'_{M-1}| = |J_1|$ automatically implies that $|J'_{M-2p+1}| = |J_{2p-1}|$ for all p [see Fig. 3.9(c)]. Here, not only the bulk but also the finite open system are translationally symmetric. Since all cells are equivalent, the concept of boundary becomes ill-defined. As a consequence, as one can observe in Fig. 3.9(d), all eigenstates of the Hamiltonian are such that all sites are uniformly occupied, reflecting the translational symmetry. Note, that the condition $|J'_{M-1}| = |J_1|$ is satisfied when $a/\lambda_{\rm f} = m/M$ with $m \in \mathbb{N}$. So when M increases, there are more values of $a/\lambda_{\rm f}$ within a given interval that constitute these flat states. In the limit of $M \to \infty$ every value of $a/\lambda_{\rm f}$ would exhibit flat states at all values of b. It is for this reason we have carried out the fully connected analysis with a chain of $M = 10$ atoms.

We point out that the bulk gap in momentum space closes [see Fig. 3.9(e)] when we impose the condition $|J'_{M-1}| = |J_1|$ as this is a topological transition point. Hence, even though this gap closing does not come accompanied by a change in the topological invariant, specifically in this parameter regime [horizontal dashed lines in Fig. 3.9(a)] the winding number is not well defined and hence the flat states are not topologically protected states.

3.5.2 Localised States

The translational symmetry is broken whenever $|J'_{M-1}| \neq |J_1|$, as one can again distinguish the boundaries from the bulk. The extreme case here occurs when $J'_{M-1} = 0$, i.e., when the first and the last atom in the chain are not coupled to each other [see Fig. 3.9(f)]. This occurs whenever the parameters satisfy

$$\frac{b}{\lambda_{\rm f}} = \frac{M-2}{2}\frac{a}{\lambda_{\rm f}} + \frac{m}{2} \quad m \in \mathbb{N}. \tag{3.32}$$

In the topologically non-trivial region and along this line in parameter space [solid white lines in Fig. 3.9(a)], one finds two approximately zero energy [mass gap $\varepsilon \approx 0$] eigenstates.

While usual topologically protected edge states are exponentially localized on one of the two boundaries, we find here that the population is concentrated on both boundaries of the chain [cf. Fig. 3.9(g)], such that the occupation probability of the sites in the p-th cell in sublattice A and B, respectively, can be written as

$$\begin{aligned} |A_{M/2-p+1}|^2 &= |A_{M/2}|^2 e^{-\frac{pa}{\xi}}, \\ |B_p|^2 &= |B_1|^2 e^{-\frac{pa}{\xi}}, \end{aligned}$$

for $p = 2, \ldots, M/2-1$, and $|A_1|^2 = |B_{M/2}|^2$. Where ξ, as in Sec. 3.3, is the localization length of the edge state for each sublattice. As we can observe in Fig. 3.9(h), the localization length is smaller (i.e. edge states more localized in the edges of the lattice) the smaller the ratio J'_1/J_1. One can obtain that the localization length is approximately given by

$$\xi \approx -\frac{a}{\log\left|\frac{J'_1}{J'_3}\right|}. \tag{3.33}$$

As one can see in Fig. 3.9(h), this simple expression yields indeed an excellent approximation to the localization length, particularly for small values of the ratio $|J_1'/J_1|$.

The edge states become completely localized on the edges when $J_1' = 0$. It can be easily shown that this occurs when

$$\frac{a}{\lambda_{\rm f}} = \frac{m}{M-2}, \quad \frac{b}{\lambda_{\rm f}} = \frac{m'}{2}, \tag{3.34}$$

with m and m' being natural numbers. Here, the edge states can be analytically obtained, and they read

$$|\Psi_{\pm}\rangle = \frac{1}{2}\left[a_1^\dagger \pm b_1^\dagger + (-1)^n\left(a_{M/2}^\dagger \pm b_{M/2}^\dagger\right)\right]|0\rangle\,, \tag{3.35}$$

with $n = \lfloor M/4 \rfloor$, and $|0\rangle$ being the state with no fermions. Note, moreover, that at this point these edge states have exact zero energy, and that the spectrum becomes doubly degenerate [see Fig. 3.9(b)]. This structure is reminiscent of what occurs in the presence of a so-called strong zero mode [125–131]. Indeed, here there exists an operator $\Psi = \sum_p i(-1)^p\left(a_p^\dagger b_p - b_p^\dagger a_p\right)$ that anticommutes with a symmetry of the Hamiltonian $\mathcal{D} = \sum_p\left(a_p^\dagger b_p + b_p^\dagger a_p\right)$. Due to the long-range character of the hopping rates, though, in our case the strong zero mode Ψ is not concentrated on the edges of the lattice, as it is usually the case considering systems with short range interactions. Moreover, the Hamiltonian exactly commutes with Ψ for all system sizes (cf. [131]), instead of doing so only in the thermodynamic limit.

3.5.3 Robustness of Localised States

We now test the robustness of these localised states by adding disorder in the form of uncertainty in each of the atomic positions [see Eq. (3.27)], as was done in Sec. 3.3 and Sec. 3.4.

For each realization of disorder, we calculate the mass gap ε_σ of the edge state $|\Psi_\sigma\rangle$, and the fidelity [see Eq. (3.28)] between the measured edge state and the state with zero disorder. After many realizations, we extract the corresponding average fluctuations of the hoppings, $J \to J+\delta J$, and the average mass gap ε and fidelity F, shown in Fig. 3.10 (a) and (b), respectively, for the fully localized case, where both J_1' and J_{M-1}' are equal to zero [where in the absence of disorder $\varepsilon = 0$ and the edge states are exactly given by (3.35)]. As one can observe, as we increase the average fluctuations up to more than 10% (note that the maximum value δJ could take is $\gamma/2$) the mass gap increases linearly with the disorder, remaining much smaller than the gap between the bulk bands in all cases. Moreover, the fidelity of the edge state with respect to the no-disorder case remains above 0.99. In Fig. 3.10 (c) and (d) we show the same results for a parameter regime where $J_{M-1}' = 0$ but $J_1' \neq 0$ [cf. Fig. 3.9(f-g)]. One can easily observe that the deviation of the mass gap and fidelity from their no-disorder values remain small. Finally, let us point out that the size of the system, M, does not affect the results. Hence, we have established that the edge states along the full line $J_{M-1}' = 0$ are indeed extremely robust against external disorder.

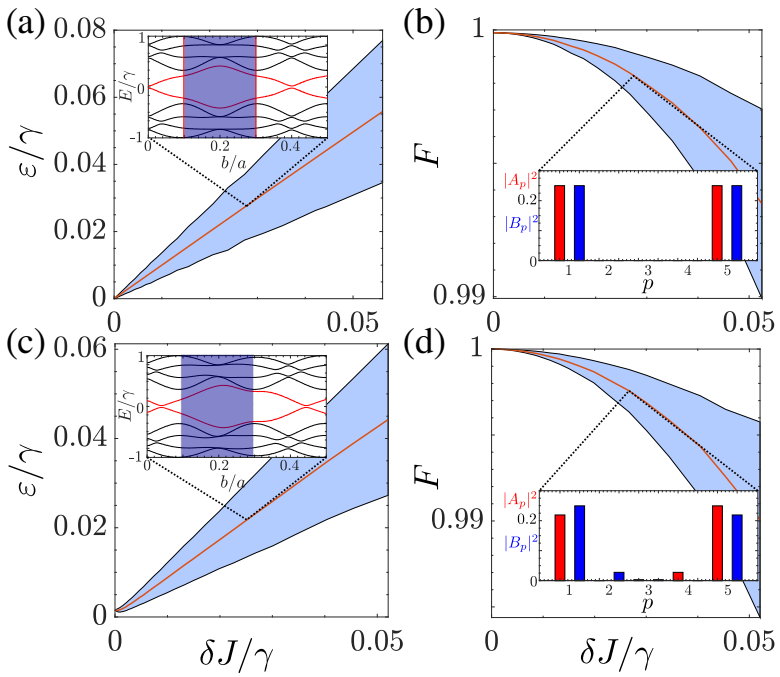

Figure 3.10: **Robustness against local disorder.** **(a)** and **(c):** Mass gap ε for a system of $M = 10$ sites as a function of the average fluctuations of the coupling constants δJ. **(b)** and **(d):** Fidelity F of the edge state in the presence of disorder with respect to the corresponding state in the absence of disorder. In all figures, the red line represents the average value and the blue shaded area the standard deviation after 5000 realizations of disorder. The parameters are $a/\lambda_f = 1.25$ and $b/a = 0.4$ for **(a)** and **(b)** and $a/\lambda_f = 1.2375$ and $b/a = 0.4444$ for **(c)** and **(d)**.

3.6 Long-Range Interactions Breaking Symmetries

Up until now we have studied a system where the chiral symmetry is not broken, i.e., where the intra-sublattice hoppings J_{2p} have been put to zero. In a real atom-waveguide system, these cannot be generally put to zero unless $a/\lambda_f = m/2$ [see Eq. (3.10a)]. Unfortunately, this regime is also precisely where the bulk gap closes (horizontal lines in Fig. 3.2), and hence no topological invariant can be defined. In this section, we will explore a situation where, even though the chiral symmetry is not strictly conserved, states with energy close to zero appear in the gap between the bulk bands which, moreover, are localized to the edges of the chain and are robust to local disorder.

We focus on the situation where the number of atoms is even but not a multiple of four, i.e. $M = 4n + 2$ for $n \in \mathbb{N}$. Here, when $a/\lambda_f = m/(M-2)$ one can make half of the even couplings zero, such that

$$J_{2p} = \begin{cases} 0 & \text{if} \quad p \,\text{even} \\ \frac{\gamma}{2}(-1)^{\frac{p-1}{2}} & \text{if} \quad p \,\text{odd}. \end{cases} \tag{3.36}$$

Moreover, as it can be observed in Fig. 3.11(a), the spectrum becomes symmetric around $E = 0$ at the point determined by condition (3.34). Here, the eigenstates

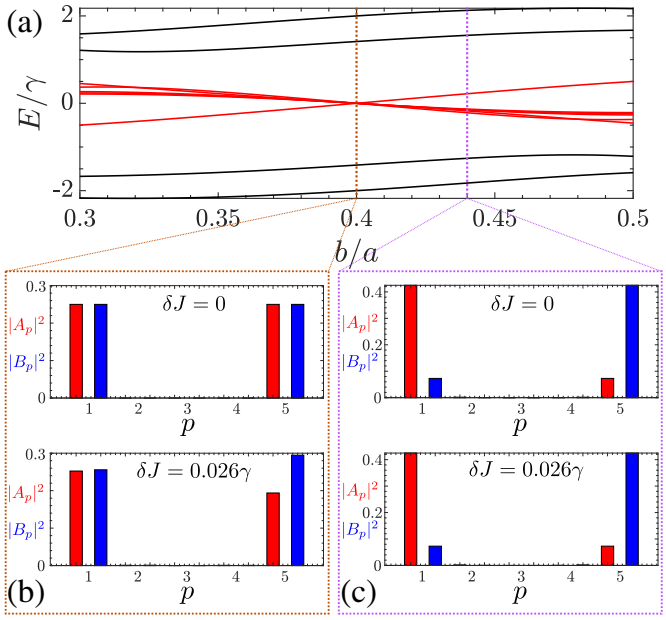

Figure 3.11: **Non-chiral edge states. (a):** Spectrum for a system of $M = 10$ atoms with $a/\lambda_f = 1.25$. **(b):** At $b/a = 0.4$, the spectrum is symmetric around $E = 0$ and some of the zero-energy eigenstates are strongly localized to the edges. **(c):** At $b/a = 0.44$ the degeneracy is lifted, but the edge states are still present. The lower panels in **(b)** and **(c)** represent the edge state in the presence of disorder, averaged over 5000 realizations.

of the Hamiltonian can be obtained analytically. In particular, we find that there is a manifold of $M/2+1$ eigenstates with zero energy. Some of these eigenstates are indeed localized in the edge, such as

$$|S_\pm\rangle = \frac{1}{2}\left[a_1^\dagger + b_1^\dagger \pm \left(a_{M/2}^\dagger + b_{M/2}^\dagger\right)\right]|0\rangle \tag{3.37}$$

$$|A\rangle = \frac{1}{2}\left[a_1^\dagger - b_1^\dagger + (-1)^n\left(a_{M/2}^\dagger - b_{M/2}^\dagger\right)\right]|0\rangle\,. \tag{3.38}$$

These states are, moreover, robust in the presence of local disorder, in the sense that they stay localized to the edges, not spreading into the bulk [Fig. 3.11(b)]. However, note that the mixing with the rest of eigenstates of the quasi-degenerate manifold lead to small variations in the populations of the edge sites involved.

To avoid this mixing, one may move away from this particular symmetric point. As we can observe in Fig. 3.11(a), both to the right and left of this point (larger and smaller b/a, respectively), the zero-energy degeneracy is indeed lifted. However, the eigenstates with energies now slightly different from zero are still localized on the edges and extremely robust to the addition of local disorder [see, e.g. Fig. 3.11(c)]. Moreover, again the structure of the spectrum and the eigenstates, including the existence of robust edge states, are independent of the number of atoms in the system, M. Note, however, that strictly speaking we have no reason to believe these localized states are topologically protected states, as the chiral symmetry is here broken and hence there is no topological invariant associated with the corresponding Hamiltonian.

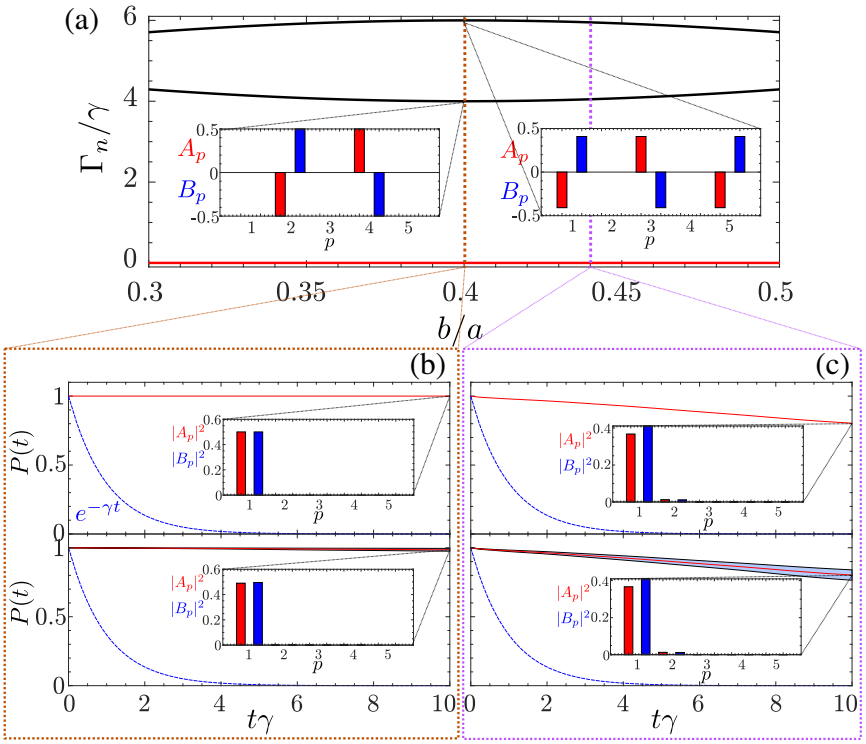

Figure 3.12: **Non-equilibrium dynamics. (a):** Collective decay rates for a system of $M = 10$ atoms with $a/\lambda_f = 1.25$. The insets show the probability amplitudes of the two superradiant states for $b/a = 0.4$. **(b)** and **(c):** Survival probability $P(t)$ of a single excitation as a function of the reduced time $\tau\gamma$, with the initial state being given by $|\Phi(0)\rangle$ (see main text) for $b/a = 0.4$ and 0.44, respectively. The lower panels show the same quantities in the presence of disorder, at $\delta J = 0.05\gamma$, for 5000 realizations. Each inset shows the occupation probability at the final time $t = 10\gamma$. For comparison, the decay of a single atom excited next to the waveguide is depicted in all panels.

3.7 Non-Equilibrium Dynamics

Up until now, we have studied only the static properties of the atom-waveguide system in the absence of dissipation. While this has offered us the possibility to study the topological properties of the system and demonstrate the existence of edge states, one can see from the expressions of the coherent and dissipative coupling V_{ij}^g and Γ_{ij}^g, in Eqs. (3.2a) and (3.2b), respectively, that the two mechanisms are inevitably intertwined, i.e., the dissipation in general cannot be neglected. In this Section, we study the out-of-equilibrium subradiant dynamics of the system in the presence of dissipation via the effective Hamiltonian, H_{eff}, approach defined in Eq. (2.129) but only using the guided interactions, focusing in particular on the lifetime of the edge states found in the previous sections.

3.7.1 Subradiance

Since the dissipation coefficients $\Gamma_{ij}^g = \gamma\cos(\beta z_{ij})$ do not decay with the distance between the atoms, the dissipation in this system has a collective character. We establish this by calculating the dissipation channels $|\psi_n\rangle$ and corresponding

decay rates Γ_n in the single-particle sector as the eigenstates and eigenvalues of the matrix Γ^g_{ij}, respectively. Independently of the parameter regime, there are only two superradiant modes with decay rates $\Gamma_{1,2}$ much larger than γ. The rest of the states forms a subradiant manifold with zero decay rate [121], as one can observe in Fig. 3.12(a) for $a/\lambda_{\rm f} = 1.25$. Along this line in parameter space, one can see that one of these two eigenstates has no support on the lattice edges, while the other one does. However, the latter has an alternating phase profile, similarly to the state $|A\rangle$ given in Eq. (3.38). Any initial state that one chooses to excite in this system that does not have a large overlap with these two superradiant states will be, thus, subradiant.

If, moreover, we are in a parameter regime where an edge state has been predicted to exist in the previous Section, we expect an initial state with large support on the edge to remain localized in the edge during the dynamics determined by (2.107). This is indeed what we observe in the upper panels of Figs. 3.12(b) and (c) by measuring the survival probability, $P(t) = \sum_{p=1}^{M/2} \left(|A_p(t)|^2 + |B_p(t)|^2\right)$ for two values of the parameter b/a: the initial symmetric superposition localized state,

$$\big|\Phi(t=0)\big\rangle = \frac{1}{\sqrt{2}}\left(a_1^\dagger + b_1^\dagger\right)|0\rangle \tag{3.39}$$

(i.e., $A_1 = B_1 = 1/\sqrt{2}$, $A_p = B_p = 0$ for all $p = 2, \dots M/2$) remains localized, and the excitation has an extremely long lifetime. In particular, for $b/a = 0.4$ the initial state is an eigenstate of both the coherent interactions (i.e. a zero-energy edge state), and of the dissipation (belonging to the subradiant manifold). Hence, as expected, the state remains completely unchanged throughout the dynamics. In the lower panels of Figs. 3.12(b) and (c) we show how this dynamics is also extremely robust against local disorder.

3.7.2 Excitation Transport

We have seen that in the case when chiral symmetry is broken we can find eigenstates localised on one side of the chain that remain as such for long times even in the presence of the dissipative dynamics. We now present the results of the same out-of-equilibrium dynamical investigation but in the case where each J_{2p} remains zero. Letting $a/\lambda_{\rm f} = 1.25$ and $b/a = 0.4$ again we take the initial state (3.39) localised on one end of the chain and see how it evolves. Fig 3.13 (a) shows us that once again the total population of the excited state does not decay for very long times but Fig 3.13 (b) shows us that the initial excitation is not static, as the excitation was when we broke chiral symmetry. In fact we find that the excitation population is completely transferred from one end of the chain to the other periodically and seemingly without propagating through the middle of the chain. These results are very similar to those obtained in [59].

3.7.3 Beyond Subradiance

We now turn our attention to engineering the waveguide QED system in order to change the dynamical decay properties of the edge state. We will use the setup $a/\lambda_{\rm f} = 1.25$ and $b/a = 0.4$ with the initial excitation again being $|\Phi(t)\rangle$ from (3.39). We no longer restrict the azimuthal angle ϕ_B between sublattice A

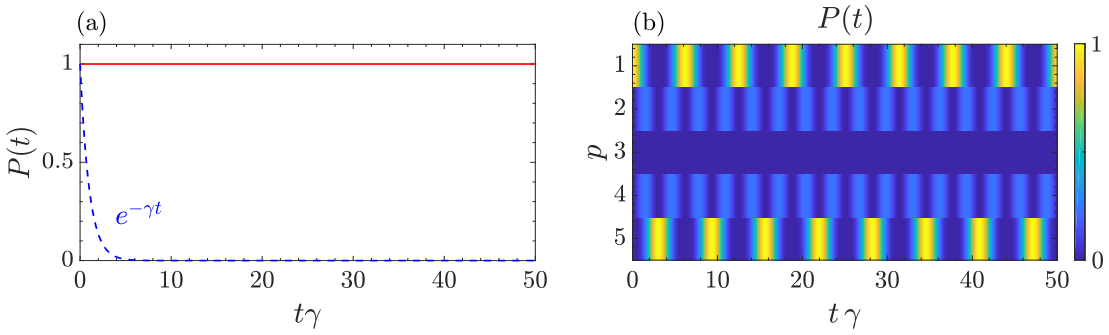

Figure 3.13: **Excitation Population Transfer. (a)**: Dynamic (non-)decay of overall population of initial state $\left|\Phi(0)\right\rangle$ (red line) for $b/a = 0.4$ compared to the dynamic population decay of a single atom in the vicinity of the nanofiber (blue dashed). **(b)**: A heat-map of the population contained in each unit cell (indexed by p) as $\left|\Phi(0)\right\rangle$ evolves.

and sublattice B to zero and show that varying this angle can lead to different decay properties than the case of $\phi_B = 0$. To aid our analysis we introduce the normalised *instantaneous decay rate* of the state in question

$$\Gamma(t) = \frac{\sum_i^M \Gamma_i \left|\langle\Phi(t)|\psi_i\rangle\right|^2}{\sum_i^M \left|\langle\Phi(t)|\psi_i\rangle\right|^2}, \tag{3.40}$$

where the $|\psi_i\rangle$ are the eigenstates of the decay matrix.

Firstly we note that in Fig. 3.14(c) and (d) when $\phi_B = 0$ we simply recover the results of Fig. 3.12(a) and (b), namely the two highly superradiant decay modes have zero overlap with the excitation $|\Phi(t)\rangle$ and so it does not decay in time. Fig. 3.14(e) reassures this result showing $|\Phi(t)\rangle$ has a zero effective decay rate for very long times.

As we increase ϕ_B, Fig. 3.14(d) shows that two of the previously zero-decay modes lift from the degenerate manifold. This coincides with a decrease of the population of $|\Phi(t)\rangle$ over time, as seen in Fig. 3.14(c). As ϕ_B increases to π we see that the population of $|\Phi(t)\rangle$ decays more rapidly. When $\phi_B = \pi$ we find that the decay of the excited state population is, at early times, faster than that of the single-atom excitation population decay. We note that when $\phi_B = \pi/2$ the sublattices are completely decoupled and act as independent and identical chains. As a result there is at least a two-fold degeneracy in each of the energy levels.

The effective decay rates in Fig. 3.14(e) show us that $|\Phi(0)\rangle$ has a higher overlap with the superradiant decay modes the closer ϕ_B gets to π. This is because when atoms are separated by an azimuthal angle of π, then it is the anti-symmetric superposition state which becomes subradiant, and the symmetric superposition state becomes highly superradiant as seen in Fig. 3.14(a) and (b). As time increases the effective decay rates always become subradiant which is evident in the slowing down of the dynamical decay of the population in Fig. 3.14(c). $P(t)$ only slowly approaches zero for each value of ϕ_B.

As ϕ_B increases we also find more fluctuations in the effective decay rate of $|\Phi(t)\rangle$. The change between decreasing and increasing decay rates, which are most pronounced for $\phi_B = \pi$, explain the fluctuating rates of population decay $P(t)$. On the other hand, say for $\phi_B = \pi/8$ the effective decay rate is almost

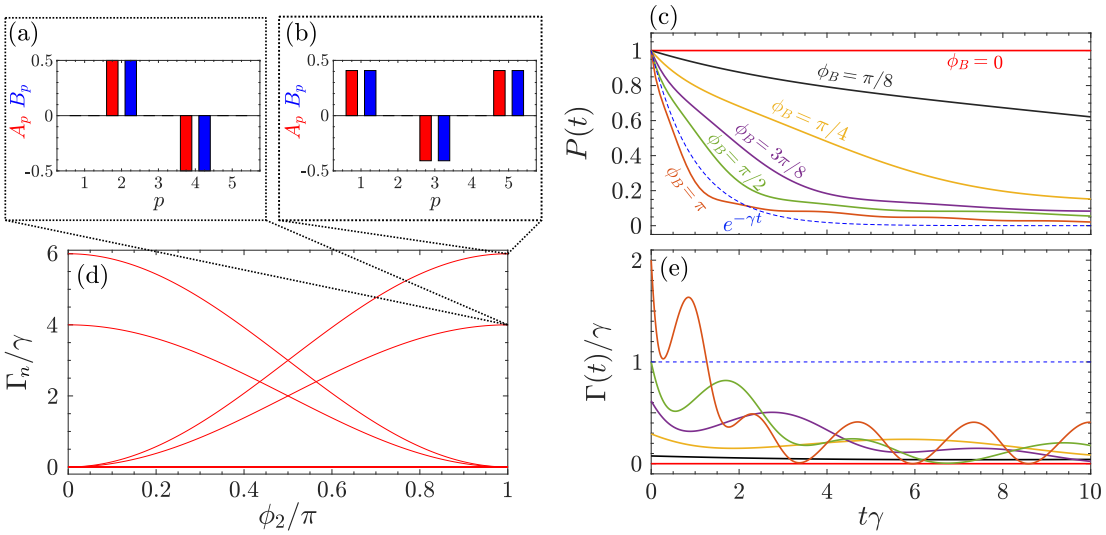

Figure 3.14: **Edge state decay vs ϕ_B. (a)** and **(b)**: Probability amplitudes of the superradiant decay modes when $\phi_B = \pi$. **(c)**: The population of the initial excitation $\left|\Phi(0)\right\rangle$ remaining at unit-less time $t\gamma$ for $\phi_B = 0$, $\pi/8$, $\pi/4$, $3\pi/8$, $\pi/2$ and π. Each represented by a different colour. The dynamic population decay of a single atom in the vicinity of the nanofiber (blue dashed) has been included for comparison. **(d)**: Decay rates of the decay channels as a function of ϕ_B. **(e)**: Normalised effective decay rate of $\left|\Phi(t)\right\rangle$ for the same values of ϕ_B (colours matching) as in (c). The effective decay rate of a single atom in the vicinity of the nanofiber (blue dashed) has been included here also for comparison.

constant in time. Since it is also non-zero we therefore see an approximately constant loss of excitation population.

3.8 Conclusions and Outlook

In this chapter we have used an atom-waveguide QED system in order to probe the topological characteristics of long-range interacting systems as well as their decay properties. We restricted our analysis to the guided coherent and dissipative interactions throughout.

We have demonstrated that the waveguide QED system is exactly the same as the original SSH model in the nearest-neighbour interaction limit, exhibiting non-trivial topological insulator phases which give rise to zero-energy edge states that are naturally robust against disorder. Building on this we showed that the introduction of next-nearest-neighbour interactions can destroy the topological insulating phases of the model due to the breaking of chiral symmetry in the bulk Hamiltonian. As a result bulk-boundary correspondence can be lost and the robust edge states of the nearest-neighbour model no longer need to be present. In agreement with [82] we found that there were parameter regimes in which the bulk-boundary correspondence was retained. Here we find some semblance of the edge states of the nearest-neighbour limit remain when next-nearest-neighbour interactions were introduced. These states were not found to be as robust as their nearest-neighbour counterparts.

We then took advantage of the naturally long-range interactions of the waveg-

uide QED model to move to the fully connected regime. At first we manually retained the chiral symmetry of the bulk Hamiltonian. Here we found two noteworthy parameter regimes. The first guaranteed a completely periodic chain of atoms in which the eigenstates of the Hamiltonian are Fourier modes. The Fourier modes which had zero-energy were found to have equal population on each site of the chain. The bulk bands of this model were not found to be gapped however and thus we concluded that these flat Fourier states were not states in a topological insulator phase. The second noteworthy regime engineered zero coupling between the first and last atom. In this case we found zero-energy eigenstates of the Hamiltonian which were almost completely localised in the first and last cell of the atom chain. We finally showed that these localised eigenstates are extremely robust against external disorder. These states portray all of the static characteristics of topologically protected states.

We then re-introduce the interaction terms that break chiral symmetry of the bulk Hamiltonian to the fully connected model. Interestingly we once again find zero-energy eigenstates which are highly localised to the first and last cell of the atom chain. Once more we test the static robustness of these states against disorder and find that they are extremely robust. Furthermore we test this robustness against the dynamics of a state excited on one of the edges of the fully connected chain. We find that not only does the excitation remain at the boundary of the atom chain despite the introduction of disorder in the atomic position, but it is also a highly subradiant state. Even more interestingly we find that the Hamiltonian does not need to have an exact zero-energy eigenstate in order for this behaviour to be observed. These states portray all of the static characteristics of topologically protected states despite the fact we do not retain chiral symmetry in the bulk Hamiltonian and thus do not expect any bulk-boundary correspondence to hold.

Next we briefly investigated the dynamical properties of the edge excitation in the chiral symmetric system and found that the excitation population could be entirely transferred from on end of the chain to the other seemingly without any propagation through the middle of the chain. Theoretically, if one had a 'switch' which could turn on and off the chiral symmetry, the population could be transferred from one end of the chain to the other when chiral symmetry is retained, and then 'trapped' on either end by breaking the chiral symmetry at the right time.

Finally we explored the full range of decay characteristics of the edge state excitation mentioned previously. We found that by simply increasing the azimuthal angle ϕ_B between sublattices we can tune the effective decay of the excitation from being highly subradiant, in which the population of the state does not decay, to being highly superradiant, in which the population of the state decays rapidly.

We foresee difficulties in verifying these results experimentally. The main problem will be suppressing the interactions of the system coming from radiation channels, namely V_{ij}^u (see eqn. (2.117)) and Γ_{ij}^u (see eqn. (2.113)). However, if this problem is overcome we see these results contributing to the search for efficient storage and transportation methods for quantum information.

Since the publication of [132] we have come up with a way to engineer the system such that all of the J_{2p} interactions which destroy the topological insulator

phase are zero, and there is still some freedom in the J'_{2p-1} and J_{2p-1}. Previously we had tried setting $a = 2\pi/\beta_g$ or $a = \pi/\beta_g$ which made each $J_{2p} = 0$, however this also restricted $\left|J'_{2p-1}\right| = \left|J_{2p-1}\right|$ such that the system would always be at a topological phase transition point. Recently we have thought to also use the azimuthal angle of the atoms in order to engineer $J_{2p} = 0$. On paper we have done this by setting $a = \pi/(2\beta_g)$ and $\phi_{ij} = |i - j|\,\pi/4$, where ϕ_{ij} is found in Eq. (3.2a) and (3.2b). With the lattice constant set to half of the wavelength of the light in the fiber, and each nearest atom separated by an azimuthal angle $\pi/4$ we find that

$$J_{2p} = \frac{\gamma}{2}\sin\left(p\frac{\pi}{2}\right)\cos\left(p\frac{\pi}{2}\right). \tag{3.41}$$

Now if p is odd $\cos\left(p\frac{\pi}{2}\right) = 0$ and if p is even $\sin\left(p\frac{\pi}{2}\right) = 0$ such that we always have $J_{2p} = 0$. Importantly we find that

$$J'_{2p-1} \propto \sin\left[\beta_g b + \frac{\pi}{2}(p-1)\right], \tag{3.42a}$$

$$J_{2p-1} \propto \sin\left[\beta_g b - \frac{\pi}{2}p\right], \tag{3.42b}$$

such that now the amplitude of the two types of hoppings can differ. We have not investigated whether different topological phases can be probed using this setup as of yet.

Chapter 4

Photon Emission and Photon Correlations

4.1 Introduction

In this chapter we turn our attention to the degree of control one can achieve over the atomic emission of photons in similar atom-waveguide systems to that used in the previous chapter. In this case however we include the guided and unguided decay modes of the nanofiber and compare the emission into each. With the eventual aim of producing efficient quantum networks, we look to maximise the total fraction of the emission propagating into the guided modes whilst also investigating the flux and chirality (directionality) of this emission. We begin by briefly introducing the model for the system in Sec. 4.2, mainly outlining the differences between the system in this and in the previous chapter. We then investigate how two different atomic ensembles coupled to the waveguide emit radiation collectively when driven by a weak laser in section 4.3. We first do this for the case of resonant laser-driving and then we investigate the effects of driving with an off-resonant laser. In Sec. 4.4 we examine the correlations between emission of pairs of photons for the different atomic systems with resonant laser-driving. We examine these correlations as a function of atomic separation for for small system sizes. Lastly, we examine the effects of off-resonant laser-driving on the correlation functions of a system of two atoms. We find that we can engineer the system such that a large fractions of the emission from the atoms propagate into the fiber. For resonant driving there is a critical system size above which this fraction is larger for an ensemble of atoms with half on one side of the fiber and the other half on the opposite side, compared with an ensemble with all atoms on one side of the fiber. Interestingly we find that off-resonant driving for large system sizes produces large increases in this fraction of overall emission into the guided modes in both atomic ensembles. Finally we find correlated emission of photon pairs into the guided modes of the nanofiber. The nature of these correlations, i.e. bunched or anti-bunched photon emission, can be chosen by tuning the system parameters.

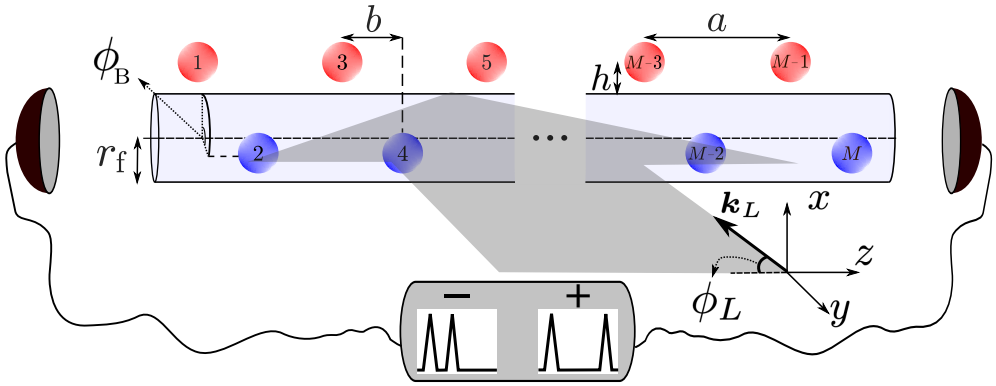

Figure 4.1: **System Setup.** Sublattice A (red) and B (blue) of two-level atoms with atomic transition wavelength $\lambda_a = 852.347$nm coupled to optical nanofiber of radius $r_f = 250$nm. The sublattices are at a radial height $h = 190$nm above the fiber and are offset by azimuthal angle ϕ_B and a distance b in the z direction. The electromagnetic field of a laser with wavevector $\boldsymbol{k}_L$ confined to the y-z plane (represented by the grey arrow) and at an angle ϕ_L causes emission of photons into the fiber in $\pm z$ direction which we see using detectors placed at the left($-$) and right($+$) ends of the nanofiber.

4.2 Model

As we see from Fig. 4.1, in this chapter we take a very similar system to that of the previous chapter. Once again we couple a sublattice array of M two-level atoms to a silica nanofiber waveguide of radius r_f with the atoms all at a radial height h above the nanofiber surface. The atoms in the same sublattice are separated by a distance a. The sublattices are offset in the z-direction by a distance b and by an azimuthal angle ϕ_B. A major difference from the previous chapter is that we will now include both the guided and unguided decay modes of the nanofiber in our calculations in order to describe a system closer to realistic experimental setups. We will aim to find parameter regimes where the emission into the guided modes is maximised compared to the emission into the unguided modes such that the photons are emitted into the nanofiber with a high probability instead of being lost to the radiation field. We still only consider the fundamental guided modes of the nanofiber. As well as this the atoms in this chapter are chosen to have circularly polarised dipole moments

$$\boldsymbol{d} = \frac{d}{\sqrt{2}}\begin{pmatrix} i & 0 & -1 \end{pmatrix}, \tag{4.1}$$

where we recall that $d = |\boldsymbol{d}|$. As a result the coupling between the atoms and the electric field of the fiber will differ to that of Chapter 3. The guided decay rates for example now take the form

$$V_{ij}^g = i\frac{d^2\omega\beta_g'}{8\epsilon_0}\sum_{lf}\mathrm{sgn}(fz_{ij})\Big[|e_r^g|^2\cos\phi_i\cos\phi_j + (e_z^g)^2 - ie_z^g e_r^g f(\cos\phi_j + \cos\phi_i)\Big]e^{if\beta_g z_{ij}}e^{il\phi_{ij}}, \tag{4.2a}$$

$$\Gamma_{ij}^{g} = \frac{d^2\omega\beta_g'}{4\epsilon_0}\sum_{lf}\Big[|e_r^g|^2\cos\phi_i\cos\phi_j + (e_z^g)^2 - ie_z^g e_r^g f(\cos\phi_j + \cos\phi_i)\Big]e^{if\beta_g z_{ij}}e^{il\phi_{ij}}, \tag{4.2b}$$

where we recall $z_{ij} = z_i - z_j$ and $\phi_{ij} = \phi_i - \phi_j$. The radiation decay rates cannot be simplified analytically and so are calculated numerically from Eqs. (2.117) and (2.113).

As discussed in Chapter 2, in order to probe the collective nature of the emission of this system we must first diagonalise the decay matrix Γ containing the components Γ_{ij}. Recall the eigenvalues of Γ give us the rate of the emission from collective eigenstates of the system. Let us also briefly recall that if this collective emission rate is faster (slower) than that of a single atom in the vicinity of the optical fiber, γ, the corresponding eigenstate is called superradiant (subradiant). We will now investigate how the parameters of two different ensembles of $M = 20$ atoms coupled to the nanofiber affect the collective decay rates of the system. The atomic ensembles we focus on are that with both sublattices placed above the fiber ($\phi_B = 0$) and that with the sublattices on opposite sides of the fiber ($\phi_B = \pi$) [see schematics in Fig. 4.2(a) and (b) respectively].

In Fig. 4.2(a) we see that for a regular array of atoms placed above the nanofiber, as the separation between atoms increases above half the wavelength of the light in the fiber a highly superradiant state emerges (light blue line). The black lines show that, of the two guided modes of the nanofiber, one is superradiant whilst the other is highly subradiant. The rest of the decay rates (coloured lines) decay quickly towards the single-atom decay rate as the atomic separation grows. We know from [23] that this is precisely how the free space decay modes behave, meaning that the presence of the nanofiber causes the emergence of the highly superradiant mode. We also know from [23] that the superradiant guided mode is that of the right moving mode in the fiber, and that the highly superradiant mode of the entire system has a high overlap with this guided mode. This is not surprising as the decay rates of the guided modes do not decay with the increased atomic separation, so it is specifically the presence of the guided modes of the nanofiber that cause the emergence of the highly superradiant mode.

In Fig. 4.2 (b) we see that when we alternate the position of the atoms above and below the fiber we get very similar results to the ensemble of atoms above the nanofiber. What differs is that there are, for the most part, two superradiant modes that split from the rest as the atomic z-separation is increased. We also see that the collective guided decay rates are very close to the single-atom decay rate except for when the atoms are separated by half-integer or integer numbers of the wavelength of light in the fiber. Interestingly, the guided modes do not simply split into the left- and right-propagating modes of the nanofiber. Instead they are (approximately) the equal symmetric and anti-symmetric superposition of the left- and right-propagating modes of the nanofiber. Once again we must attribute the persistent superradiant decay modes to the presence of the guided modes of the nanofiber.

In Fig. 4.2 (c) and (d), we observe that the highly superradiant decay modes in both systems are extremely sensitive to the radial height at which the atoms are located relative to the fiber surface. In either system we see that the separated,

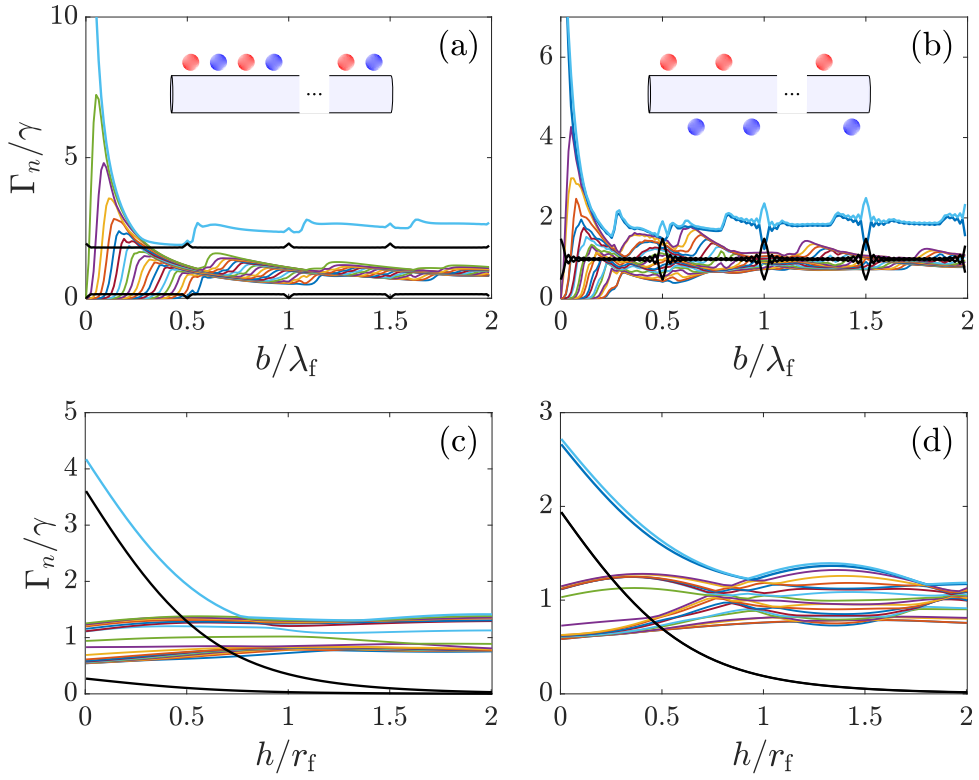

Figure 4.2: **Collective Decay Rates**. **(a)** and **(c)**: Total collective decay rates (coloured lines) and collective guided decay rates (black lines) of a system of 20 atoms with circularly polarised dipole moments placed in a regular array above the fiber (see schematic in (a)) as the separation between atoms b and the height of the atoms above the fiber h are varied respectively. The colouring of the atoms represent a sublattice structure which will be more important in the coming chapters. **(b)** and **(d)**: Same plots as in (a) and (c) but for a regular array of atoms which alternate above and below the fiber (see schematic in (b)). In all cases we have used a fiber of radius $r_f = 250$nm and identical circularly polarised atomic dipole moments with transition wavelengths $\lambda_a = 852.347$nm. In (a) and (b) the atoms were placed at a radial height $h/r_f = 0.36(90\text{nm})$ from the fiber and in (c) and (d) the atoms were separated by a distance $b/\lambda_f = 0.8(596\text{nm})$.

highly superradiant decay modes that exist for small h merge with the manifold of other decay modes at a height above the surface less than that of the fiber radius. As a result, we must be careful when choosing h in the rest of this thesis to ensure that the atoms are not too close to the fiber, which would invalidate the approximation used in Eq. (2.117), nor too far away, so that we can investigate the dynamics of highly superradiant modes of the system. Finally we note that Fig. 4.2 (c) and (d) show a similarity in the decay of the highly superradiant decay rates and that of the guided decay rate. This also hints towards a guided nature of the highly superradiant modes. In the rest of this chapter we will focus on comparing the stationary state emission properties of the two atomic ensembles mentioned above, namely that when $\phi_B = 0$ and that when $\phi_B = \pi$, when driven by a weak laser.

4.3 Fiber coupling efficiency and directionality in the weak driving limit

Introducing another electromagnetic field in the form of a single-mode laser modifies the Lindblad master equation (2.107) such that the coherent interactions become

$$\sum_{i\neq j} V_{ij}\sigma_i^+\sigma_j^- \rightarrow \sum_{i\neq j} V_{ij}\sigma_i^+\sigma_j^- + H_L \tag{4.3}$$

where

$$H_L = \sum_i \left(\Omega[e^{i\boldsymbol{k}_L\cdot\boldsymbol{r}_i}\sigma_i^+ + h.c.] + \Delta\sigma_i^+\sigma_i^-\right) \tag{4.4}$$

is the Hamiltonian of the laser. Recall Ω is the Rabi-frequency of the laser, $\boldsymbol{k}_L$ is the wavevector of the light emitted from the laser, $\boldsymbol{r}_i$ is the position of atom i and $\Delta = \omega_0 - \omega_L$ the detuning between the atomic transition and laser frequency. Throughout this chapter we confine the laser momentum to the yz-plane at an angle $\phi_L = \pi/2$, with Rabi-frequency $\Omega = 0.01\gamma$. With $\Omega \ll \gamma$ we can say the laser is in the weak-driving limit which allows us to assume that at most one excitation can be present in the system at any given time. In this limit we can once again apply the effective Hamiltonian method from Eq. (2.129) to numerically solve for the dynamics of the system.

In order to quantify the emission properties of the system we will use the photon flux [14]

$$N_P = \sum_{ij} \Gamma_{ij} \left\langle \sigma_i^+\sigma_j^- \right\rangle_{ss}, \tag{4.5}$$

where $\langle O\rangle_{ss}$ refers to the expectation value of the operator O in the stationary state (see Sec. 2.3.2 for details). We can split this total photon flux into its guided and unguided contributions, $N_P = N_P^g + N_P^u$, where the guided or unguided photon fluxes are isolated by simply replacing the full decay rates Γ_{ij} with the corresponding guided or unguided decay rates Γ_{ij}^g or Γ_{ij}^u respectively. We can even split the guided photon flux further into the right-moving(+) and left-moving(−) photons by using the directional decay rates of $\Gamma_{ij}^g = \Gamma_{ij}^+ + \Gamma_{ij}^-$. The right- and left-moving guided decay coefficients are Eq. 4.2b when $f = \pm 1$ respectively.

With this photon flux we can now calculate the fiber coupling efficiency(FCE)

$$\beta = \frac{N_P^g}{N_P^g + N_P^u}, \tag{4.6}$$

i.e. fraction of the overall expected photon decay which propagates into guided modes. Finally we define the chirality of the guided emission as

$$C = \frac{N_P^{g+} - N_P^{g-}}{N_P^{g+} + N_P^{g-}}, \tag{4.7}$$

such that $C = -1$ means all guided emission propagates to the left, $C = 1$ means all guided emission propagates to the right and $C = 0$ means there is equal emission propagating to the left and right along the nanofiber.

4.3.1 Resonant Driving ($\Delta = 0$)

In Refs. [22, 23], among others, it has been shown that for a single regular chain of atoms on the same side and in the vicinity of the nanofiber that this FCE can be dramatically enhanced when the angle of incidence of the laser and the lattice constant satisfy a so-called modified Bragg relation. In our case, where the laser momentum is perpendicular to the atoms, this condition is met when $a/(2\lambda_{\mathrm{f}}) = b/\lambda_{\mathrm{f}}$ is an integer. This can be understood as constructive interference between the light scattered by all of the atoms in the chain, leading to a maximum guided photon flux N_P^g. Since the wavelength of the unguided light is not exactly that of the guided light, rather a continuous range of values, this maximum constructive interference does not occur for N_P^u in the same parameter regime as for N_P^g and so we observe an enhancement in the FCE.

Here, we aim to find alternate configurations to the regular array of atoms that further enhance the FCE. First, we consider a bipartite lattice when all of the atoms are at the same azimuthal angle $\phi_B = 0$. For a system of $M = 20$ atoms we plot the FCE and the guided photon flux in Fig. 4.3(a) and (c) respectively as a function of a/λ_{f} and the offset distance between sublattices in units of the lattice constant b/a. As predicted by the Bragg condition we find a large enhancement of β and N_P^g at the same value of $a/\lambda_{\mathrm{f}} = 2$ and $b/a = 0.5$ (this enhancement repeats for each integer value of $a/(2\lambda_{\mathrm{f}})$). Furthermore, this happens to be the maximum β and N_P^g achievable in our parameter space for this configuration of atoms.

We next consider a bipartite sublattice with the chains of atoms on opposite sides of the fiber i.e. $\phi_B = \pi$. In Fig. 4.3(b) and (d) we plot β and N_P^g respectively for the configuration of atoms alternating on either side of the nanofiber. In this configuration we find that these quantities are enhanced not only for $a/(2\lambda_{\mathrm{f}})$ an integer, but also for half integer values. This can be interpreted as each atomic chain independently satisfying the Bragg condition and the interactions between the chains cause the modulation of β and N_P^g with b/a. When $a/\lambda_{\mathrm{f}} = 2$ and $b/a = 0.5$, the individual chains and the full bipartite lattice satisfy the Bragg condition leading to the maximum values of N_P^g and β. In the situation with $a/\lambda_{\mathrm{f}} = 1$ however, only atoms separated by two or more sites can satisfy the Bragg condition and thus the enhancement of N_P^g and β is not as pronounced compared to when $a/\lambda_{\mathrm{f}} = 2$. For a system of $M = 20$ atoms we see that we can achieve a little over 40% guided emission when $\phi_B = 0$ and a little less than that when $\phi_B = \pi$.

We find that the chirality of the emission when $\phi_B = 0$ is $C = 0.844$, which is exactly the single-atom chirality found in [23] for $\phi_L = \pi/2$ and a/λ_{f} an integer. Thus we expect a large percentage of the guided emission to propagate in the $+z$-direction. When $\phi_B = \pi$ on the other-hand, the chirality C is always zero and so we always have equal emission into guided modes propagating in opposite directions. This is because any chirality exhibited by the atomic chain above the fiber will be canceled out by the exact negative chirality of the atomic chain below the fiber. This is always true when all atoms have the same transition dipole moments and $\phi_B = \pi$.

As we expect (for resonant driving) that the maxima of β and N_P^g occur when the modified Bragg condition is met, we now fix this atomic separation and investigate the effects of the system size on the emission properties for the

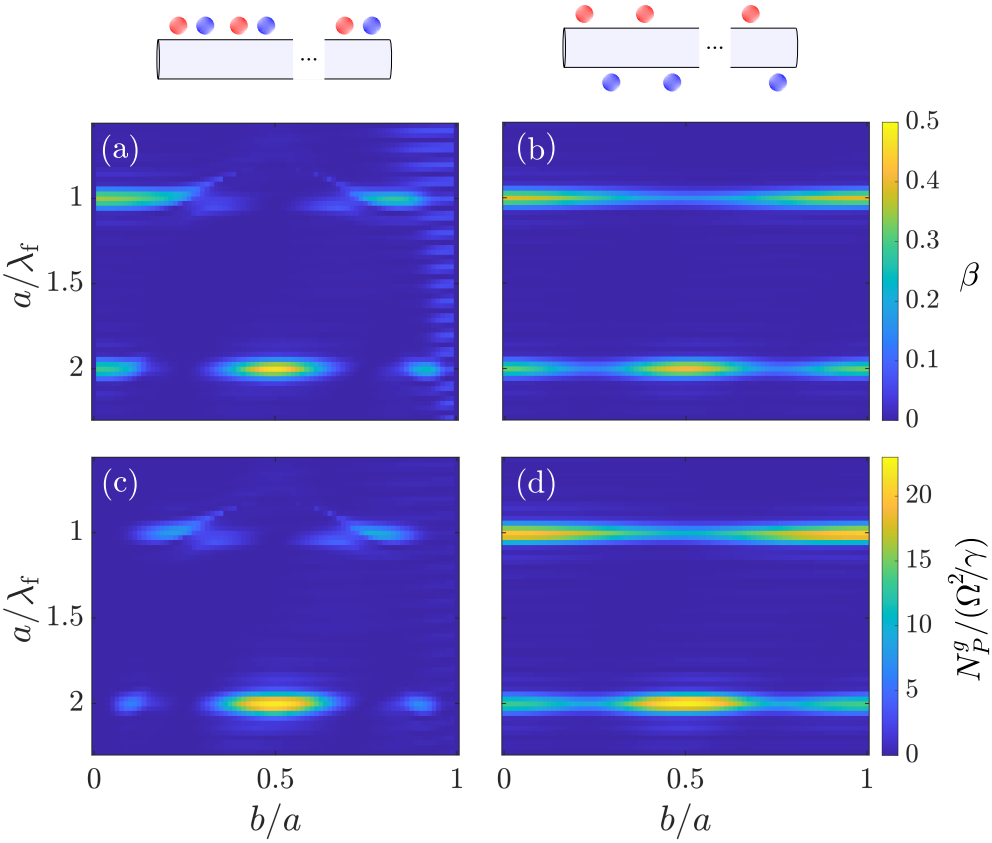

Figure 4.3: **Emission Properties of** $M = 20$ **Atoms**. **(a)** and **(b)**: β and N_P^g (scaled by the approximate total emission of one atom Ω^2/γ) respectively for $\phi_B = 0$. **(c)** and **(d)**: β and $N_P^g/(\Omega^2/\gamma)$ respectively for $\phi_B = \pi$. All quantities are calculated as a function of the lattice constant a, scaled by the wavelength of the light in the fiber λ_f, and the sublattice offset distance a, scaled by the lattice constant a.

different atomic configurations. We find in Fig. 4.4(a) that when the number of atoms increases above $M = 32$ the FCE of the atomic arrangement with $\phi_B = \pi$ becomes larger than the arrangement with $\phi_B = 0$. We also find that the FCE when $\phi_B = 0$ plateaus at $\beta \approx 0.542$ for as few as $M = 50$ atoms, whereas for $\phi_B = \pi$ the FCE has not plateaued even as M approaches 150. We have not been able to adequately fit β as a function of M and so we cannot currently accurately predict the behaviour for larger values of M. We speculate that β will plateau before reaching 1 for $\phi_B = \pi$ in the infinite system size limit as we calculated $\beta = 0.675$ for $M = 300$ atoms, only a 0.3% increase from the FCE at $M = 148$ despite over doubling the number of atoms. We remark that for large system sizes, both atomic arrangements produce FCEs far larger than that of the single-atom FCE of $\beta_1 \approx 0.036$. More precisely we see the FCE increase by a factor of over 15 when $\phi_B = 0$ and by a factor of over 18 when $\phi_B = \pi$ (calculated for $M = 148$).

We find very similar results for the guided photon flux in Fig. 4.4(b). Once more there are a number of atoms, $M = 20$, above which N_P^g becomes larger when $\phi_B = \pi$. When $\phi_B = 0$ we see N_P^g also plateaus for a relatively small number of atoms at a value of $N_P^g/(\Omega^2/\gamma) \approx 30.12$. For the arrangement with $\phi_B = \pi$ we

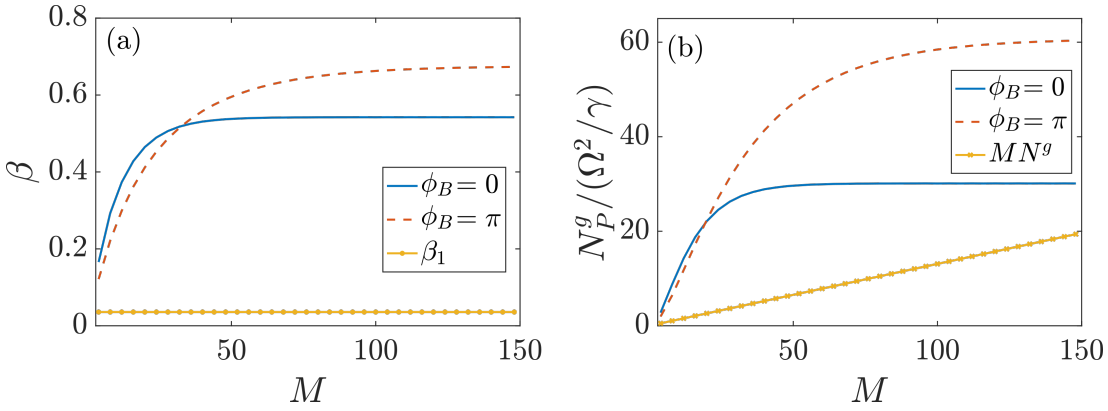

Figure 4.4: **Emission Properties vs System Size. (a)**: The fiber coupling efficiency as a function of the system size for the arrangement with all of the atoms above the fiber (blue solid line) and the arrangement with atoms alternating above and below the fiber (red dashed line). β_1 is the single-atom β-factor. **(b)**: The flux of guided photons emitted, scaled by the Rabi-frequency of the laser and single atom decay rate for the arrangement with all of the atoms above the fiber (blue solid line) and the arrangement with atoms alternating above and below the fiber (red dashed line). N^g is the single-atom guided photon flux (scaled by Ω^2/γ). We have satisfied the Brag condition using the parameters $b/a = 0.5$ and $a/\lambda_f = 2$.

see that, like β, N_P^g has not yet plateaued even for M approaching 150 atoms. As is the case for β, N_P^g could not be fit to a suitably accurate function and so we can only speculate whether the N_P^g value for $\phi_B = \pi$ does plateau. We expect it will plateau as for $M = 300$ atoms we find that $N_P^g/(\Omega^2/\gamma) \approx 60.74$ which is an increase of only 0.66% - a very small variation from $M = 148$ atoms.

If it is the case that N_P^g does plateau for the collective setups of $\phi_B = 0$ and $\phi_B = \pi$ then it is interesting to note from Fig. 4.4(b) that the guided emission from M independent emitters will, for large enough M, increase above both the guided photon flux of both collective atomic arrangements. Of course the unguided photon flux of the independent emitters will also increase such that the FCE in the independent system will remain very small at β_1.

4.3.2 Laser-driven superradiant emission

We provide here an attempt to explain the drastic enhancement of the FCE and guided photon flux seen above. We do this by first assuming that the collective state of the atoms that is excited by the weak laser takes the form [18]

$$|\psi\rangle = \sum_{i=1}^{M} \psi_i |e\rangle_i , \tag{4.8}$$

where $\psi_i = e^{i\boldsymbol{k}_L \cdot \boldsymbol{r}_i}/\sqrt{M}$. Since we choose the laser momentum to be perpendicular to the array of atoms we get $e^{i\boldsymbol{k}_L \cdot \boldsymbol{r}_i} = 1$ such that $|\psi\rangle$ is a symmetric superposition of all excited atom states. We can then calculate the effective decay rate of this excited state as

$$\Gamma_{|\psi\rangle} = \sum_k \Gamma_k \left| \sum_i D_{ik} \psi_i \right|^2 , \tag{4.9}$$

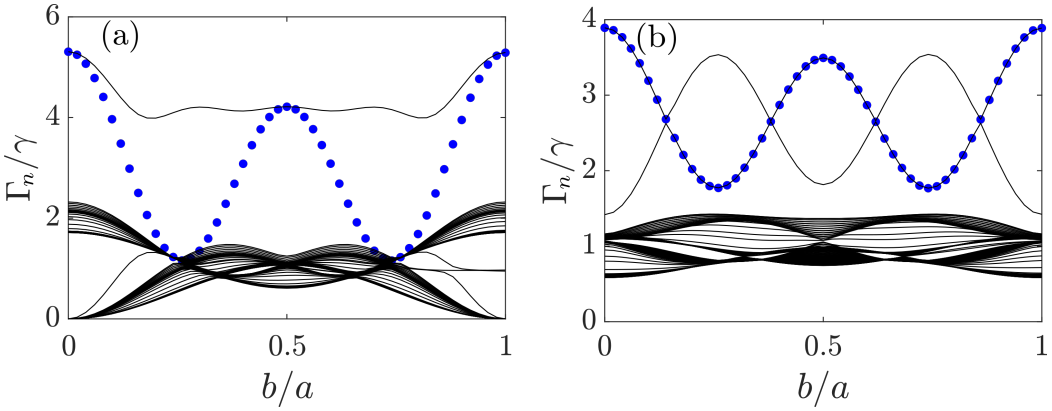

Figure 4.5: **Laser-Driven superradiant States**. **(a)**: Decay rates (black lines) of a system of $M = 100$ atoms with the effective decay rates of the laser-driven state (blue dots) for $\phi_B = 0$ as a function of the offset distance b in units of a. **(b)**: Same as plot (a) but for $\phi_B = \pi$. In both plots $a/\lambda_f = 2$ and the decay rates are scaled by the single atom decay rate γ.

where the matrix of D_{ik} values diagonalises the dissipation matrix Γ with corresponding collective decay rates Γ_k. Taking a system size of $M = 100$ atoms, $a/\lambda_f = 2$ and varying b/a we superimpose the effective decay rate of the laser-driven state on top of the true decay channel rates for $\phi_B = 0$ in Fig. 4.5(a) and $\phi_B = \pi$ in Fig. 4.5(b).

Despite the fact that the emission properties in Fig. 4.3 have been calculated with $M = 20$ one can see for $a/\lambda_f = 2$ that in both atomic arrangements the peaks in β and N_P^g occur when the effective decay rate of the laser-excited state matches the highly superradiant decay rate of the decay channels. Furthermore, in Fig. 4.5(a) we see that the regimes where the effective decay rate of $|\psi\rangle$ matches the decay rates of the manifold of eigenstates with much smaller decay rates, are precisely the regimes where the minima of the emission quantities β and N_P^g occur. As the waveguide only has two guided modes we thus conclude that, in these regimes, the laser must be driving decay into the unguided modes. In Fig. 4.5(b) we find that when $\phi_B = \pi$, the effective decay rate of the laser-excited state matches that of one of the superradiant decay modes irrespective of b. This behaviour would explain the 'strip' of increased β and N_P^g seen in Fig. 4.3(c) and (d) when $a/\lambda_f = 2$. We can understand this as each chain of atoms on either side of the fiber satisfying their own modified Bragg condition irrespective of b, and the interactions between the chains collectively enhancing this effect when $b/a \approx 0.5$. The regimes where β and N_P^g decrease in Fig. 4.5(b) correspond to the values of b/a for which the decay rate of the driven state is closest to the multitude of decay rates corresponding to unguided decay.

Such large values of β and N_P^g, when the effective decay rate of $|\psi\rangle$ matches the decay rates of the highly superradiant decay modes, leads us to conclude that these particular decay modes have a high overlap with one ($\phi_B = 0$) or an equal superposition of both ($\phi_B = \pi$) of the guided modes of the nanofiber. Expecting to drive an equal superposition of the left- and right-propagating guided modes when the atomic chains are on opposite sides of the nanofiber is another way to see why the chirality is zero for this system.

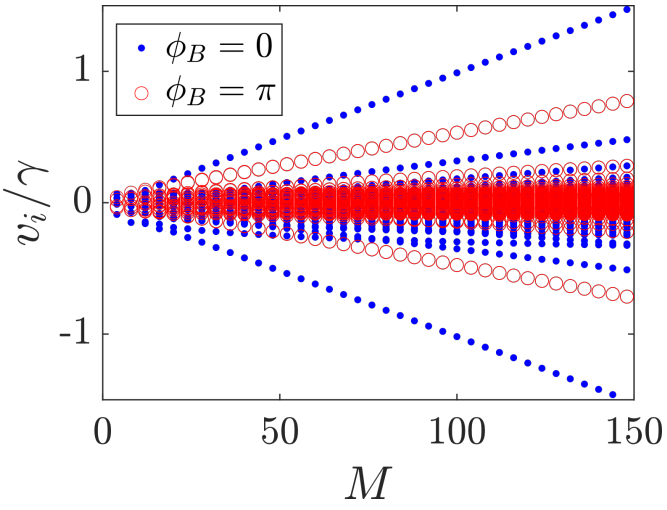

Figure 4.6: **Coherent Eigenvalues vs System Size.** Coherent energy eigenvalues $V|\psi_i\rangle = v_i|\psi_i\rangle$, where V is the matrix of V_{ij} rates, show a splitting which is more pronounced for the $\phi_B = 0$ setup (blue dots) compared to when $\phi_B = \pi$ (red circles).

4.3.3 Off-Resonant Driving ($\Delta \neq 0$)

In this section we will alter the detuning of the laser, Δ, such that it is no longer on-resonance with the atomic transition frequency. Since the highly superradiant states in Fig. 4.5(a) and (b) are eigenstates of Γ, but not necessarily eigenstates of H_{eff}, we do not expect that the energy of the resonant laser will match the energy of the guided modes. This is because the energy of these eigenstates split from the rest of the energy eigenstates [see Fig. 4.6]. By varying Δ we can change the energy of the laser in an attempt to match more closely the energy of the guided modes.

We will once again focus on the regime with atoms regularly spaced by λ_{f} ($a/\lambda_{\text{f}} = 2$ and $b/a = 0.5$) and investigate how the emission quantities for different system sizes change now that Δ can be non-zero. We see in Fig. 4.7(a) and (b) that upon varying the detuning of the laser from -3γ to 3γ, the FCEs found in Fig. 4.4(a) can be greatly enhanced when the laser in no longer on-resonance with the atomic transition for both atomic ensembles, compared to that when the laser is resonant. Interestingly, a significant enhancement in the FCE with increased detuning, in both ensembles, only occurs above a particular system size which differs for the ensembles. When $\phi_B = 0$ these effects begin for system sizes around $M \approx 24$ atoms but for a much larger $M \approx 50$ when $\phi_B = \pi$. We see that for system sizes above these particular numbers β continues to increase the further away the laser frequency is from resonance. A FCE of approximately 0.871 is achievable for $\phi_B = 0$ and 0.837 for $\phi_B = \pi$.

In the case when $\phi_B = 0$, we find a 'valley' of β values around $\Delta = 0$ i.e. we find a very sharp increase in β (in the Δ direction) either side of $\Delta = 0$. This valley widens with increasing system size, thus the larger the system size, the more off-resonant the laser would need to be to see this sharp increase in β. When $\phi_B = \pi$ we also see a valley about $\Delta = 0$ however it is not as deep (β is not as small) as the $\phi_B = 0$ case. Interestingly it also does not widen as much with increased system size compared to when $\phi_B = 0$. As a result, probing the high

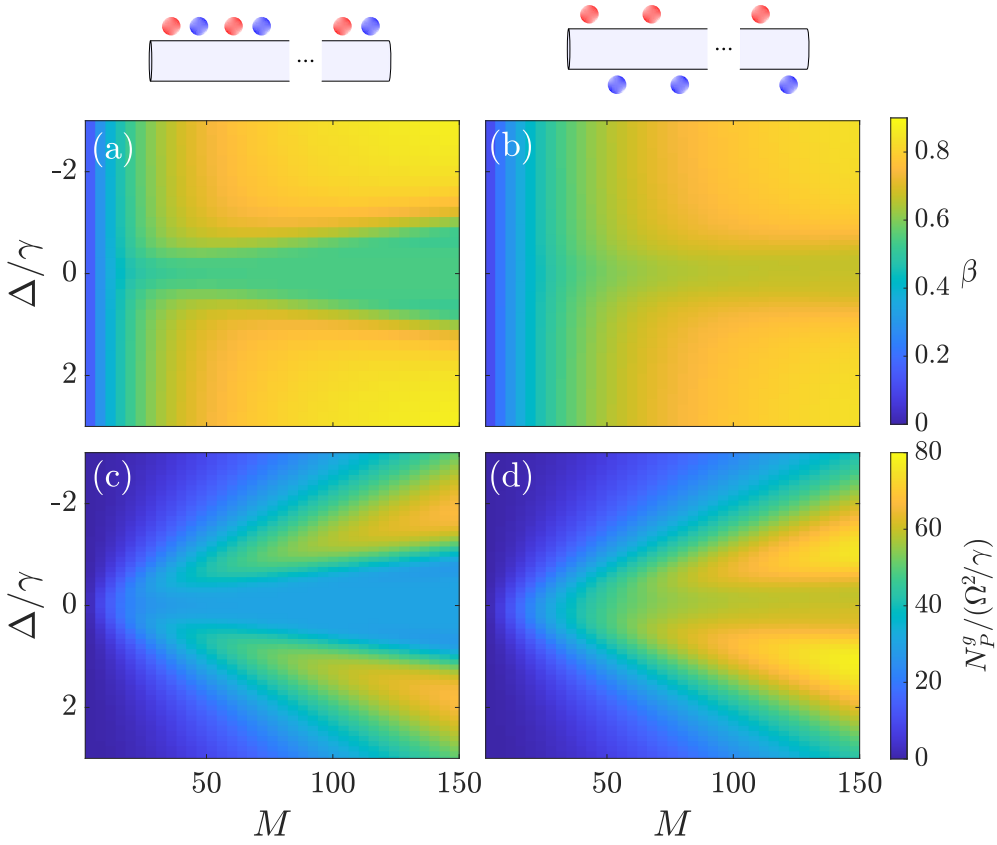

Figure 4.7: **Emission Properties with Detuning and System Size (a)** and **(b)**: β and the scaled guided photon flux $N_P^g/(\Omega^2/\gamma)$ respectively as a function of the system size M and detuning of the laser Δ in units of the single-atom decay rate γ for $\phi_B = 0$, $b/a = 0.5$ and $a/\lambda_f = 2$. **(c)** and **(d)**: Same plots as (a) and (b) respectively but for $\phi_B = \pi$.

FCE dynamics of the $\phi_B = \pi$ ensemble would require a smaller laser detuning than the ensemble with $\phi_B = 0$. In realistic atomic systems, a larger detuning usually constitutes a higher probability that the ground state will couple with more than one excited state. Since we have modelled a system of two-level atoms here it is advantageous to keep the detuning as small as possible.

The guided photon flux exhibits similar behaviour to β as we find in Fig. 4.7(c) and (d). We find a valley of N_P^g values around $\Delta = 0$ which widens with system size more when $\phi_B = 0$ compared to when $\phi_B = \pi$. Once again this valley is not as deep when $\phi_B = \pi$. As one might expect, larger system sizes have the capability to emit more guided photons but we also find that a larger guided photon flux of $N_P^g/(\Omega^2/\gamma) \approx 75$ is achievable for the $\phi_B = \pi$ ensemble when $\Delta \approx \gamma$ in comparison to $N_P^g/(\Omega^2/\gamma) \approx 67$ for the $\phi_B = 0$ ensemble when $\Delta \approx 2\gamma$.

Unlike in the case of β, as we continue to increase $|\Delta|$ we eventually see a very large reduction in the guided photon flux. These resulting peaks of N_P^g in the Δ-M parameter space have also been observed in [18]. The eventual reduction in emission flux as $|\Delta|$ increases occurs because when the laser is very far off-resonant the atoms are much less likely to be excited. This reduction occurs at a smaller value of $|\Delta|$ when $\phi_B = \pi$. In this way, for a large number of atoms, one could choose Δ based on a desired flux of guided photons, knowing that these

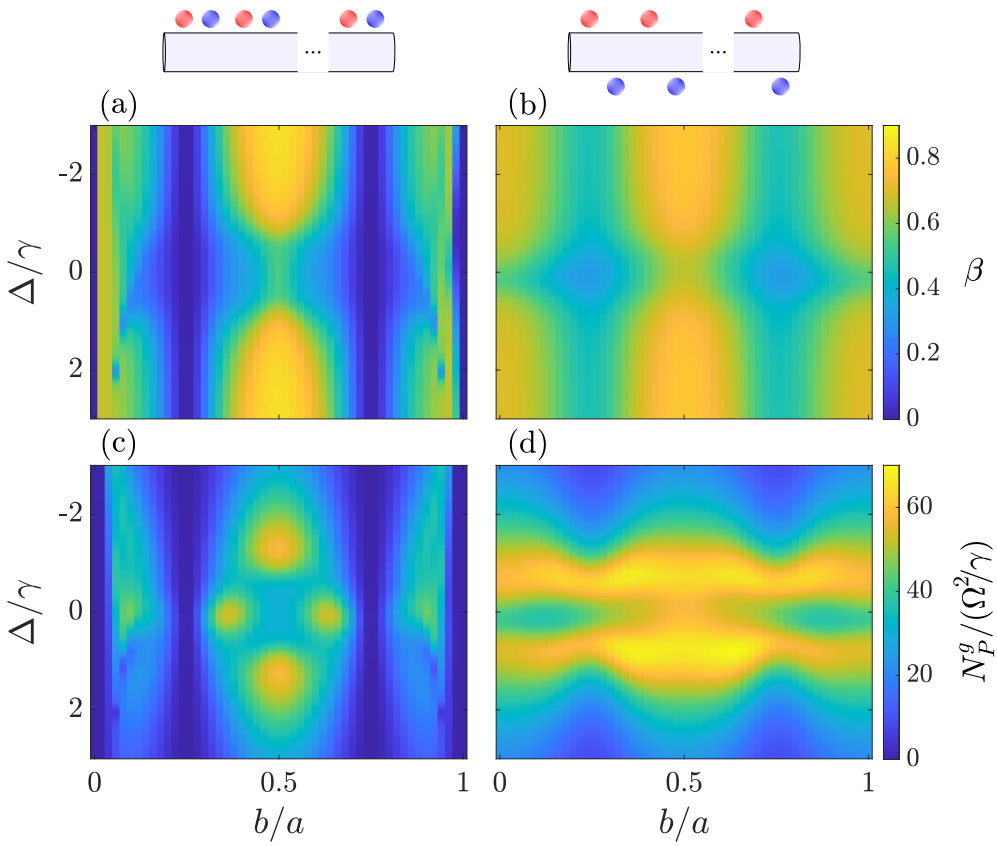

Figure 4.8: **Emission Properties with Detuning and Sublattice Offset**. **(a)** and **(b)**: β and the scaled guided photon flux $N_P^g/(\Omega^2/\gamma)$ respectively as a function of the sublattice offset b, in units of a, and detuning of the laser Δ in units of the single-atom decay rate γ for $\phi_B = 0$. **(c)** and **(d)**: Same plots as (a) and (b) respectively but for $\phi_B = \pi$.

photons would make up the vast majority of the total emission. Depending on the required directionality of the emission one can also choose between the $\phi_B = 0$ and $\phi_B = \pi$ ensembles of the atoms. The chirality of the ensemble of atoms all above the fiber can be reversed by placing all of the atoms below the fiber[1].

In Fig. 4.8 we take a system of $M = 100$ atoms and allow the offset between atomic chains to vary as well as the laser-atom detuning. We find that the FCE for the ensembles with $\phi_B = 0$ and $\phi_B = \pi$, plotted in Fig. 4.8(a) and (b) respectively, peak around $b/a = 0.5$. As we have already seen, β increases with increased detuning around $b/a = 0.5$. Interestingly, when all of the atoms are placed above the fiber one can tune the sublattice offset distance such that no guided emission occurs when b/a is around 0.25. At this offset value we have seen in Fig. 4.5(a) that the effective decay rate of the laser-excited state matches with the decay rates of the unguided modes. This is because when $b/a = 0.25$ the superradiant decay mode is an anti-symmetric superposition of the atom excited states compared to the symmetric superposition of atom excited states found when $b/a = 0.5$ which matches the phase pattern of the laser-excited state.

In Fig. 4.8(c) we once again see the peaks in N_P^g around $b/a = 0.5$ for $\phi_B = 0$

[1]It is equivalent to reverse the circular polarisation of the atomic dipole moments for the ensemble with all atoms above the nanofiber.

when the laser becomes off-resonant however we also see two smaller peaks when the laser is on-resonant which were not visible for a system of $M = 20$ atoms (see Fig. 4.3(b)). Previously the maximum N_P^g value for $M = 20$ atoms for an on-resonant laser was found at $b/a = 0.5$, suggesting a splitting of this peak which occurs with increasing system size. As one would expect the sublattice offset at which $\beta = 0$ shows no guided photon flux. Lastly, we find in Fig. 4.8(d) that when $\phi_B = \pi$ the peaks of N_P^g (at $\Delta \approx \gamma$) are almost independent of b/a. In fact there is an increase in the guided photon flux when b/a moves slightly away from 0.5. Since the modified Bragg condition is satisfied by the individual atomic chains, when they are above the nanofiber they must interfere destructively, in the context of significantly reducing the guided photon flux, at the offset distances in which N_P^g is very low. We do not see such drastic destructive interference when the chains are on the opposite sides of the fiber, meaning that the reduction in β around $b/a = 0.5$ is likely caused by a significant increase in the unguided photon flux N_p^u.

4.4 Photon-photon Correlations

So far in this chapter we have seen how varying levels of control are achievable over the collective emission from atomic chains in the vicinity of a nanofiber waveguide in the single-excitation regime. In particular we have seen how the relative position of the chains, and the separation between the atoms can have a significant impact on the fiber coupling efficiency as well as the chirality of the guided emission. In this section we will investigate the correlations between pair photon emission in both of the atomic ensembles studied so far. In order to do this we go beyond the single-excitation limit used so far, allowing for the possibility of having two excitations in the system at any given time. In the two-excitation limit the Hilbert space for M atoms has a dimension of $(M^2 + 1) \times (M^2 + 1)$ compared to a dimension of $(M + 1) \times (M + 1)$ in the single-excitation limit. Furthermore the effective Hamiltonian method used to simulate the stationary state dynamics in the single-excitation regime is no longer valid when two excitations are allowed because the single- and two-excitation subspaces couple to one another. In order to simulate the dynamics of the atom-waveguide QED system in the two-excitation limit we will employ the Choi-Jamiołkowski isomorphism detailed in Sec. 2.3.1. As this method requires matrices that scale as $(M^2 + 1)^2 \times (M^2 + 1)^2$ we will only investigate the correlations of photons emitted from a small number of atoms.

The normalised two-time second order correlation function is defined as

$$g^{(2)}(\tau) = \frac{\langle a^\dagger(t)a^\dagger(t+\tau)a(t+\tau)a(t)\rangle_{ss}}{\langle a^\dagger(t)a(t)\rangle_{ss}\langle a^\dagger(t+\tau)a(t+\tau)\rangle_{ss}} \tag{4.10}$$

where in our case $a^{(\dagger)}$ is the annihilation (creation) operator for a photonic mode in the fiber and the expectation values are calculated for the system in the stationary state. In simple terms, $g^{(2)}(\tau)$ is a measure of how correlated the emission of a photon at time t is with the emission of a photon at time $t+\tau$, normalised by the uncorrelated emission of a photon at time t and $t + \tau$ such that for uncorrelated photon emission $g^{(2)}(\tau) = 1$. In the long-time limit we always expect uncorrelated

photon emission i.e. $g^{(2)}(\tau \to \infty) = 1$. An important quantity to consider is $g^{(2)}(0)$, the same-time photon emission correlation function. In the literature $g^{(2)}(0)$ is used for a three-fold classification of the emission of photons;

$$g^{(2)}(0) > 1: \quad \text{Photon bunching,} \tag{4.11a}$$

$$g^{(2)}(0) = 1: \quad \text{Uncorrelated photons,} \tag{4.11b}$$

$$g^{(2)}(0) < 1: \quad \text{Photon anti-bunching.} \tag{4.11c}$$

As the names suggest, photon bunching implies the photons are most likely to be emitted in short pulses whereas photon anti-bunching implies delayed single photon emission. In the classical view of light one finds $1 \leq g^{(2)}(0) < \infty$ [111] which means that photon anti-bunching is a strictly quantum phenomenon. If the $g^{(2)}(\tau)$ function evolves monotonically towards one, the above classification is all one needs to capture the behaviour of the emitted photon correlations, however this is not always the case. A generalisation of this classification is to say that one observes photon bunching when $g^{(2)}(0) > g^{(2)}(\tau)$ and photon anti-bunching when $g^{(2)}(0) < g^{(2)}(\tau)$.

We can express the photonic operators in terms of a sum over all contributing modes as $a^{(\dagger)}(t) = \int d\omega \sum_{lf} a^{(\dagger)}_{\omega fl}(t)$ where $a^{(\dagger)}_{\omega fl}(t)$ is the annihilation (creation) operator for a photonic mode with frequency ω specifically propagating in the direction f and of polarisation l (recall we denoted this $a^{(\dagger)}_{\mu}(t)$ in Chapter 2). The equation of motion for these operators is [115]

$$\dot{a}_{\omega fl}(t) = \sum_i G^*_{\omega fli}\sigma_i^-(t)e^{i(\omega-\omega_0)t} + \sum_i \tilde{G}^*_{\omega fli}\sigma_j^+(t)e^{i(\omega+\omega_0)t}. \tag{4.12}$$

As is done in [118], we assume that the atoms only have a significant optical response to modes with frequency in such a narrow bandwidth centred around the transition frequency ω_0 that we can approximate $\omega \approx \omega_0$, such that

$$\dot{a}_{fl}(t) = \sum_i G^*_{\omega_0 fli}\sigma_i^-(t) + \sum_i \tilde{G}^*_{\omega_0 fli}\sigma_j^+(t)e^{i2\omega_0 t}, \tag{4.13}$$

where the $a_{fl}(t)(a^\dagger_{fl}(t))$ operators now only annihilate(create) photonic modes of frequency ω_0. The cosine and sine terms of $e^{i2\omega_0 t}$ approximately average to zero in the typical emission timescales we consider, leaving us with the solution

$$a_{fl}(t) = \sum_i G^*_{\omega_0 fli}\int_{t_0}^{t} dt'\sigma_i^-(t'), \tag{4.14}$$

By summing (4.14) over l only we obtain the annihilation operator for a photonic mode propagating in the $f = \pm$ z-direction i.e. $a_f(t) = \sum_l a_{fl}(t)$. We are interested in correlations between directional emission of the photons (not total emission) and so by replacing the terms in Eq. (4.10) with their directional counterparts ($a_f(t)$) we find the correlation between photons emitted in the f and f' direction to be

$$g^{(2)}_{ff'}(\tau) = \frac{\sum_{ijkn}\Gamma^f_{in}\Gamma^{f'}_{jk}\left\langle\sigma_i^+(t)\sigma_j^+(t+\tau)\sigma_k^-(t+\tau)\sigma_n^-(t)\right\rangle_{ss}}{\sum_{ijkn}\Gamma^f_{in}\Gamma^{f'}_{jk}\left\langle\sigma_i^+(t)\sigma_n^-(t)\right\rangle_{ss}\left\langle\sigma_j^+(t+\tau)\sigma_k^-(t+\tau)\right\rangle_{ss}}, \tag{4.15}$$

where Γ^f_{ij} are the components of the right($f = +$) or left($f = -$) propagating guided decay matrix.

4.4.1 On-Resonant Driving

$M = 2$ Atoms

First we will examine the directional same-time correlations ($g^{(2)}_{ff'}(0)$) for a system of $M = 2$ atoms as a function of b, the z-separation between between them. In Fig. 4.9(a) we find that when the atoms are placed above the nanofiber, one can observe photon bunching, photon anti-bunching or uncorrelated emission for each combination of directional emission by varying the atomic separation.

We find extreme photon bunching for each of the directional correlation functions when $b/\lambda_{\mathrm{f}} \approx 1/2, 3/2$ which is reminiscent of that found by Zheng and Baranger when they too consider Markovian dynamics [36]. We also find that the right-left photon correlations exhibit extreme anti-bunching when $b/\lambda_{\mathrm{f}} \approx 1/4, 3/4, 5/4, 7/4$. The correlation functions coincide when the atoms are separated by integer wavelengths of the guided light, at which points they all exhibit anti-bunching behaviour. There exist values of b/λ_{f} at which $g^{(2)}_{++}(0)$, $g^{(2)}_{--}(0)$ and $g^{(2)}_{+-}(0)$ behave as though the atoms were not interacting, however this never happens simultaneously for all of the directional correlation functions. Since we are examining the emission of simultaneous photons we note that $g^{(2)}_{+-}(0) = g^{(2)}_{-+}(0)$.

In Fig. 4.9(b) we plot the correlation functions now with the atoms on the opposite side of the nanofiber. Once more we see, for both of the directional correlation functions, photon bunching, anti-bunching and uncorrelated emission effects for different atomic z-separations. Once again we see the photon bunching peaking around $b/\lambda_{\mathrm{f}} \approx 1/2, 3/2$ however not to the same extent as the configuration with $\phi_B = 0$. Interestingly, when the atomic separation satisfies the modified Bragg condition ($b/\lambda_{\mathrm{f}} \in \mathbb{Z}$) we observe photon anti-bunching in both the right-right and right-left photon correlations with the former exhibiting more extreme photon anti-bunching than the latter. The non-interacting $g^{(2)}_{ff'}(0)$ functions differ for the different direction combinations when $\phi_B = \pi$, and once more we see atomic separations at which the interacting correlations behave as though the atoms were not interacting, but again this does not happen for both functions at the same atomic separation distance. We note that when $\phi_B = \pi$ we always find $g^{(2)}_{++}(0) = g^{(2)}_{--}(0)$.

In Fig. 4.10 we see how the correlated emission changes over time for different z-separations of the two atoms. In (a) and (c) we find that when the atoms are above the nanofiber, and the separation between them becomes less than about a quarter of the guided light wavelength, quantum beats emerge in both of the directional correlation functions. These quantum beats appear due to the interference between the transitions to the ground state from the symmetric and anti-symmetric superpositions of the two excited atoms, which are defined as

$$|\phi_+\rangle = \frac{1}{\sqrt{2}}\big(\,|e\rangle_1 + |e\rangle_2\,\big), \tag{4.16a}$$

$$|\phi_-\rangle = \frac{1}{\sqrt{2}}\big(\,|e\rangle_1 - |e\rangle_2\,\big), \tag{4.16b}$$

respectively (see for example Ch.1 Sec. 4 of [110]). In the superposition basis the symmetric and anti-symmetric states have energy eigenvalues $\omega_0 \pm |V_{12}|$ (recall $\hbar = 1$) respectively [36] and since we are driving with a resonant laser we see

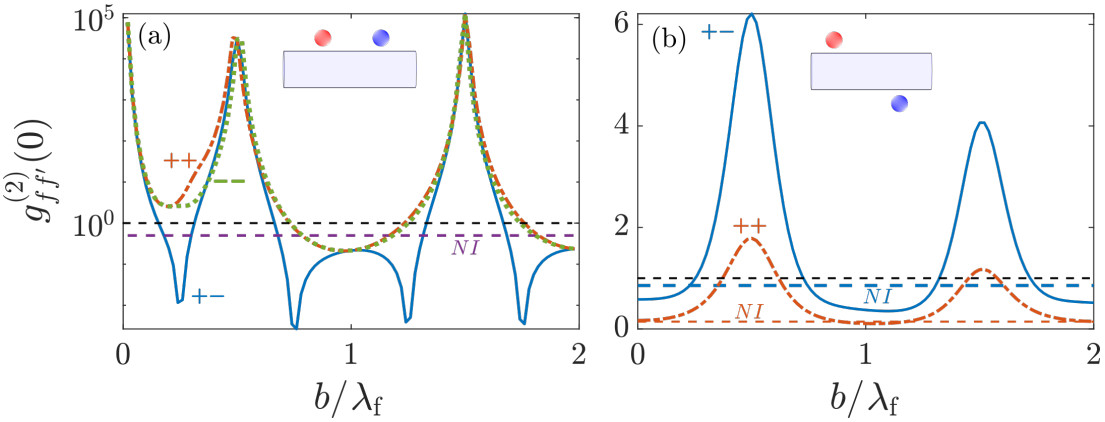

Figure 4.9: **Directional Same-time Photon Emission Correlations**. **(a)**: Log-scaled same-time right-right (red dot-dashes), left-left (green dashes) and right-left (blue line) correlations for two atoms above the fiber (see schematic) as a function of the atomic z-separation relative to the guided photon wavelength. The correlations for the corresponding non-interacting(NI) system of atoms is plotted (purple dashes) for comparison. When both atoms are above the fiber the non-interacting correlations are independent of the emission direction. **(b)**: Same-time directional photon correlations for a system of two atoms now on opposite sides of the fiber (see schematic). The non-interacting correlations for the right-right (red light dashes) and right-left (blue thick dashes) are plotted to match the colour of the corresponding interacting correlations. In both plots the uncorrelated limit $g^{(2)}(0) = 1$ (black dashes) is included for comparison.

the interference between these two states. The quantum beats become more persistent and their frequency increases as the atoms get closer to one another.

In contrast, Fig. 4.10 (b) and (d) show that when the atoms are placed on opposite sides of the nanofiber, quantum beats do not emerge irrespective of the z-separation of the atoms. When the atoms are separated by less that $\lambda_f/4$ we only find photon anti-bunching behaviour which relatively quickly becomes uncorrelated emission. Since the guided decay rates only depend on the z-separation between the atoms, we speculate that the unguided interactions must play a major role in the emergence of the quantum beats. In this way the atoms on opposite sides of the nanofiber never get close enough to one another (in absolute distance not just z-separation) in order to see quantum beats emerge from the interference between superposition states of the two atoms. This would also offer an explanation as to why the quantum beats found when $\phi_B = 0$ only emerge when the

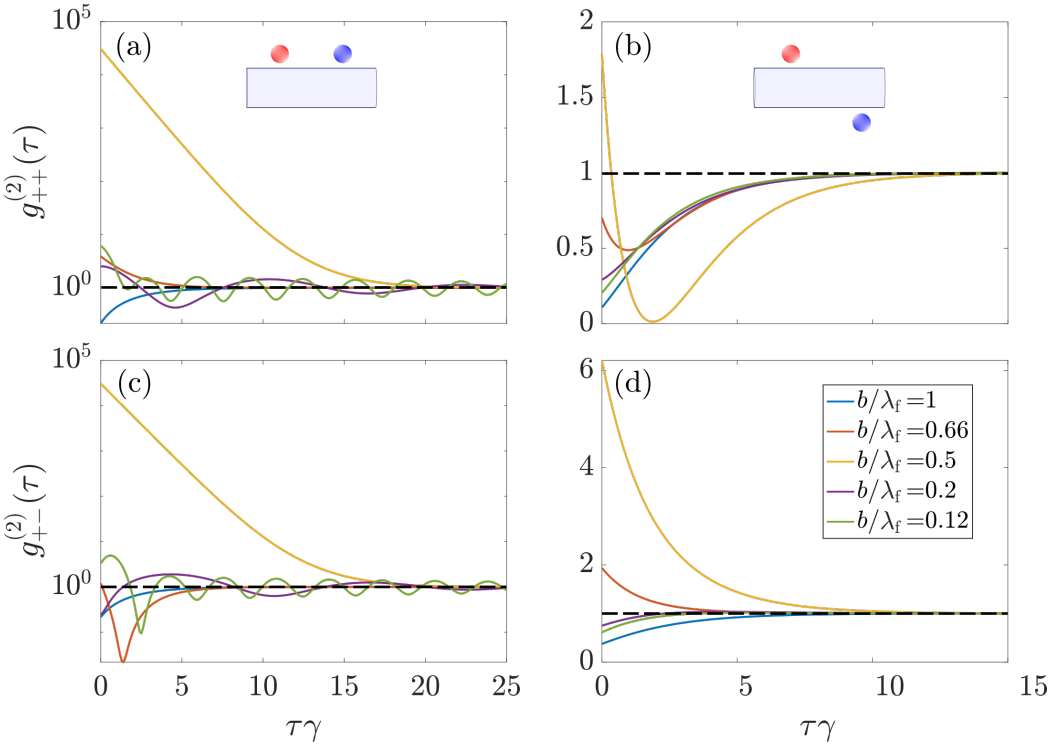

Figure 4.10: **Directional Photon Emission Correlations**. **(a)** and **(c)**: Log-scaled right-right and right-left emission correlations respectively for two atoms above the fiber (see schematic) with different separation distances, as a function of the unit-less time $\tau\gamma$. **(b)** and **(d)**: Right-right and right-left emission correlations respectively for two atoms on opposite sides of the fiber for the same z-separations. Coherent emission limit $g^{(2)}(0) = 1$ (black dashes) included for comparison.

atoms are close enough together. Preliminary results suggest that isolating the atomic system from the environment (thus removing the unguided interactions) eliminates the quantum beats found for $\phi_B = 0$ when $b < \lambda_f/4$.

$M > 2$ Atoms

We now increase the number of atoms in each sublattice and examine the effects of the sublattice offset distance on the $g^{(2)}(0)$ function. In Fig. 4.11(a) and (b) we find that when $\phi_B = 0$ one can achieve either photon bunching, photon anti-bunching or uncorrelated emission for both the right-right and right-left emission patterns by varying the sublattice offset as a function of a for a system of $M = 4, 6, 8, 10$ atoms. These photon bunching and anti-bunching effects are always less or equally as pronounced as those for a system of $M = 2$ atoms. As in the $M = 2$ case, we know that $g^{(2)}_{+-}(0) = g^{(2)}_{+-}(0)$. Interestingly we find that the system of $M = 4$ atoms exhibits perfect perfect photon anti-bunching ($g^{(2)}_{++}(0) = 0$) when $b/a \approx 0.18$.

Fig. 4.11(c) and (d) show the same-time right-right and right-left correlations respectively for $\phi_B = \pi$. For $M = 4, 6, 8, 10$ we find, irrespective of b/a, that only photon anti-bunching is possible for a pair of photons emitted in the $+z$-direction. We also find that $g^{(2)}_{++}(0)$ increases with system size, which in fact reduces the

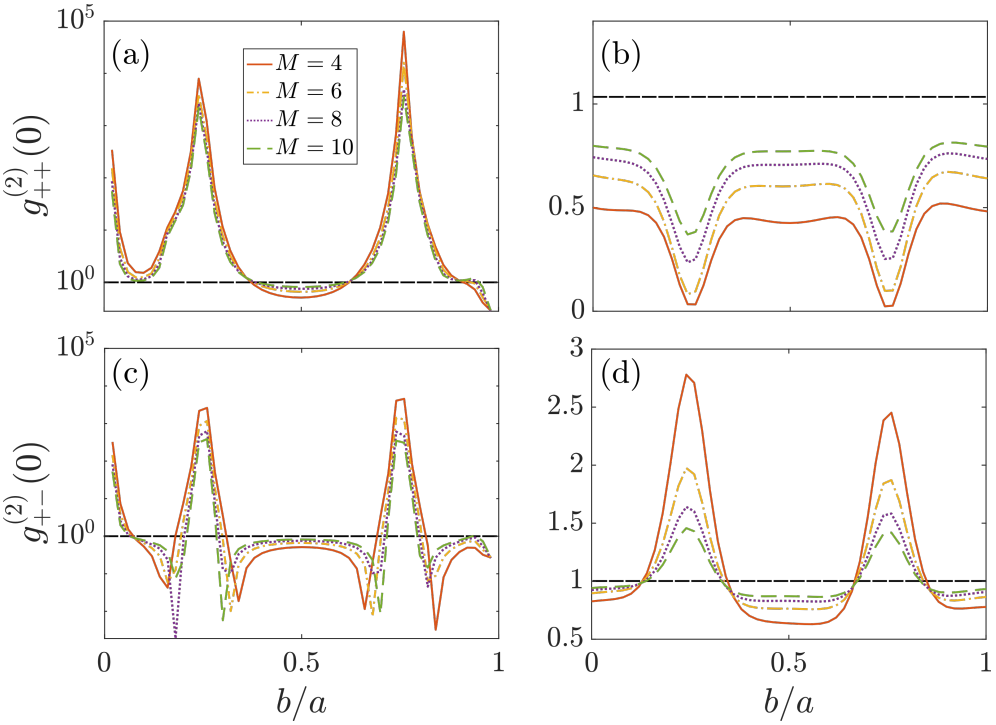

Figure 4.11: **Directional Same-time Photon Emission Correlations**. **(a)** and **(c)**: Log-scaled same-time right-right and right-left photon emission correlations respectively for $\phi_B = 0$ as a function of the sublattice offset b in units of a. **(b)** and **(d)**: Scaled same-time right-right and right-left photon emission correlations respectively for $\phi_B = \pi$ as a function of the sublattice offset b in units of a. All same-time correlations are calculated for a system of $M = 4$ (red line), $M = 6$ (yellow dot-dashes), $M = 8$ (purple dots) and $M = 10$ (green dashes) atoms. The uncorrelated limit $g^{(2)}(0) = 1$ (black dashes) is included for comparison.

anti-bunching effects no matter the offset between atomic chains.

On the other hand one can achieve photon bunching, anti-bunching or uncorrelated emission of a pair of right and left moving photons by tuning b/a. As in the case of $g^{(2)}_{++}(0)$, we notice that as the system size increases, the photon bunching and anti-bunching effects of $g^{(2)}_{+-}(0)$ become less pronounced. We speculate that adding more atoms to the system suppresses the correlations between simultaneously emitted photons and that for very large system sizes one would find the emission of simultaneous photon pairs to be random.

4.4.2 Off-Resonant Driving

We now examine how the introduction of detuning between laser and atomic transition frequencies affects the correlation functions $g^{(2)}_{ff'}(\tau)$ of a system of $M = 2$ atoms. We will first choose $b/\lambda_f = 1$ such that each of the directional same-time photon correlations show anti-bunching behaviour in $g^{(2)}_{ff'}(0)$.

Once again we see in Fig. 4.12(a)-(d) that when the system is driven by a resonant laser, the anti-bunching behaviour for each of the directional photon-emission combinations persist with τ since $g^{(2)}_{ff'}(\tau) > g^{(2)}_{ff'}(0)$. However when we introduce the atom-laser detuning we see the emergence of quantum beat

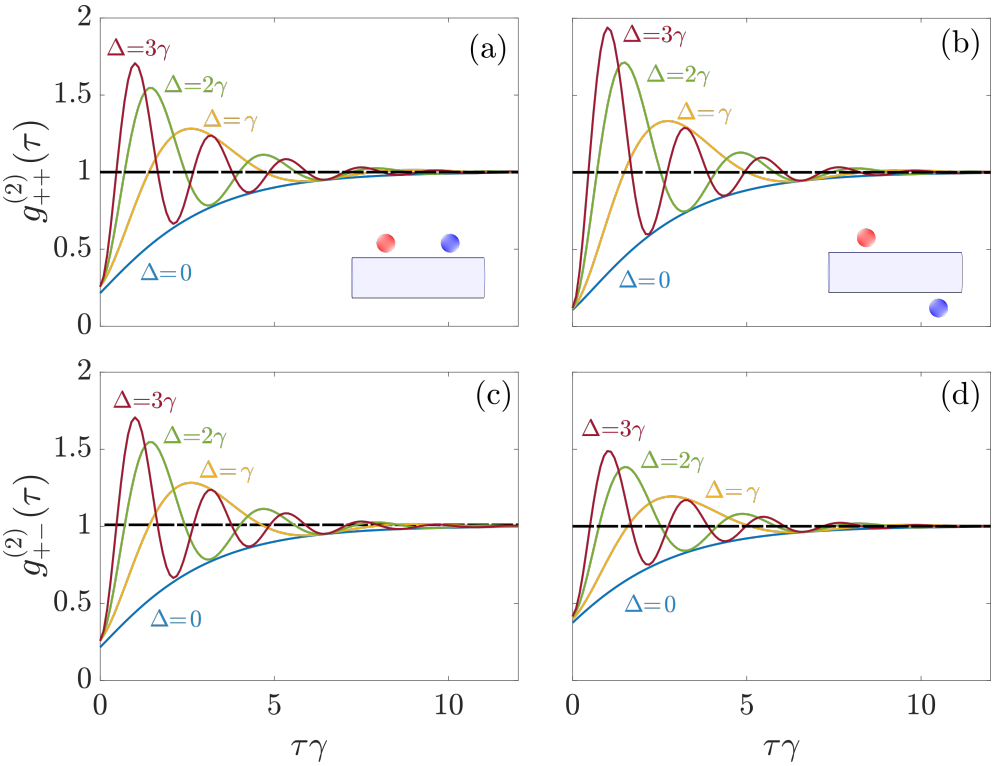

Figure 4.12: **Initial Photon Anti-Bunching**. **(a)** and **(c)**: Right-right and right-left time-separated photon emission correlations respectively for $\phi_B = 0$. **(b)** and **(d)**: Right-right and right-left time-separated photon emission correlations respectively for $\phi_B = \pi$. In all plots the atoms are separated in the z-direction by a distance $b = \lambda_f$. We calculated the correlations for different values of the laser detuning (see labels in plots) and compared them to the uncorrelated limit $g^{(2)}(\tau) = 1$ (black dashed line).

behaviour in the $g^{(2)}_{ff'}(\tau)$ functions. In all cases the frequency and amplitude of the quantum beats increase as the detuning is increased. This makes sense since an increase in detuning would increase the effective Rabi-frequency of the laser. These oscillations in the directional photon-emission correlations caused by the quantum beats suggest that pairs of photons have preferred 'wait times' between emissions i.e. the times at which the peaks occur.

Finally we examine how the photon correlations depend on time in a regime where they are extremely bunched namely $b/\lambda_f = 1/2$. In Fig. 4.13(a) and (c) we find that a resonant laser with $\phi_B = 0$ always initially produces extreme photon bunching for the right-right and right-left emission respectively. For long time separations (τ up to $10/\gamma$) the introduction of laser detuning does not alter the bunching behaviour of the photon correlations as they decay approximately exponentially in these times. Eventually however, quantum beats do emerge for the off-resonant driven correlations when the atoms are on the same side of the fiber. We would expect photon pairs in this system to emit very close together in time.

In a similar manner, when $\phi_B = \pi$ we find in Fig. 4.13(b) that a resonant laser initially produces photon bunching behaviour in the right-right emission. The resonant right-right photon emission correlations for $\phi_B = \pi$ in Fig. 4.13(d)

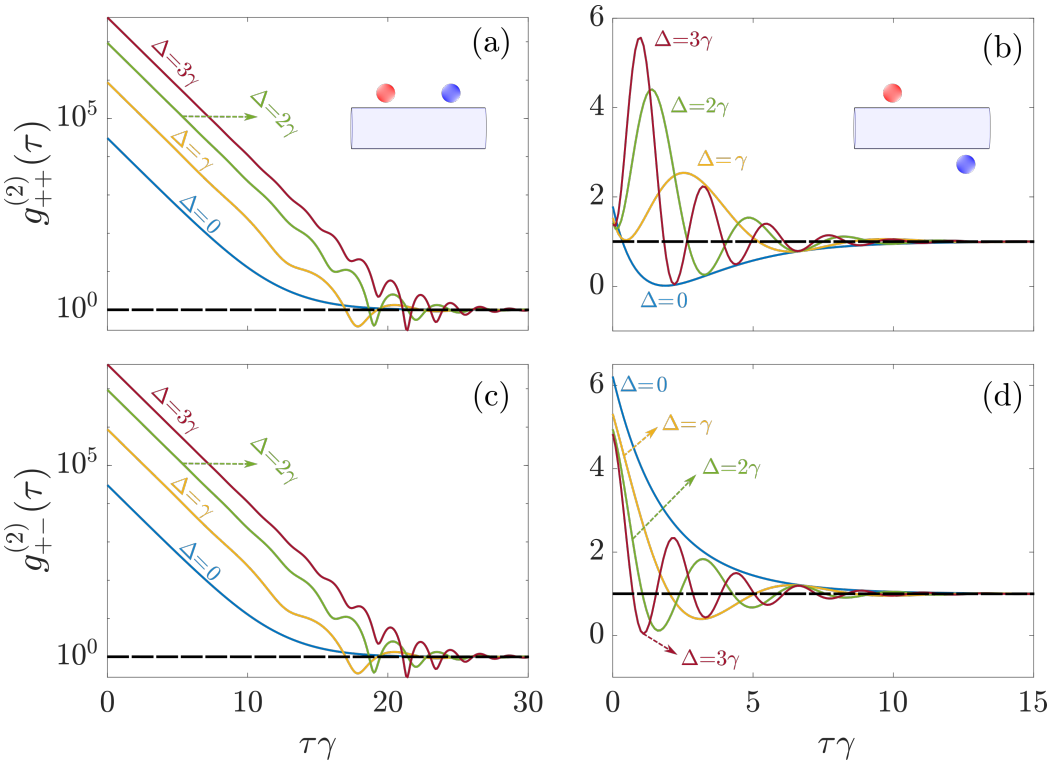

Figure 4.13: **Photon Bunching and Quantum Beats**. **(a)** and **(c)**: Log-scaled right-right and right-left time-separated photon emission correlations respectively for $\phi_B = 0$. **(b)** and **(d)**: Right-right and right-left time-separated photon emission correlations respectively for $\phi_B = \pi$. In all plots we have used an atomic separation of $b/\lambda_f = 1/2$ and the uncorrelated limit $g^{(2)}(\tau) = 1$ is included (black dashed line) for comparison. We calculated the correlations for different values of the laser detuning as labelled in each plot.

also exhibits clear photon bunching.

Quantum beats also emerge for $b/\lambda_f = 0.25$ and $\phi_B = \pi$ when detuning is introduced to the laser. Unlike the case when $b/a = 0.5$, we find that the oscillation of $g^{(2)}_{++}(\tau)$ and $g^{(2)}_{+-}(\tau)$ are out of phase with one another. This means that at times where we expect bunching behaviour from $g^{(2)}_{++}(\tau)$, we expect anti-bunching behaviour from $g^{(2)}_{+-}(\tau)$ and vice-versa.

4.5 Conclusion and Discussion

In this chapter we have studied the guided emission properties of two chains of weakly laser-driven atoms coupled to a waveguide and found that for varying chain size and different arrangements of the atomic chains the flux and fraction of emission into the waveguide can be significantly enhanced or reduced. Introducing detuning between the laser and atomic transition frequency, we showed one could further enhance these guided emission properties. The weak-driving laser limit allowed us to focus on the single-excitation regime of the system, making numerical calculations of large systems possible.

Going beyond the single excitation limit allowed us to then examine directional two-photon guided correlation functions for photons emitted from systems with

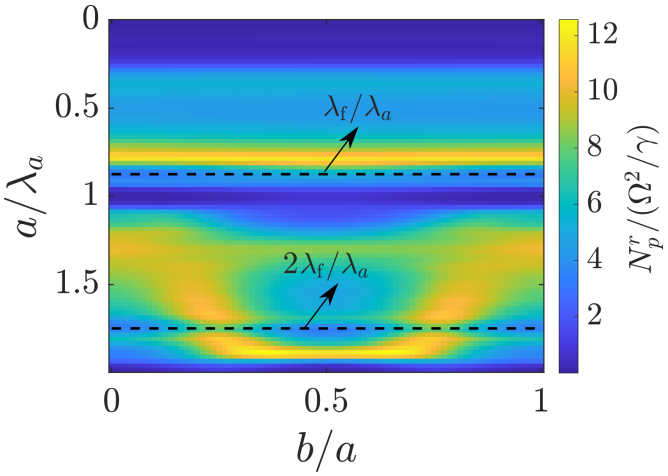

Figure 4.14: **Unguided Photon Flux**. The unguided photon flux for a system of $M = 20$ atoms alternating above and below a nanofiber waveguide identical to that used in Fig. 4.3, calculated as a function of the lattice constant a in units of the atomic transition wavelength λ_a and the sublattice offset distance b in units of a. The dotted lines represent the values of a at which maxima of N_P^g were found in Fig. 4.3(d).

a small number of atoms where we found this emission to exhibit both photon bunching and anti-bunching behaviour depending on the relative position of the atoms. Furthermore we found quantum beats emerging by moving two atoms on the same side of the fiber within a z-separation of $\lambda_f/4$. For two atoms on opposite sides of the fiber quantum beat behaviour emerged in the correlations only when the laser was off-resonance with the atomic transition.

In this analysis the atomic system was open, i.e. in contact with the environment, meaning these analyses are much closer to what is expected in real-life experiments compared to considering a closed atomic system. Further research in this area will be to investigate other atomic chain arrangements in a bid to enhance the guided emission properties even further. Using atoms of a different atomic transition frequency or having more than two chains of atoms are ways in which this may be possible.

There has been little work done here on the robustness of the FCE against disorder in either the position of the atoms or partial filling of the atomic chains. This would be valuable information for knowing what to expect in experiments where partial filling is common and the position of trapped atoms is never exact.

A natural extension for the results found here would be to increase the number of atoms in the system, both for the single-excitation regime calculations and for the correlation function analysis although the latter would require either more efficient numerical methods or far more computing power than we had access to.

Further to this, it could be insightful to explore in more detail the flux of the unguided radiation as a function of the system parameters. In Fig. 4.14 for example we plot the unguided flux for the $M = 20$ atom system explored in 4.3(d). We found that the guided photon flux was increased when $a/\lambda_f = 1, 2$ and we now see that the unguided photon flux is small at these values of a/λ_f. N_P^u is not minimised at these values however. This happens when the lattice constant is a multiple of the *atomic transition* wavelength. Thus one could look to engineer

the system such that the minimum of N_P^u and the maximum of N_P^g occur for the same lattice spacing. This may be achievable with a hollow nanofiber, as is done in [5], such that $\lambda_{\mathrm{f}} = \lambda_a$ although the complicated nature of Γ_{ij}^u makes it difficult to say for sure.

Chapter 5

Conclusion and Outlook

In this chapter we will state the main results of the research in this thesis and discuss how these results could be used for future research. We began by realising an SSH model in a closed atom-waveguide QED system where we recovered the expected bulk-boundary correspondence in the nearest-neighbour interacting limit and showed the resulting topological edge states are robust against local disorder in the atomic position. We then elucidated the destructive effects of breaking chiral symmetry and particle-hole symmetry of the model by introducing NNN interactions and how some edge states can be retained but are not as robust against disorder as their NN limit counterparts. In extending the system to long-range interactions we first manually retained chiral symmetry for the (almost) all-to-all interacting system of $M = 10$ atoms and discovered flat states which we concluded were not topological in nature due to closed bulk energy bands. Promising localised states at the edge of the system were then found and their robustness tested against disorder in the atomic position. To our surprise these states were found to be even more robust against this disorder than the NN system of $M = 100$ atoms. We then retained the symmetry breaking interactions and to our amazement we again found highly localised edge states which were shown to be highly robust against local disorder. What's more, when we opened the system up to the guided dissipation channels, we found that an excitation initially excited at one end of the chain would not dissipate at all, and its population will remain where it was initially excited. Even when disorder was introduced to the system the excitation population was retained for long times - matching each of the characteristics of topologically protected edge states. We then found that these same dynamics, once applied to the long-range system with chiral symmetry retained, also showed no signs of excitation population decay. Interestingly however, this time the population would move from one end of the chain to the other, seemingly without propagating through the fiber. Finally we investigated the effects of offsetting the sublattices by different azimuthal angles. We found that we could engineer varying 'speeds' of excitation population decay from the system into the dissipation channels.

Due to the omission of the unguided radiation in Chapter 3, in Chapter 4 we looked to investigate the emission properties of the atom-waveguide QED system without restrictions on the type of radiation present. We showed how we can probe the emission properties of two different atomic ensembles, namely that with all atoms above the nanofiber and that with atoms alternating above

and below the nanofiber, in the stationary state via weak laser-driving. After illustrating the collective nature of the decay in these system we investigated the effects that the lattice constant a and the sublattice offset b had on the emission properties of a system of $M = 20$ atoms driven by a resonant laser. We found that the fiber coupling efficiency parameter β and the guided photon flux N_P^g were maximised in both atomic ensembles when the atoms were all separated by multiples of the wavelength of the guided light.

We found that a greater FCE was achievable when all of the 20 atoms were above the fiber, however there was a critical system size above which the ensemble of alternating atoms exhibited a larger FCE. More than 65% of the of the photon emission could be expected to propagate into the nanofiber for large systems of alternating atoms driven by a resonant laser.

We then showed how well the effective decay rates matched that of the dissipation matrix Γ but explained how this does not guarantee driving exactly the decay modes of the full system. In order to do this we drove the system with an off-resonant laser. Varying the level of detuning between the laser and atomic transition frequencies we found a large increase in the possible FCEs of both atomic ensembles for large system sizes. We found that the ensemble of alternating atoms required a smaller detuning in order to reach these large FCE values. Varying the detuning was also shown to allow control over the flux of photons propagating into the nanofiber. In addition we wound that the large guided photon flux attainable via laser detuning was much more robust to changes in the offset between sublattices when the atoms alternated above and below the nanofiber.

Finishing out this chapter we find that the QED system in question, for both atomic ensembles, for a small number of atoms exhibit bunching and anti-bunching behaviour in the correlations between guided directional photon emission. For certain arrangements of the atoms one can also observe persistent quantum beats in these correlations.

A natural extension of this research would be to search for topologically non-trivial states of matter in this atom-waveguide QED system when the interactions through the radiation modes are included. In Fig. 4.14 we see that we can expect little to no radiation into the guided modes when the lattice constant is a multiple of the atomic transition wavelength and the atoms alternate above and below the fiber. For these lattice constants we have shown that non-trivial topological states of matter are possible albeit for a system with $V_{ij}^u = 0$ (and different dipole moments were chosen for the atoms). Investigating the emission properties of atoms with linear dipole moments would in itself be interesting, however if one was to find that the radiation photon flux from these atoms could also be approximately zero for some value of a which still allowed topological transitions, this would be a step closer to realising the topological states found in Chapter 3. It would be insightful to perform the same analysis of Chapter 3 without neglecting the V_{ij}^u interactions. Should the robust edge states be retained in this case, with the unguided photon flux eliminated, they would exist in a system completely open to environmental effects and could be searched for in experiments.

This research presents a step forward in the search for controllable quantum systems. It provides the platform for possible future detection of topologically

protected states of matter in a fully connected system, as well as enhanced control over emission of radiation in a quantum system.

Bibliography

[1] H. D. Zeh, "On the interpretation of measurement in quantum theory," *Foundations of Physics*, vol. 1, pp. 69–76, 3 1970.

[2] P. A. M. Dirac and N. H. D. Bohr, "The quantum theory of the emission and absorption of radiation," *Proceedings of the Royal Society of London. Series A, Containing Papers of a Mathematical and Physical Character*, vol. 114, pp. 243–265, 3 1927.

[3] E. M. Purcell, H. C. Torrey, and R. V. Pound, "Resonance Absorption by Nuclear Magnetic Moments in a Solid," *Physical Review*, vol. 69, pp. 37–38, 1 1946.

[4] H. Nha and W. Jhe, "Cavity quantum electrodynamics between parallel dielectric surfaces," *Physical Review A*, vol. 54, pp. 3505–3513, 10 1996.

[5] H. Nha and W. Jhe, "Cavity quantum electrodynamics for a cylinder: Inside a hollow dielectric and near a solid dielectric cylinder," *Physical Review A*, vol. 56, pp. 2213–2220, 9 1997.

[6] F. Le Kien, S. Dutta Gupta, V. I. Balykin, and K. Hakuta, "Spontaneous emission of a cesium atom near a nanofiber: Efficient coupling of light to guided modes," *Physical Review A*, vol. 72, p. 032509, 9 2005.

[7] Peyronel T, Firstenberg O, Liang QY, Hofferberth S, Gorshkov AV, Pohl T, Lukin MD, and Vuletić V., "Quantum nonlinear optics with single photons enabled by strongly interacting atoms.," *Nature*, vol. 488(7809), pp. 57–60, 8 2012.

[8] R. H. Dicke, "Coherence in spontaneous radiation processes," *Physical Review*, vol. 93, no. 1, pp. 99–110, 1954.

[9] R. H. Lehmberg, "Radiation from an N -Atom System. I. General Formalism," *Physical Review A*, vol. 2, pp. 883–888, 9 1970.

[10] G. S. Agarwal, "Master-Equation Approach to Spontaneous Emission," *Physical Review A*, vol. 2, pp. 2038–2046, 11 1970.

[11] J. Pellegrino, R. Bourgain, S. Jennewein, Y. Sortais, A. Browaeys, S. Jenkins, and J. Ruostekoski, "Observation of Suppression of Light Scattering Induced by Dipole-Dipole Interactions in a Cold-Atom Ensemble," *Physical Review Letters*, vol. 113, p. 133602, 9 2014.

[12] D. Pavolini, A. Crubellier, P. Pillet, L. Cabaret, and S. Liberman, "Experimental Evidence for Subradiance," *Physical Review Letters*, vol. 54, pp. 1917–1920, 4 1985.

[13] C. R. Stroud, J. H. Eberly, W. L. Lama, and L. Mandel, "Superradiant Effects in Systems of Two-Level Atoms," *Physical Review A*, vol. 5, pp. 1094–1104, 3 1972.

[14] F. Le Kien, S. D. Gupta, K. P. Nayak, and K. Hakuta, "Nanofiber-mediated radiative transfer between two distant atoms," *Physical Review A*, vol. 72, p. 063815, 12 2005.

[15] A. Albrecht, L. Henriet, A. Asenjo-Garcia, P. B. Dieterle, O. Painter, and D. E. Chang, "Subradiant states of quantum bits coupled to a one-dimensional waveguide," *New Journal of Physics*, vol. 21, p. 025003, 2 2019.

[16] A. A. Abdumalikov, O. V. Astafiev, Y. A. Pashkin, Y. Nakamura, and J. S. Tsai, "Dynamics of Coherent and Incoherent Emission from an Artificial Atom in a 1D Space," *Physical Review Letters*, vol. 107, p. 043604, 7 2011.

[17] D. Castells-Graells, D. Malz, C. C. Rusconi, and J. I. Cirac, "Atomic waveguide QED with atomic dimers," *Physical Review A*, vol. 104, p. 063707, 12 2021.

[18] B. Olmos, G. Buonaiuto, P. Schneeweiss, and I. Lesanovsky, "Interaction signatures and non-Gaussian photon states from a strongly driven atomic ensemble coupled to a nanophotonic waveguide," *Physical Review A*, vol. 102, p. 043711, 10 2020.

[19] Y.-L. L. Fang and H. U. Baranger, "Waveguide QED: Power spectra and correlations of two photons scattered off multiple distant qubits and a mirror," *Physical Review A*, vol. 91, p. 053845, 5 2015.

[20] K. Lalumière, B. C. Sanders, A. F. van Loo, A. Fedorov, A. Wallraff, and A. Blais, "Input-output theory for waveguide QED with an ensemble of inhomogeneous atoms," *Physical Review A*, vol. 88, p. 043806, 10 2013.

[21] S. J. Masson and A. Asenjo-Garcia, "Atomic-waveguide quantum electrodynamics," *Physical Review Research*, vol. 2, 11 2020.

[22] B. Olmos, C. Liedl, I. Lesanovsky, and P. Schneeweiss, "Bragg condition for scattering into a guided optical mode," *Physical Review A*, vol. 104, p. 043517, 10 2021.

[23] R. Jones, G. Buonaiuto, B. Lang, I. Lesanovsky, and B. Olmos, "Collectively Enhanced Chiral Photon Emission from an Atomic Array near a Nanofiber," *Physical Review Letters*, vol. 124, p. 093601, 3 2020.

[24] F. Le Kien and A. Rauschenbeutel, "Anisotropy in scattering of light from an atom into the guided modes of a nanofiber," *Physical Review A*, vol. 90, p. 023805, 8 2014.

[25] F. Le Kien and A. Rauschenbeutel, "Propagation of nanofiber-guided light through an array of atoms," *Physical Review A*, vol. 90, p. 063816, 12 2014.

[26] J. Petersen, J. Volz, and A. Rauschenbeutel, "Chiral nanophotonic waveguide interface based on spin-orbit interaction of light," *Science*, vol. 346, p. 67, 10 2014.

[27] S. Scheel, S. Y. Buhmann, C. Clausen, and P. Schneeweiss, "Directional spontaneous emission and lateral Casimir-Polder force on an atom close to a nanofiber," *Physical Review A*, vol. 92, p. 043819, 10 2015.

[28] R. Mitsch, C. Sayrin, B. Albrecht, P. Schneeweiss, and A. Rauschenbeutel, "Quantum state-controlled directional spontaneous emission of photons into a nanophotonic waveguide," *Nature Communications*, vol. 5, no. 1, p. 5713, 2014.

[29] C. Sayrin, C. Junge, R. Mitsch, B. Albrecht, D. O'Shea, P. Schneeweiss, J. Volz, and A. Rauschenbeutel, "Nanophotonic Optical Isolator Controlled by the Internal State of Cold Atoms," *Physical Review X*, vol. 5, p. 041036, 12 2015.

[30] S. M. Skoff, D. Papencordt, H. Schauffert, B. C. Bayer, and A. Rauschenbeutel, "Optical-nanofiber-based interface for single molecules," *Physical Review A*, vol. 97, p. 043839, 4 2018.

[31] C. Tabares, A. M. d. l. Heras, L. Tagliacozzo, D. Porras, and A. González-Tudela, "Variational waveguide QED simulators," *arXiv:2302.01922*, 2 2023.

[32] V. Paulisch, H. J. Kimble, and A. González-Tudela, "Universal quantum computation in waveguide QED using decoherence free subspaces," *New Journal of Physics*, vol. 18, no. 4, p. 043041, 2016.

[33] Y. Shen and J.-T. Shen, "Photonic-Fock-state scattering in a waveguide-QED system and their correlation functions," *Physical Review A*, vol. 92, p. 033803, 9 2015.

[34] S. Mahmoodian, M. Čepulkovskis, S. Das, P. Lodahl, K. Hammerer, and A. S. Sørensen, "Strongly Correlated Photon Transport in Waveguide Quantum Electrodynamics with Weakly Coupled Emitters," *Physical Review Letters*, vol. 121, p. 143601, 10 2018.

[35] A. S. Prasad, J. Hinney, S. Mahmoodian, K. Hammerer, S. Rind, P. Schneeweiss, A. S. Sørensen, J. Volz, and A. Rauschenbeutel, "Correlating photons using the collective nonlinear response of atoms weakly coupled to an optical mode," *Nature Photonics*, vol. 14, no. 12, pp. 719–722, 2020.

[36] H. Zheng and H. U. Baranger, "Persistent Quantum Beats and Long-Distance Entanglement from Waveguide-Mediated Interactions," *Physical Review Letters*, vol. 110, p. 113601, 3 2013.

[37] Y.-L. L. Fang, H. Zheng, and H. U. Baranger, "One-dimensional waveguide coupled to multiple qubits: photon-photon correlations," *EPJ Quantum Technology*, vol. 1, no. 1, p. 3, 2014.

[38] D. C. Tsui and A. C. Gossard, "Resistance standard using quantization of the Hall resistance of GaAs-$Al_xGa_{1-x}As$ heterostructures," *Applied Physics Letters*, vol. 38, pp. 550–552, 4 1981.

[39] K. v. Klitzing, G. Dorda, and M. Pepper, "New Method for High-Accuracy Determination of the Fine-Structure Constant Based on Quantized Hall Resistance," *Physical Review Letters*, vol. 45, pp. 494–497, 8 1980.

[40] R. B. Laughlin, "Quantized Hall conductivity in two dimensions," *Physical Review B*, vol. 23, pp. 5632–5633, 5 1981.

[41] D. J. Thouless, M. Kohmoto, M. P. Nightingale, and M. den Nijs, "Quantized Hall Conductance in a Two-Dimensional Periodic Potential," *Physical Review Letters*, vol. 49, pp. 405–408, 8 1982.

[42] M. V. Berry, "Quantal phase factors accompanying adiabatic changes," *Proceedings of the Royal Society A*, vol. 392, no. 1802, 1984.

[43] Y. Zhang, Y.-W. Tan, H. L. Stormer, and P. Kim, "Experimental observation of the quantum Hall effect and Berry's phase in graphene," *Nature*, vol. 438, no. 7065, pp. 201–204, 2005.

[44] C. Dutreix, H. González-Herrero, I. Brihuega, M. I. Katsnelson, C. Chapelier, and V. T. Renard, "Measuring the Berry phase of graphene from wavefront dislocations in Friedel oscillations," *Nature*, vol. 574, no. 7777, pp. 219–222, 2019.

[45] A. Hannonen, H. Partanen, A. Leinonen, J. Heikkinen, T. K. Hakala, A. T. Friberg, and T. Setälä, "Measurement of the Pancharatnam–Berry phase in two-beam interference," *Optica*, vol. 7, no. 10, pp. 1435–1439, 2020.

[46] C. L. Kane and E. J. Mele, "Quantum Spin Hall Effect in Graphene," *Physical Review Letters*, vol. 95, p. 226801, 11 2005.

[47] F. D. M. Haldane, "Model for a Quantum Hall Effect without Landau Levels: Condensed-Matter Realization of the "Parity Anomaly"," *Physical Review Letters*, vol. 61, pp. 2015–2018, 10 1988.

[48] B. A. Bernevig and S.-C. Zhang, "Quantum Spin Hall Effect," *Physical Review Letters*, vol. 96, p. 106802, 3 2006.

[49] K. Markus, W. Steffen, B. Christoph, R. Andreas, B. Hartmut, M. L. W, Q. Xiao-Liang, and Z. Shou-Cheng, "Quantum Spin Hall Insulator State in HgTe Quantum Wells," *Science*, vol. 318, pp. 766–770, 11 2007.

[50] N. Goldman, J. C. Budich, and P. Zoller, "Topological quantum matter with ultracold gases in optical lattices," *Nature Physics*, vol. 12, no. 7, pp. 639–645, 2016.

[51] R. J. Bettles, J. Minář, C. S. Adams, I. Lesanovsky, and B. Olmos, "Topological properties of a dense atomic lattice gas," *Physical Review A*, vol. 96, p. 041603, 10 2017.

[52] J. Perczel, J. Borregaard, D. Chang, H. Pichler, S. Yelin, P. Zoller, and M. Lukin, "Topological Quantum Optics in Two-Dimensional Atomic Arrays," *Physical Review Letters*, vol. 119, p. 023603, 7 2017.

[53] L. Lu, J. D. Joannopoulos, and M. Soljačić, "Topological states in photonic systems," *Nature Physics*, vol. 12, no. 7, pp. 626–629, 2016.

[54] S. Weimann, M. Kremer, Y. Plotnik, Y. Lumer, S. Nolte, K. Makris, M. Segev, M. Rechtsman, and A. Szameit, "Topologically protected bound states in photonic parity–time-symmetric crystals," *Nature Materials*, vol. 16, no. 4, pp. 433–438, 2017.

[55] T. Ozawa, H. M. Price, A. Amo, N. Goldman, M. Hafezi, L. Lu, M. C. Rechtsman, D. Schuster, J. Simon, O. Zilberberg, and I. Carusotto, "Topological photonics," *Reviews of Modern Physics*, vol. 91, p. 015006, 3 2019.

[56] M. Pan, H. Zhao, P. Miao, S. Longhi, and L. Feng, "Photonic zero mode in a non-Hermitian photonic lattice," *Nature Communications*, vol. 9, no. 1, 2018.

[57] P. St-Jean, V. Goblot, E. Galopin, A. Lemaître, T. Ozawa, L. Le Gratiet, I. Sagnes, J. Bloch, and A. Amo, "Lasing in topological edge states of a one-dimensional lattice," *Nature Photonics*, vol. 11, no. 10, pp. 651–656, 2017.

[58] N. L. M, K. Dustin, R. Alismari, V. Vincenzo, T. A. M, and I. W. T. M, "Topological mechanics of gyroscopic metamaterials," *Proceedings of the National Academy of Sciences*, vol. 112, pp. 14495–14500, 11 2015.

[59] B. Pérez-González, M. Bello, G. Platero, and Gómez-León, "Simulation of 1D Topological Phases in Driven Quantum Dot Arrays," *Physical Review Letters*, vol. 123, p. 126401, 9 2019.

[60] S. de Léséleuc, V. Lienhard, P. Scholl, D. Barredo, S. Weber, N. Lang, H. P. Büchler, T. Lahaye, and A. Browaeys, "Observation of a symmetry-protected topological phase of interacting bosons with Rydberg atoms," *Science*, vol. 365, p. 775, 8 2019.

[61] M. Atala, M. Aidelsburger, J. T. Barreiro, D. Abanin, T. Kitagawa, E. Demler, and I. Bloch, "Direct measurement of the Zak phase in topological Bloch bands," *Nature Physics*, vol. 9, no. 12, pp. 795–800, 2013.

[62] X.-W. Xu, Y.-J. Zhao, H. Wang, A.-X. Chen, and Y.-X. Liu, "Generalized Su-Schrieffer-Heeger Model in One Dimensional Optomechanical Arrays," *Frontiers in Physics*, vol. 9, 2022.

[63] X. Li, Y. Meng, X. Wu, S. Yan, Y. Huang, S. Wang, and W. Wen, "Su-Schrieffer-Heeger model inspired acoustic interface states and edge states," *Applied Physics Letters*, vol. 113, p. 203501, 11 2018.

[64] A. Kitaev, "Fault-tolerant quantum computation by anyons," *Annals of Physics*, vol. 303, pp. 2–30, 1 2003.

[65] C. Nayak, S. H. Simon, A. Stern, M. Freedman, and S. Das Sarma, "Non-Abelian anyons and topological quantum computation," *Reviews of Modern Physics*, vol. 80, pp. 1083–1159, 9 2008.

[66] B. Field and T. Simula, "Introduction to topological quantum computation with non-Abelian anyons," *Quantum Science and Technology*, vol. 3, no. 4, p. 045004, 2018.

[67] V. Lahtinen and J. Pachos, "A Short Introduction to Topological Quantum Computation," *SciPost Physics*, vol. 3, p. 021, 9 2017.

[68] A. P. Schnyder, S. Ryu, A. Furusaki, and A. W. W. Ludwig, "Classification of topological insulators and superconductors in three spatial dimensions," *Physical Review B*, vol. 78, p. 195125, 11 2008.

[69] S. Ryu, A. P. Schnyder, A. Furusaki, and A. W. W. Ludwig, "Topological insulators and superconductors: tenfold way and dimensional hierarchy," *New Journal of Physics*, vol. 12, p. 065010, 6 2010.

[70] M. Z. Hasan and C. L. Kane, "Colloquium: Topological insulators," *Reviews of Modern Physics*, vol. 82, no. 4, pp. 3045–3067, 2010.

[71] X.-L. Qi and S.-C. Zhang, "Topological insulators and superconductors," *Reviews of Modern Physics*, vol. 83, pp. 1057–1110, 10 2011.

[72] B. A. Bernevig, *Topological Insulators and Topological Superconductors*. Princeton University Press, 2013.

[73] Y. Ando, "Topological Insulator Materials," *Journal of the Physical Society of Japan*, vol. 82, p. 102001, 10 2013.

[74] J.-W. Rhim, J. H. Bardarson, and R.-J. Slager, "Unified bulk-boundary correspondence for band insulators," *Physical Review B*, vol. 97, p. 115143, 3 2018.

[75] X.-L. Qi, Y.-S. Wu, and S.-C. Zhang, "General theorem relating the bulk topological number to edge states in two-dimensional insulators," *Physical Review B*, vol. 74, p. 045125, 7 2006.

[76] L. Lepori and L. Dell'Anna, "Long-range topological insulators and weakened bulk-boundary correspondence," *New Journal of Physics*, vol. 19, p. 103030, 10 2017.

[77] D. Vodola, L. Lepori, E. Ercolessi, A. V. Gorshkov, and G. Pupillo, "Kitaev Chains with Long-Range Pairing," *Physical Review Letters*, vol. 113, p. 156402, 10 2014.

[78] D. Vodola, L. Lepori, E. Ercolessi, and G. Pupillo, "Long-range Ising and Kitaev models: phases, correlations and edge modes," *New Journal of Physics*, vol. 18, p. 015001, 12 2015.

[79] A. Alecce and L. Dell'Anna, "Extended Kitaev chain with longer-range hopping and pairing," *Physical Review B*, vol. 95, p. 195160, 5 2017.

[80] B.-H. Chen and D.-W. Chiou, "An elementary rigorous proof of bulk-boundary correspondence in the generalized Su-Schrieffer-Heeger model," *Physics Letters A*, vol. 384, no. 7, p. 126168, 2020.

[81] C. Li and A. Miroshnichenko, "Extended SSH Model: Non-Local Couplings and Non-Monotonous Edge States," *Physics*, vol. 1, pp. 2–16, 11 2018.

[82] B. Pérez-González, M. Bello, Gómez-León, and G. Platero, "Interplay between long-range hopping and disorder in topological systems," *Physical Review B*, vol. 99, p. 035146, 1 2019.

[83] H.-C. Hsu and T.-W. Chen, "Topological Anderson insulating phases in the long-range Su-Schrieffer-Heeger model," *Physical Review B*, vol. 102, p. 205425, 11 2020.

[84] L. Li, Z. Xu, and S. Chen, "Topological phases of generalized Su-Schrieffer-Heeger models," *Physical Review B*, vol. 89, p. 085111, 2 2014.

[85] W. P. Su, J. R. Schrieffer, and A. J. Heeger, "Solitons in Polyacetylene," *Physical Review Letters*, vol. 42, pp. 1698–1701, 6 1979.

[86] J. Zak, "Berry's phase for energy bands in solids," *Physical Review Letters*, vol. 62, pp. 2747–2750, 6 1989.

[87] J. K. Asbóth, L. Oroszlány, and A. P. Pályi, *A Short Course on Topological Insulators: Band Structure and Edge States in One and Two Dimensions*. Lecture Notes in Physics, Springer International Publishing, 2016.

[88] N. Batra and G. Sheet, "Understanding Basic Concepts of Topological Insulators Through Su-Schrieffer-Heeger (SSH) Model," *arXiv:1906.08435*, 6 2019.

[89] M. Bello, G. Platero, J. I. Cirac, and A. González-Tudela, "Unconventional quantum optics in topological waveguide QED," *Science Advances*, vol. 5, no. 7, 2019.

[90] E. Kim, X. Zhang, V. S. Ferreira, J. Banker, J. K. Iverson, A. Sipahigil, M. Bello, A. González-Tudela, M. Mirhosseini, and O. Painter, "Quantum Electrodynamics in a Topological Waveguide," *Physical Review X*, vol. 11, p. 011015, 1 2021.

[91] P. Boross, J. K. Asbóth, G. Széchenyi, L. Oroszlány, and A. Pályi, "Poor man's topological quantum gate based on the Su-Schrieffer-Heeger model," *Physical Review B*, vol. 100, p. 45414, 7 2019.

[92] E. Meier, F. An, and B. Gadway, "Observation of the topological soliton state in the Su-Schrieffer-Heeger model," *Nature Communications*, vol. 7, 2 2016.

[93] L. Thatcher, P. Fairfield, L. Merlo-Ramírez, and J. M. Merlo, "Experimental observation of topological phase transitions in a mechanical 1D-SSH model," *Physica Scripta*, vol. 97, p. 035702, 3 2022.

[94] M. Bello, G. Platero, and A. González-Tudela, "Spin Many-Body Phases in Standard- and Topological-Waveguide QED Simulators," *PRX Quantum*, vol. 3, p. 010336, 3 2022.

[95] D. Xie, W. Gou, T. Xiao, B. Gadway, and B. Yan, "Topological characterizations of an extended Su–Schrieffer–Heeger model," *npj Quantum Information*, vol. 5, no. 1, p. 55, 2019.

[96] Y. He and C.-C. Chien, "Non-Hermitian generalizations of extended Su–Schrieffer–Heeger models," *Journal of Physics: Condensed Matter*, vol. 33, p. 085501, 2 2021.

[97] J. J. Sakurai and J. Napolitano, *Modern Quantum Mechanics*. Cambridge University Press, 9 2017.

[98] M. Born and V. Fock, "Beweis des Adiabatensatzes," *Zeitschrift für Physik*, vol. 51, no. 3, pp. 165–180, 1928.

[99] K. Tosio, "On the Adiabatic Theorem of Quantum Mechanics," *Journal of the Physical Society of Japan*, vol. 5, no. 6, pp. 435–439, 1950.

[100] T. Suzuki, H. Nakazato, R. Grimaudo, and A. Messina, "Analytic estimation of transition between instantaneous eigenstates of quantum two-level system," *Scientific Reports*, vol. 8, no. 1, p. 17433, 2018.

[101] Y. Aharonov and D. Bohm, "Significance of Electromagnetic Potentials in the Quantum Theory," *Physical Review*, vol. 115, pp. 485–491, 8 1959.

[102] M. R. Zirnbauer, "Riemannian symmetric superspaces and their origin in random-matrix theory," *Journal of Mathematical Physics*, vol. 37, pp. 4986–5018, 10 1996.

[103] A. Altland and M. R. Zirnbauer, "Nonstandard symmetry classes in mesoscopic normal-superconducting hybrid structures," *Physical Review B*, vol. 55, pp. 1142–1161, 1 1997.

[104] P. W. Anderson, "Absence of Diffusion in Certain Random Lattices," *Physical Review*, vol. 109, pp. 1492–1505, 3 1958.

[105] A. Kitaev, "Periodic table for topological insulators and superconductors," *AIP Conference Proceedings*, vol. 1134, no. 1, pp. 22–30, 2009.

[106] X.-L. Qi, T. L. Hughes, and S.-C. Zhang, "Topological field theory of time-reversal invariant insulators," *Physical Review B*, vol. 78, p. 195424, 11 2008.

[107] H.-P. Breuer and F. Petruccione, *The Theory of Open Quantum Systems*. Oxford University Press, 1 2007.

[108] J. v. Neumann and N. A. Wheeler, *Mathematical Foundations of Quantum Mechanics*. Princeton University Press, 2 2018.

[109] D. Manzano, "A short introduction to the Lindblad master equation," *AIP Advances*, vol. 10, p. 025106, 2 2020.

[110] M. O. Scully and M. S. Zubairy, *Quantum Optics*. Cambridge University Press, 9 1997.

[111] R. Loudon, *The quantum theory of light*. Oxford University Press, 2000.

[112] K. Okamoto, "Chapter 3 - Optical fibers," in *Fundamentals of Optical Waveguides (Second Edition)* (K. Okamoto, ed.), pp. 57–158, Burlington: Academic Press, 2006.

[113] F. Bowman, *Introduction to Bessel functions*. New York: Dover Publications Inc., 1958.

[114] T. Søndergaard and B. Tromborg, "General theory for spontaneous emission in active dielectric microstructures: Example of a fiber amplifier," *Physical Review A*, vol. 64, p. 033812, 8 2001.

[115] F. Le Kien and A. Rauschenbeutel, "Nanofiber-mediated chiral radiative coupling between two atoms," *Physical Review A*, vol. 95, p. 023838, 2 2017.

[116] J. R. Ackerhalt, P. L. Knight, and J. H. Eberly, "Radiation Reaction and Radiative Frequency Shifts," *Physical Review Letters*, vol. 30, pp. 456–460, 3 1973.

[117] M. B. M. Svendsen and B. Olmos, "Modified dipole-dipole interactions in the presence of a nanophotonic waveguide," *arXiv:2211.13595*, 11 2022.

[118] A. Asenjo-Garcia, M. Moreno-Cardoner, A. Albrecht, H. Kimble, and D. Chang, "Exponential Improvement in Photon Storage Fidelities Using Subradiance and "Selective Radiance" in Atomic Arrays," *Physical Review X*, vol. 7, p. 031024, 8 2017.

[119] M.-D. Choi, "Completely positive linear maps on complex matrices," *Linear Algebra and its Applications*, vol. 10, no. 3, pp. 285–290, 1975.

[120] A. Jamiołkowski, "Linear transformations which preserve trace and positive semidefiniteness of operators," *Reports on Mathematical Physics*, vol. 3, no. 4, pp. 275–278, 1972.

[121] J. A. Needham, I. Lesanovsky, and B. Olmos, "Subradiance-protected excitation transport," *New Journal of Physics*, vol. 21, p. 073061, 7 2019.

[122] R. Jones, G. Buonaiuto, B. Lang, I. Lesanovsky, and B. Olmos, "Collectively Enhanced Chiral Photon Emission from an Atomic Array near a Nanofiber," *Physical Review Letters*, vol. 124, p. 093601, 3 2020.

[123] P. Jordan and E. Wigner, "Über das Paulische Äquivalenzverbot," *Zeitschrift für Physik*, vol. 47, no. 9, pp. 631–651, 1928.

[124] N. Batra and G. Sheet, "Physics with Coffee and Doughnuts," *Resonance*, vol. 25, no. 6, pp. 765–786, 2020.

[125] P. Fendley, "Strong zero modes and eigenstate phase transitions in the XYZ/interacting Majorana chain," *Journal of Physics A: Mathematical and Theoretical*, vol. 49, p. 30LT01, 7 2016.

[126] D. V. Else, P. Fendley, J. Kemp, and C. Nayak, "Prethermal Strong Zero Modes and Topological Qubits," *Physical Review X*, vol. 7, p. 041062, 12 2017.

[127] J. Kemp, N. Y. Yao, C. R. Laumann, and P. Fendley, "Long coherence times for edge spins," *Journal of Statistical Mechanics: Theory and Experiment*, vol. 2017, p. 063105, 6 2017.

[128] L. M. Vasiloiu, F. Carollo, and J. P. Garrahan, "Enhancing correlation times for edge spins through dissipation," *Physical Review B*, vol. 98, p. 094308, 9 2018.

[129] L. M. Vasiloiu, F. Carollo, M. Marcuzzi, and J. P. Garrahan, "Strong zero modes in a class of generalized Ising spin ladders with plaquette interactions," *Physical Review B*, vol. 100, p. 024309, 7 2019.

[130] L. M. Vasiloiu, A. Tiwari, and J. H. Bardarson, "Dephasing-enhanced Majorana zero modes in two-dimensional and three-dimensional higher-order topological superconductors," *Physical Review B*, vol. 106, p. L060307, 8 2022.

[131] K. Klobas, P. Fendley, and J. P. Garrahan, "Stochastic strong zero modes and their dynamical manifestations," *arXiv:2205.09110*, 5 2022.

[132] C. McDonnell and B. Olmos, "Subradiant edge states in an atom chain with waveguide-mediated hopping," *Quantum*, vol. 6, p. 805, 9 2022.